SAPIENZA
UNIVERSITÀ DI ROMA

Search for axion dark matter with the QUAX–LNF tunable haloscope

Facoltà di Scienze Matematiche Fisiche e Naturali

Corso di Laurea Magistrale in Physics

Candidate

Gianluca Vidali

ID number 1872665

Thesis Advisor

Prof. Cesare Bini

Co-Advisor

Dr. Claudio Gatti

Academic Year 2024/2025

Thesis not yet defended

Search for axion dark matter with the QUAX–LNF tunable haloscope
Master's thesis. Sapienza – University of Rome

This thesis has been typeset by LaTeX and the Sapthesis class.

Author's email: gianluca.vidali1@gmail.com

Abstract

The nature of dark matter remains one of the most compelling open questions in modern physics. Among the theoretically motivated candidates, the axion stands out not only as a solution to the strong CP problem via the Peccei Quinn mechanism, but also as a viable cold dark matter component. This thesis explores the axion both from a theoretical and an experimental perspective, focusing on the development and operation of the QUAX–LNF tunable haloscope, designed to search for galactic axions through their coupling to photons in a resonant microwave cavity.
The first part of the thesis reviews the theoretical background, from the emergence of the θ term in the QCD Lagrangian and the strong CP problem, to the introduction of axions and their parameter space as constrained by cosmology and astrophysics. Particular attention is given to the electromagnetic interaction, which enables the experimental detection via the Primakoff effect.
The second part of the thesis is dedicated to the description of the QUAX–LNF apparatus, covering the RF design, cavity characterization, and cryogenic setup. My contribution to the experiment includes calibration of the RF lines inside the cryostat, the implementation of a fitting procedure for the scattering parameters, and participation in the first data acquisition campaign.
No axion signal was observed in the explored mass range, but an exclusion limit was established, contributing to the broader effort of mapping the viable axion parameter space.

Contents

Chapter 1

Introduction

The 20th century witnessed a revolution in our understanding of the universe in both the smallest and largest scales, the former culminated with the establishment of the **Standard Model (SM)** of particle physics while the latter with **ΛCDM** model in cosmology.
With the 2012 discovery of the Higgs boson, every particle predicted by the SM has been observed. There are however many reasons to believe the SM is not an ultimate theory of nature and the most pressing comes from cosmology. The main problem with the ΛCDM model is that we understand neither Λ, that stands for Dark Energy, nor CDM that stands for **Cold Dark Matter**.
From cosmological observations there is now evidence that only 5% of the Universe constituents is explained by ordinary matter. The rest is supposed to be composed by Dark Matter (DM) for 25% and Dark Energy (DE). Our discussion follows DM models.
The existence of dark matter, a non baryonic form of matter, is inferred from its gravitational effects on ordinary matter. Observations indicate that our solar system orbits the center of the galaxy at about 200 km/s and we are immersed into a DM halo. Nevertheless it doesn't seem to do very much on smaller scales, DM has not been detected so far with particle physics experiment.
There are two Dark Matter models, Hot DM and Cold DM, meaning that particles are relativistic or not, the latter is favoured because of Large scale structure observations. The evidence for Cold DM is the most precious for particle physics as it is directly attributable to the existence of new species of particles.
In the context of theories of new physics beyond the Standard Model many new particles emerge, one of the first suitable model arised from Supersymmetry that predicts particles that can be included in the category of **WIMPs (Weakly Interacting Massive Particles)** and had great interest thanks to the WIMP miracle[1]. No detection has been claimed in this high energy landscape so increasingly resources are being invested in other models like **WISPs, Weakly Interacting Subelectronvolt Particles**, that arise when global symmetries in SM are spontaneously broken. Among these there are **axions and Axion-Like Particles (ALPs)**.
In this framework the QCD axion, a hypothetical spin 0 particle predicted by the Peccei-Quinn mechanism [2,3] to solve dynamically the so-called strong CP problem, is the best motivated candidate of DM. As we shall see in Chapter 2, the QCD lagrangian admits an additional term that violates the CP symmetry, but this violation is not seen in strong interactions. The violation of CP symmetry is a subject of great theoretical interest because there is substantially more matter than antimatter in the observable universe today, yet the known laws of physics are mostly CP symmetric. Nonetheless in the theory of QCD we have precisely the opposite

problem.
The value of the parameter responsible for this violation, $\overline{\theta}$, is constrained to be $\leq 10^{-10}$ from experiments [4] while it is theoretically expected to be of order one on naturalness grounds. In fact, $\overline{\theta}$ arises as the sum of two independent parameters coming from two independent physics sectors: QCD and electroweak theory. it appears so that strong CP violation is "accidentally" suppressed because the additive contributions to $\overline{\theta}$ happen to be equal and opposite to better than one part in ten billion.
The axion was identified by Weinberg [5] and Wilczek [6] as the pseudo Goldstone boson of a new spontaneously broken global symmetry that Peccei and Quinn had postulated. Axions are strongly related to mesons and indeed would mix with them obtaining a mass and featuring couplings to hadrons and two photons, Both coupling constants and mass are inversely proportional to a free parameter of the theory, f_a, that represents the energy scale at which the Peccei-Quinn U(1) symmetry is broken, so neither the couplings nor the mass can be a priori specified.
Within a few years theorists realized that if m_a were much smaller than the initial formulation of the PQ mechanism assumed, axions would interact very weakly with SM particles, and moreover they would be produced copiously in the early universe. For this motivations light axions can constitute dark matter and this is the reason for their name: they are named after a laundry detergent, since axions have the capability to "clean up" both the strong CP and DM problems.
We have reason to believe that dark matter is all around us all the time so we shall detect it to constrain both mass and coupling. In 1983 Sikivie [7] proposed two detection techniques, both relying on axion-photons coupling through the Primakoff process[8]: the **axion helioscope** to detect the copious flux of axions emitted from the Sun and the **axion haloscope** to detect axions from the hypothetical DM galactic halo.
In Chapter 3 I will present the main physical principles on which haloscope experiments are based, such as radiofrequency and resonant microwave cavities, then the **QUAX** experiment is described, whose acronym stands for 'QUest for AXions'. The experiment is funded by **INFN**, is situated at **LNF (Laboratori Nazionali di Frascati)** and **LNL (Laboratori Nazionali di Legnaro)** and I had the opportunity to witness the real first run of the QUAX-LNF tunable haloscope [9].
During my thesis I contributed to the experimental setup, to the data acquisition and to part of the data analysis, joining the team working in the **COLD laboratory (CryOgenic Laboratory for Detectors)**. Chapter 4 is indeed dedicated mainly to my thesis work, on how the radiofrequency concepts are used to exploit the calibration of lines inside the cryostat. In conclusion I will present the search for signals and finally the exclusion plot for axion mass and coupling.

Chapter 2

The physics problem and Axions as solution

2.1 Hints from theory

The formulation of this new scalar field, the axion, starts from a problem in the low energy landscape of Standard Model. In the **chiral limit** the quarks present some approximate symmetries. Thanks to electroweak symmetry breaking (EWSB) fermions acquire mass and this lead to a problem if one consider an axial symmetry $U(1)_A$ for the system: This brings to predict a wrong mass for the η' meson in the 3 quarks model.
The $U(1)_A$ problem is automatically resolved if one looks at the **nontrivial QCD vacuum structure**, but the story didn't end here. A new term with a $\overline{\theta}$ parameter appears in the QCD lagrangian that violates CP symmetry in QCD interactions. This would induce an **Electric Dipole Moment (EDM)** for the neutron, which has not been observed experimentally. This experimental constraint imply a fine-tuning problem that in turn is resolved by Peccei and Quinn mechanisim introducing a new axial symmetry $U(1)_{PQ}$ which promotes the parameter $\overline{\theta}$ to a dynamical field. Two nice introduction to the axion formulation are given in [10,11]

2.1.1 Symmetries and chiral limit

Let's begin with the two quark model, in the chiral limit QCD acquires a global $SU(2)V \times SU(2)_A \times U(1)_V \times U(1)_A$ symmetry. A **global vector** $U(1)_V$ transformation is a phase transformation that rotates the left and right-handed fields in the same sense:

$$q_L \to e^{-i\alpha} q_L \qquad q_R \to e^{-i\alpha} q_R \tag{2.1}$$

while a **global axial** $U(1)_A$ transformation causes the fields to rotate in the opposite sense:

$$q_L \to e^{-i\alpha} q_L \qquad q_R \to e^{i\alpha} q_R \tag{2.2}$$

An $SU(2)$ transformation operates in an analogous way when distinguishing between vector and axial, although it is just a little more complicated and involves a doublet of fields, therefore considering as an example a doublet of u and d quarks [12]:

$$\begin{pmatrix} u \\ d \end{pmatrix} \to e^{-i\epsilon_k \sigma_k/2} \begin{pmatrix} u \\ d \end{pmatrix} \tag{2.3}$$

where $k = 1, 2, 3$, ϵ_k are parameters and σ_k the three generators of $SU(2)$ group transformations, note that this transformations mix the quark flavors.

To show why they are symmetries, let's look at the QCD gauge invariant Lagrangian density for only one quark flavor [13]:

$$\mathcal{L}_{QCD} = \overline{q}_L i\gamma^\mu D_\mu q_L + \overline{q}_R i\gamma^\mu D_\mu q_R - \overline{q}_L m q_R - \overline{q}_R m q_L - \frac{1}{4} G^a_{\mu\nu} G^{\mu\nu}_a \tag{2.4}$$

with D_μ the covariant derivative and $G_{\mu\nu}$ a the gluon field strength tensor:

$$G^{\mu\nu}_a = \partial^\mu A^\nu_a - \partial^\nu A^\mu_a + g_s f_{abc} A^\mu_b A^\nu_c \tag{2.5}$$

where A^μ_a is the gluon vector field, $a, b, c = 1, ..., 8$ are indexes for the gauge fields, f_{abc} the structure constants of $SU(3)_c$, and g_s the coupling constant of strong interactions.
It is then sufficient only to look at the mass term in the Lagrangian of Eq. (2.4):

$$- m(\overline{q}_L q_R + \overline{q}_R q_L) \tag{2.6}$$

- $U(1)_V$ is an **exact symmetry** in any case and implies baryon number conservation [14], this symmetry implies that we should observe anti-baryons with exactly the same mass as the corresponding baryons but opposite charge, and indeed we do.

- $SU(2)_V$ maintain mass terms invariant, but it is indeed necessary to keep the quark masses to zero to make it a symmetry, because u and d are part of a doublet and therefore they must have the same quantum numbers, including mass. This symmetry implies that we should observe doublets of hadrons with almost the same mass (experimental mass of u and d is not equal) whose strong force interactions are identical. This symmetry is known as the **nuclear isospin symmetry** and the most obvious such doublet comprises the proton ($m_p = 938.3$ MeV) and neutron ($m_n = 939.6$ MeV).

- $SU(2)_A$ is only a symmetry in the **massless limit** and implies the existence of another doublet of particles nearly degenerate in mass but with opposite parity, we do not observe such particles so it has to be somehow broken together with $U(1)_A$. Generally axial symmetries only exist in the massless limit, for this reason the massless limit is also called the chiral limit.

If the axial symmetries are spontaneously broken, we should expect three **Goldstone bosons** corresponding to the generators of $SU(2)_A$ along with a fourth Goldstone boson from $U(1)_A$ [12]. Because these symmetries are chiral, all four Goldstone bosons will be pseudoscalar fields which are odd with respect to parity.
In the hadron spectrum there exist a triplet of particles with odd parity: the **pion triplet**, π^0 and $\pi^\pm$ with $m_{\pi^0} = 135$ MeV, $m_{\pi^\pm} = 140$ MeV, they are not much smaller with respect to Λ_{QCD} but they are the lightest mesons and their masses go to zero as m_u, m_d going to zero, so they can be thought of as the pseudo Goldstone bosons of the group. In this 2-flavor model the pseudo-Goldstone boson associated with $U(1)_A$ would be instead the **pseudoscalar η meson**. If the s quark didn't exist, it would have a mass smaller than it actually is ($m_\eta \sim 548$ MeV). Besides if this model is incomplete because the absence of s quark, there is evidence that the approximate $SU(2)_A$ and $U(1)_A$ symmetries of the strong interactions of light quarks are spontaneously broken in the hadronic phase.
If we now extend our model to the 3-flavor case, QCD possesses a global $SU(3)_V \times$

$SU(3)_A \times U(1)_V \times U(1)_A$ symmetry, then by breaking the axial symmetries, eight pseudo Goldstone bosons from $SU(3)_A$ and one from $U(1)_A$ are expected. The **pseudoscalar singlet** $\eta^{'}$ **meson** and the **pseudoscalar octet** comprising the three pions, the four kaons and the η meson are the candidates we are looking for. All the mesons aside $\eta^{'}$ still have masses small enough to play the role of pseudo-Goldstone bosons, the problem here is that $m_{\eta'} \sim 958$ MeV is much higher compared to Λ_{QCD}. This is in contrast with the work of Steven Weinberg too [15], who pointed out that in this 3-flavor model the pseudo-Goldstone boson associated to the $U(1)_A$ broken symmetry should have a mass:

$$m_{\eta'} < \sqrt{3} m_\pi \sim 240\ MeV. \tag{2.7}$$

The essence of the $U(1)_A$ problem resides here, why is the observed $m_{\eta'}$ meson so much heavier?

2.1.2 Solution to the $U(1)_A$ problem

The solution at this problem can be summarized observing that the expected pseudo-Goldstone boson doesn't exist because there is **no** $U(1)_A$ **symmetry at all**, and this declaration is made possible if one exploit chiral anomalies, the nontrivial topology of the QCD vacuum and their relationship [16].
Even before the $U(1)_A$ problem it was already well established that global $U(1)_A$ symmetries were **anomalous**, anamalous in the sense that is a symmetry of the classical Lagrangian but is violated in the corresponding quantum theory. However the solution comes down to a distinction between the behavior of Abelian and non-Abelian gauge theories and this lead us toward the **strong CP problem**.
In classical field theories, **Noether's theorem** states that each symmetry of a Lagrangian has associated to it a conserved current J^μ in the sense that:

$$\partial_\mu J^\mu = 0 \tag{2.8}$$

is the continuity equation that implies a **conserved charge** defined as:

$$Q = \int d^{3x} J^0. \tag{2.9}$$

In most cases this procedure works for the quantum theory too in which the fields are promoted to operators. But if the classical theory includes at least one fermion which transforms under a global $U(1)_A$ symmetry and is coupled to gauge fields A^μ_a, Eq. (2.8) does not hold in the quantum theory, infact $U(1)_A$ current obeys:

$$\partial_\mu J^\mu_A = \frac{g^2}{32\pi^2} F^{\mu\nu}_a \tilde{F}_{\mu\nu a} \tag{2.10}$$

where g is the gauge coupling, $F^{\mu\nu}_a$ is the gauge field strength tensor that we wrote explicity for the gluon field in Eq. (2.5) and

$$\tilde{F}_{\mu\nu a} = \frac{1}{2} \epsilon_{\mu\nu\alpha\beta} F^{\alpha\beta}_a \tag{2.11}$$

is its dual, where $\epsilon_{\mu\nu\alpha\beta}$ is the Levi-Civita symbol, antisymmetric in all indices.
Eq. (2.10) is the formal statement of the **chiral anomaly** [13, 14]: If the fermion that transforms under $U(1)_A$ is coupled to more than one gauge group, there will be

one term of Eq. (2.10) for each gauge symmetry. Moreover if there are N fermions with $U(1)_A$ symmetries coupled to a particular gauge group, the corresponding term should be multiplied by N.
Since $\partial_\mu J^\mu_A \neq 0$, it is evident that the axial current is actually not conserved, because of the effect of the chiral anomaly. Therefore $U(1)_A$ symmetry is **automatically broken** (actually is not a simmetry at all): this implies that we don't need a pseudo-Goldstone boson in the hadron spectrum anymore and the arguments of Weinberg on the η' mass become irrelevant.
Furthermore Eq. (2.10) implies that a $U(1)_A$ transformation on a single fermion field with parameter α does not leave the Lagrangian invariant, but instead adds a term of the form:

$$\delta\mathcal{L} = \frac{g^2}{16\pi^2}\alpha F^{\mu\nu}_a \tilde{F}_{\mu\nu a}. \tag{2.12}$$

We did not include such terms in the original Lagrangian because they are a total derivative, thus they correspond to surface terms which can only contribute to the action at the boundaries of the spacetime volume, where any reasonable field ought to vanish, but chiral anomalies can cause them to appear anyway.
While everything may seem to follow a linear path, the full picture has yet to emerge: we need to talk about the nontrivial topology of the QCD vacuum and in doing so let's introduce the so called θ **terms** in SM that are formally equivalent to Eq. (2.12), with parameters θ_{EM}, θ_W , and θ_{QCD} in place of α for the corresponding gauge symmetry [17]. Let's anticipate here that the presence of the antisymmetric Levi-Civita symbol implies that θ terms violate P and T symmetries (thus they also violate CP by the **CPT theorem**). The reason we did not include θ terms in the Lagrangian is that each θ term is a **total derivative**.
It can been shown that for a $U(1)_A$ current which is not conserved due to an anomaly with QED, is still possible to construct a conserved charge Q in the sense that there are no observable effects due to surface terms [18]. However, it turns out that surface terms can have observable effects in **non Abelian gauge theories**.
In the general case of non Abelian gauge theories the surface terms from Eq. (2.12) become $\frac{1}{2}\epsilon_{\mu\nu\alpha\beta}F^{\mu\nu}_a F^{\alpha\beta}_a = \partial^\mu K_\mu$ where:

$$K_\mu = \epsilon_{\mu\nu\alpha\beta}\left(A^\nu_a F^{\alpha\beta}_a - \frac{g}{3}f_{abc}A^\nu_a A^\alpha_b A^\beta_c\right). \tag{2.13}$$

The main problem resides here, the gauge fields A^μ_a of QCD appearing in K^μ do not all tend to zero simultaneously at infinity, therefore the surface integral of K^μ does not cancel. Non Abelian gauge theory gets very complicated, here I will present only the key passages but more details can be found in Refs. [13, 14].
The discussion can be simplified by restricting our focus to **vacuum field configurations**: a trivial example of a vacuum field configuration is $A^\mu_a = 0$, but gauge invariance implies that there are infinitely many others related to the trivial case by gauge transformations. It turns out that it is not possible to smoothly transform each vacuum configuration into another, each vacuum is classified by an integer number n, called **winding number**, and all of them are separated by energy barriers. The vacua are then indicated by $|n\rangle$ and for each n a different expression of the fields exists. For instance, the solution with n = 1 is called instanton, while n = 0 corresponds to $A^\mu_a = 0$.
Belavin et al. [19] first noted that non-Abelian gauge theory permits vacuum field configurations for which the surface integral of Eq. (2.13) is nonvanishing, they

showed that there exist vacuum field configurations with:

$$\frac{g^2}{32\pi^2}\int d^{4x}\partial^\mu K_\mu = n. \tag{2.14}$$

't Hooft [20] was the first to point out that the integral of Eq. (2.14) is just the volume integral of Eq. (2.10), and a nonzero value implies that the charge corresponding to J^μ_A is not conserved, so it can be claimed that instantons and other field configurations with n $\neq$ 0 resolve the $U(1)_A$ problem.
It is though possible the **quantum tunnelling** between different vacua with different winding numbers: the transition amplitude from two vacua is not negligible, so it is preferable to define a true vacuum that possibly remains fixed. We want the true vacuum to be invariant under the "tunnelling" operator that acts as:

$$\mathcal{U}_k \left|n\right\rangle = \left|n+k\right\rangle \tag{2.15}$$

this request is satisfied if we define a superposition of all the vacua, called θ **vacuum**, such as:

$$\left|\theta\right\rangle = \sum_n e^{-in\theta}\left|n\right\rangle . \tag{2.16}$$

If now one evaluate the transistion probability from one θ vacuum to another $\theta^{'}$ it is possible to find [14]:

$$\mathcal{M}_{\theta\to\theta'} \sim \delta(\theta^{'}-\theta)e^{-(S-in\theta)} \tag{2.17}$$

where S is the action. The Dirac delta function enforces the absence of tunneling between distinct θ vacua, consistently with the physical expectation.
The interesting part is the factor containing the winding number: it can be see that from Eq. (2.14), using the definition of $\partial^\mu K_\mu$ from Eq. (2.13), in a theory in which the true QCD vacuum state is $\left|\theta_{QCD}\right\rangle$ there is a contribution to the Lagrangian of the form we have predicted in Eq. (2.12):

$$\mathcal{L}_\theta = \frac{g_s^2}{32\pi^2}\theta_{QCD}G_a^{\mu\nu}\tilde{G}_{\mu\nu a} \tag{2.18}$$

where now I explicited the fact that we are talking about quark and gluons: $G_{\mu\nu}$ is the gluon field strength tensor and g_s^2 is the coupling of the strong interaction. Thus we see that the solution to the $U(1)_A$ problem implies the existence of a QCD θ term and as we anticipated this kind of terms violate CP simmetry: we have now the **strong CP problem** to deal with.

2.1.3 Strong CP problem

In the previous subsection we showed that non-Abelian gauge theories permit field configurations with nonvanishing surface terms, and then went on to show that in such theories the θ parameter from the θ term in SM has a physical interpretation as the parameter describing the true gauge vacuum state. The resolution of the $U(1)_A$ problem therefore, required us to recognize the existence of non-Abelian gauge vacua other than $\left|n=0\right\rangle$, but does not give us any hint to the value of θ_{QCD}. Nevertheless what is important is that any nonzero θ_{QCD} produces an electric dipole moment (EDM) for the neutron, and the non observation of the neutron EDM implies that θ_{QCD} must be extremely small. This is the essence of the strong CP problem, but there is also more to deal with.
It turns out that in the SM the strong CP problem actually cannot be resolved

by QCD alone: quarks are charged under both QCD and the electroweak gauge group. It is instructive to point out what is the variation of θ_{QCD} under an axial transformation: for N_f flavors of massless quarks the $U(1)_A$ is anomalous and we have new contribution to the lagrangian as in Eq. (2.12); this term adds to the θ_{QCD} one, causing him to shift:

$$\theta_{QCD} \to \theta_{QCD} - 2N_f\alpha. \tag{2.19}$$

This means that if only θ_{QCD} contributed to CP violation, by an appropriate choice of the parameter α, we could make $\theta_{QCD} = 0$, however the **electroweak sector** contribute too and as we know fermions acquire mass thanks to the electroweak symmetry breaking via Higgs mechanism.
In order to see where a contribution from Electroweak can rise, we can look at **Yukawa type interactions** between Higgs fields and quarks which are renormalizable and invariant under the full SM gauge group, they have this form [14]:

$$\mathcal{L}_{Yukawa} = -y_d(\overline{Q}_L \cdot \phi)d_R - iy_u(\overline{Q}_L \cdot \sigma_2\phi^*)u_R + h.c. \tag{2.20}$$

where ϕ is the Higgs doublet, $Q_L = (u_L, d_L)^T$ is the left-handed quark doublet, u_R and d_R are right-handed up and down quarks, y_u and y_d are Yukawa coupling constants, and σ_2 is the second Pauli matrix. After EWSB, we can replace the Higgs doublet with its vacuum expectation value $< \phi >= \frac{1}{\sqrt{2}}(0, v)^T$:

$$\mathcal{L}_{Yukawa} = -\frac{1}{\sqrt{2}}y_d v\bar{d}_L d_R - \frac{1}{\sqrt{2}}y_u v\bar{u}_L u_R + h.c. \tag{2.21}$$

Thus below the electroweak scale the previously independent left and right chiral down quark fields are mixed together and down quark acquire mass $m_d = y_d v/\sqrt{2}$ while for up quark $m_u = y_u v/\sqrt{2}$.
For our purposes we have to generalize Eq. (2.21), the other two generations of fermions are essentially copies of the first as they have all the same quantum numbers under the SM gauge groups. Consequently y_u and y_d should actually be replaced with 3×3 matrices Y_u and Y_d that sit between the 3 quark generations. This matricies are not diagonal or hermitian, but can be diagonalized through unitary matrices $\mathcal{U}$ and $\mathcal{W}$, which can be in turn absorbed into the definition of the left- and right-handed quark fields respectively: this is the mass basis in which Eq. (2.21) looks like a proper mass term. The transformations we used are a combination of vector $U(1)_V$ and axial $U(1)_A$ rotations, but these axial phase rotations as we know are anomalous so it will generate an additive contribution to θ_{QCD} of the form [21]:

$$\theta_{EW} = arg\Big[det\Big(Y_d Y_u\Big)\Big]. \tag{2.22}$$

Consequently the Lagrangian that has physical observable effects is of the form:

$$\mathcal{L}_{CP} = \frac{g_s^2}{32\pi^2}\,\overline{\theta}\,G_a^{\mu\nu}\tilde{G}_{\mu\nu a} \tag{2.23}$$

where $\overline{\theta}$ has contributions from both QCD and EW:

$$\overline{\theta} \equiv \theta_{QCD} - \theta_{EW}. \tag{2.24}$$

It's important to underline that this is an **additional contribution** to the CP violation in the SM, alongside to the phase δ_{CKM} of the CKM matrix, responsible

for the kaon and B oscillations. Therefore in the absence of massless quarks, the strong CP problem is real, and it has turned out to be a problem of the full SM rather than just the strong force.
As said in the beginning, an additional lagrangian term like Eq. (2.23) produces an electric dipole moment for the neutron that has been calculated in Ref. [22]. Is proportional to $\overline{\theta}$ and it is estimated to be:

$$d_n \sim 2.4 \times 10^{-16}\,\overline{\theta}\,e\,cm \tag{2.25}$$

where e is the fundamental electric charge. In the article, with the experimental bound of those times, it was estimated an upper limit on the theta parameter of $|\overline{\theta}| < 3 \times 10^{-10}$. From the most recent experiment on neutron EDM instead, it was set a most stringent upper limit of about [4]:

$$|\overline{\theta}| < 0.67 \times 10^{-10}. \tag{2.26}$$

This is an extrimely small value considering that we have two contributions from **two independent sectors**: there are no reasons for θ_{QCD} and θ_{EW} to tune exactly to zero when they are summed. There is no way for the two parameters to "know" about each other, we need therefore to look beyond the SM for a solution to the strong CP problem.

2.2 Axions

Theorists came out mostly with 3 solutions to the strong CP problem [17]:

- The presence of a **massless quark**, for example the u quark, that will allow us to do the procedure described by Eq. (2.19) and gauge away by a phase rotation θ_{QCD}, because θ_{EW} term wouldn't be present. But as exposed in the previuous section, this hypotesis is ruled out by experiment, since there is no evidence of massless quarks.
- A **spontaneous CP violation**, in the sense that it exists in the Standard Model a more general CP symmetry that would be in turn spontaneously broken, allowing for CP violation. This is ruled out by experiment too, since experimental data is in excellent agreement with a CP violation due to the CKM matrix.
- The **Peccei Quinn mechanism**, discussed in this thesis, in which an additional $U(1)_A$ symmetry is assumed in the theory. The axion emerge here, it would be an additional pseudo-Goldstone boson from the simmetry breaking.

As said so, the PQ mechanism will be presented and this lead us to 3 theoretical models: **PQWW, KSVZ, DFSZ**. The meaning of this 3 acronyms will be presented further in the reading along with Axion main parameters such as his mass and his coupling with different fields. The value of this two parameters doesn't have hints from theory, then it will be presented the axion parameter space with all the experiments and bounds imposed by Astrophysics and Cosmology.

2.2.1 Peccei-Quinn mechanism

This solution was proposed by R. Peccei and H. Quinn in two papers in 1977 [2,3]. The idea in the end is that of gauge away θ_{QCD} more or less as we suggested

in Eq. (2.19). In doing so, they suggested to introduce a **further exact axial global** $U(1)$ **symmetry**, now called $U(1)_{PQ}$ symmetry, by adding a **scalar field**. Therefore if this is spontaneously broken and has a chiral anomaly, we will have an additional term in the lagrangian as Eq. (2.12) that can absorb the $\overline{\theta}$ term. In 1978, Weinberg [5] and Wilczek [6], pointed out that adding this scalar field which couses the simmetry breaking, would generate a new Goldstone boson: **the axion**.
In exploiting the mechanism, it's enough to consider only **one quark flavor** and a **new scalar complex field** σ. As said in subsection 2.1.1, a mass term for the quark is not invariant under $U(1)_A$ rotations, so we start again with yukawa coupling like Eq. (2.20). However let's consider now only one quark flavor and the σ field despite of the Higgs doublet:

$$\mathcal{L}_{Yukawa} = -y(\overline{q}_L \sigma q_R + \overline{q}_R \sigma^* q_L) \tag{2.27}$$

where the σ field has a lagrangian:

$$\mathcal{L}_\sigma = \frac{1}{2}\partial_\mu \sigma \partial^\mu \sigma^* - \mu^2 |\sigma|^2 - \frac{\lambda}{4}|\sigma|^4 \tag{2.28}$$

supponing that the potential has a minimum at $|\sigma| = f_a$. If we apply an axial $U(1)$ transformation to the quarks they rotate like Eq. (2.2), then we need that σ changes as $\sigma \to e^{-2i\alpha}\sigma$ if we want the lagrangian to be invariant.
If the scalar field satisfies this additional condition, $U(1)_{PQ}$ is though an exact global symmetry that has in turn to be broken to generate the quark mass. In the spirit of SSB we expand σ around its minimum:

$$\sigma(x) = (\rho(x) + f_a)e^{ia(x)/f_a} \tag{2.29}$$

where $\rho(x)$ and $a(x)$ are two real fields: thanks to it the lagrangian acquire the quark mass term along with kinetic and potential terms for the two real field. The ρ field plays the role of the Higgs boson in the EWSSB, while the axion a is supposed to be the **massless Goldstone boson**.
The key point here is that $U(1)_{PQ}$ present a chiral anomaly and as we know this causes the lagrangian to acquire anothere CP violating term like Eq. (2.12). We can substitute the α parameter with a/f_a by noticing that if we apply a $U(1)$ rotation to the σ field, the axion field undergoes this transformation:

$$a \to a + \alpha f_a. \tag{2.30}$$

If we underline only the terms of our interest, the final lagrangian takes the following final form [16]:

$$\mathcal{L} = \mathcal{L}_q + \mathcal{L}_\sigma + \frac{1}{2}\partial_\mu a \partial^\mu a + \mathcal{L}_{int}[\partial^\mu (a/f_a); q] + \frac{\alpha_s}{8\pi}\overline{\theta} G_a^{\mu\nu}\tilde{G}_{\mu\nu a} + \frac{\alpha_s}{8\pi}\frac{a}{f_a} G_a^{\mu\nu}\tilde{G}_{\mu\nu a} \tag{2.31}$$

where $\mathcal{L}_{int}$ contains interactions between quark and axion, and is used $\alpha_s = \frac{g_s^2}{4\pi}$. The last term it's the one we are interested in, it can be seen as a potential V_{eff} and has two conseguences: can solve the strong CP problem and give rise to an **axion mass**. As we anticipated, in solving the CP problem, $\overline{\theta}$ can be absorbed and we fullfill this task by redifining the potential term, or equivalently, the axion field. Since $\overline{\theta}$ term has the same structure as the potential, we can consider them as one single term, later on we can impose that this potential has a minimum when calculated in the vacuum, explicitly $\langle \frac{\partial V_{eff}}{\partial a} \rangle = 0$, so in the end it can be found [3]:

$$\langle a \rangle = -\overline{\theta} f_a \tag{2.32}$$

and in this sense the axion field a is the **dynamical version** of $\overline{\theta}$. We can also define a physical axion field with null vacuum expectation value, given as $a_{phys} = a - \langle a \rangle$. As said so, an axion mass can rise from V_{eff}: this term infact explicity breaks $U(1)_{PQ}$, it can be interpreted as a tilt of the wine-bottle-shaped potential, typical of a toy model of SSB for one complex scalar field [10], along a certain direction. The axion therefore rolls towards the new tilted minimum and oscillates around that, acquiring a mass that can be calculated from V_{eff}:

$$m_a^2 = \left\langle \frac{\partial^2 V_{eff}}{\partial a^2} \right\rangle_{\langle a \rangle = -\overline{\theta} f_a} . \tag{2.33}$$

We can now rewrite the lagrangian considering a_{phys} consideration and adding the mass term we have discussed:

$$\mathcal{L} = \frac{1}{2}\partial_\mu a_{phys} \partial^\mu a_{phys} - \frac{1}{2} m_a^2 a_{phys}^2 + \frac{\alpha_s}{8\pi} \frac{a_{phys}}{f_a} G_a^{\mu\nu} \tilde{G}_{\mu\nu a} \tag{2.34}$$

where i omitted $\mathcal{L}_q$, $\mathcal{L}_\sigma$, $\mathcal{L}_{int}$ and where now we have the usual mass term beside an interaction between the axion and the gluons. The strong CP problem is therefore solved: when axion excitations are not present a_{phys} is zero and the classical potential is minimized at zero, while when a_{phys} is present, a CP violation term follows. The key interpretation here is that when we consider for a long time interval observable quantities depending on a_{phys}, like neutron EDM, they are averaged to zero and the **CP violation is not seen**.
Now is important to extend this mechanism to the whole standard model, the more immediate extention is the **PQWW** one that follows from Peccei, Quinn, Weinberg and Wilczek. We will later on refer to a_{phys} simply by writing a.
PQ mechanism requires at least one quark q and one complex scalar field σ, on the contrary SM ontains many quarks and we saw how they acquire mass via EWSSB: identifying σ with the **Higgs doublet** ϕ would be the most immediate extension of our model. Nonetheless we have an impediment, our lagrangian have to be invariant under all SM gauge groups: this is fullfilled only if ϕ appears in the term that gives mass to down-type quarks and ϕ^* for the up-type, as we wrote in Eq. (2.20). However ϕ and ϕ^* transform differently under $U(1)_{PQ}$ and the necessary condition to make the lagrangian invariant falls. Peccei and Quinn thus extended the Higgs sector of the SM to include **two Higgs doublets**, ϕ_1 that couples to up-type quarks and ϕ_2 to down-type, having transformations that preserve $U(1)_{PQ}$ invariance.
The two Higgs doublets in the PQWW model have two different vacuum expectation values v_1 and v_2, $f_a = \sqrt{v_1^2 + v_2^2}$ is a free parameter of the theory and in this model is identified with the electroweak scale $v = 246$ GeV.
The axion mass has been calculated with effective Lagrangian techniques, what is important here is that in this calculations **mixing terms** with neutral pions and η mesons arise. These are responsible for generating the axion mass term but also allow the axion to have **interactions with two photons**: a very useful property that will be exploited to design an experimental approach to the axion detection. Its mass is given by [13, 14]:

$$m_a^{PQWW} = N_g \left(x + \frac{1}{x} \right) \frac{m_\pi f_\pi}{v} \frac{\sqrt{m_u m_d}}{m_u + m_d} \tag{2.35}$$

where $N_g = 3$ is the number of fermion generations and x $= v_2/v_1$ is the only free parameter of the PQWW model: if we plug in number we obtein approximatly

$m_a^{PQWW} > 150$ keV with a minimum value of $m_a^{PQWW} \sim 25$ keV for $x = 1$.
As stated before, this model lead to a coupling with 2 photons too:

$$\mathcal{L}_{a\gamma\gamma} = \mathcal{K}_{a\gamma\gamma} \frac{\alpha_{em}}{4\pi} \frac{a}{f_a} F_{\mu\nu} \tilde{F}^{\mu\nu} \; ; \qquad \mathcal{K}_{a\gamma\gamma} = N_g \left(x + \frac{1}{x} \right) \frac{m_u}{m_u + m_d} \tag{2.36}$$

with $\alpha_{em} = e^2/4\pi$ the fine structure constant of QED in natural units and $F_{\mu\nu}$ the electromagnetic field strength tensor.
This model of high energy mass axion has however been ruled out by **Kaons decay experiment** [23]. Experimental evidences of this type recall that perhaps theories in which $f_a \gg v$ are more reliable, and since axion mass and coupling are inversely proportional to f_A we are conducted towards light axions very weakly coupled to SM particles. These are called **invisible axion models**, we will briefly discuss only two of them:

- From Kim [24] and Shifman, Vainshtein, Zakharov [25] the **KSVZ** model in which only a complex scalar field σ and a single heavy quark ($m_q \propto f_a$) are added to the SM, with the energy breaking scale $f_a \gg v$. The mass term has the same form as in the PQWW model, but is rescaled with the new f_a value:

$$m_a = \left(\frac{v}{f_a} \right) m_a^{PQWW}. \tag{2.37}$$

  The peculiarity of this model is that the axion doesn't interact with leptons.

- From Zhitnitsky [26] and Dine, Fischler, Srednicki [27] the **DFSZ** model that is an exstention of the PQWW one: beside the Higgs doublets, a complex scalar field σ is added too. Here all the interaction exploited in the PQWW model are manteined but the mass has the same expression as in Eq. (2.37), where now instead $f_a = \langle \sigma \rangle$.

This was just an overview to the theoretical problem and to the axion formulation, to give an idea about the motivation that push this experimental field of Physics and to introduce some useful concepts that we will need when we are going to talk about experimental approaches. There is a lot more to talk about this models we introduced and there are many other models that predict axions with different masses and couplings[1].

2.2.2 Parameter space

If axions constitute **Dark Matter**, their electromagnetic interactions may be observable in a sufficiently sensitive laboratory-scale detector. As said the most important fundamental parameter in any invisible axion model is the **PQ symmetry breaking scale** f_a: we discussed how mass (2.37) and coupling constant with photons (2.36) depend on it. We didn't mention it but also interactions with fermions arise in the DFSZ model, this will be usefull in discussing astrophysical constraints.
In the axion coupling with two photons lagrangian is present $\mathcal{K}_{a\gamma\gamma}$ that is a dimensionless model-dependent parameter, we can write it in a more compact way by defining a new coupling constant $g_{a\gamma\gamma}$ that has now dimensions GeV^{-1} and is still model-dependent:

$$\mathcal{L}_{a\gamma\gamma} = \frac{1}{4} g_{a\gamma\gamma} a F_{\mu\nu} \tilde{F}^{\mu\nu} \; ; \qquad g_{a\gamma\gamma} = \frac{\alpha_{em}}{\pi} \frac{\mathcal{K}_{a\gamma\gamma}}{f_a} \tag{2.38}$$

note that as the mass, also $g_{a\gamma\gamma}$ is inversely proportional with respect to f_a; in this sense axions are "invisible", their couplings with SM particles are extreamly weak.
It's very usefull to write the electromagnetic interaction in terms of the **electric and magnetic fields**, this is explicitly derived in appendix A of Ref. [10]:

$$\mathcal{L}_{a\gamma\gamma} = \frac{1}{4} g_{a\gamma\gamma} a F_{\mu\nu} \tilde{F}^{\mu\nu} = -g_{a\gamma\gamma} a \vec{E} \cdot \vec{B} \tag{2.39}$$

This expression will be exploited in dealing with haloscope detectors, this will help us in identifying the right mode inside a microwave cavity dealing with axion conversion into photons.
It's also worth noticing that Eq. (2.39) has exactly the same form as the **Primakoff process** [8] that originally was introduced to explain π^0 production through a two-photon interaction, the decay of π^0 into two photons is on the contrary called inverse Primakoff process. This two processes can happen through a triangle diagram with a virtual fermion in the loop and the axion therefore goes through the same as it has the same interaction lagrangian, because it inherits the electromagnetic interactions from **mixing** with the pion and η meson. The diagram representing the inverse Primakoff process of the axion is shown in Fig. 2.1 (a), together with the axion production via Primakoff effect diagram Fig. 2.1 (b).

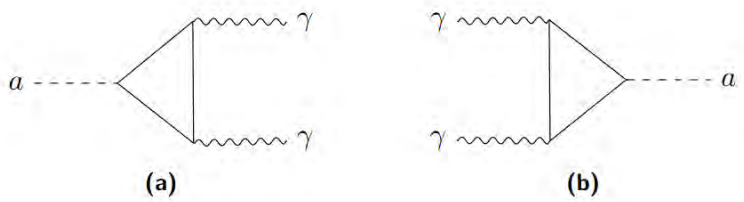

Figure 2.1. [11] (a) Axion decay into two photons via inverse Primakoff effect. (b) Axion production via Primakoff effect in vacuum.

This two diagrams provide both a **detection technique** and a **production mechanism**: Primakoff effect could be responsible for an axion flux from stars while inverse Primakoff is the paradigm of axion detection.
In practice, axion detection, can be exploited substituting a real outgoing photon with an **external static magnetic field**, that provides virtual photons but is treated as a classical electromagnetic field. In this sense, in Haloscopes, a microwave resonant cavity is immersed within external magnetic field lines: this conversion is schematized in Fig. 2.2. In this case too, if one exchange axion and photon lines, this could account for a production mechanism in some regions of the universe where high magnetic fields are achieved.

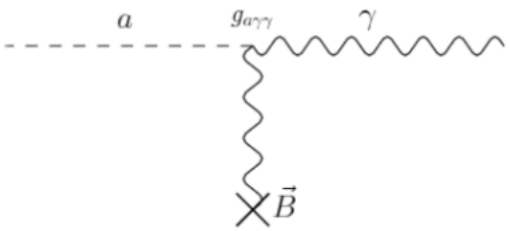

Figure 2.2. [10] Axion conversion into a photon stimulated by an external static magnetic field.

This digression aside, we noticed before that both coupling constant and mass are inversely proportional to f_a: this obviously imply that $g_{a\gamma\gamma} \propto m_a$. In this sense, **the parameter space** for the electromagnetic interaction is the $g_{a\gamma\gamma}$ vs. m_a plane, this is shown in Fig. 2.3.

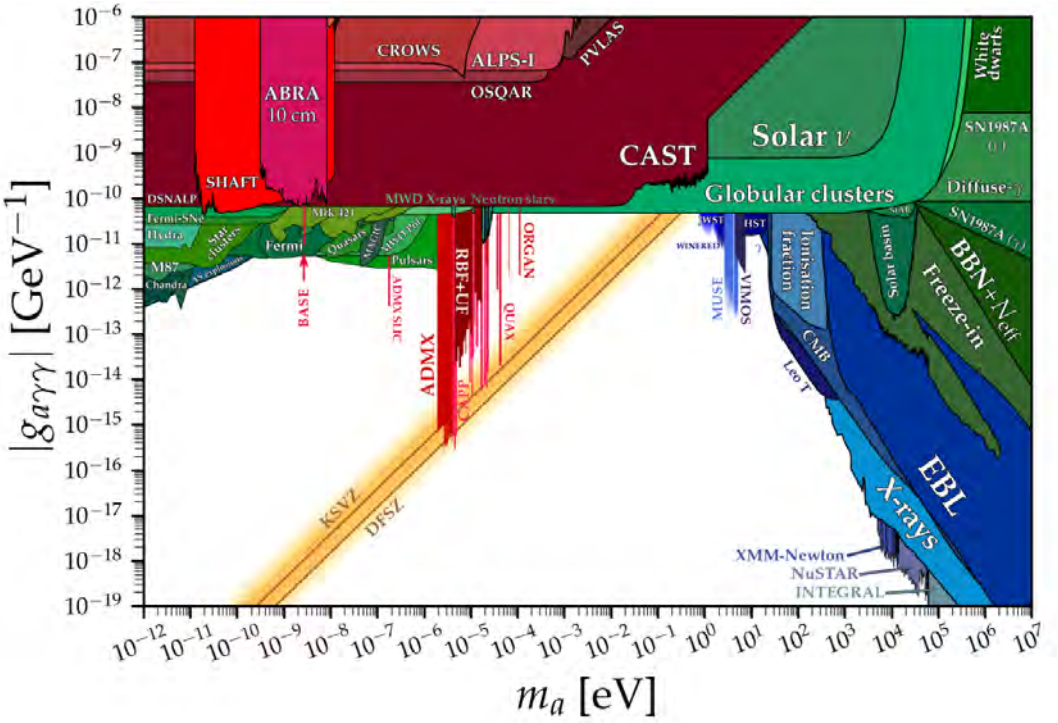

Figure 2.3. [28] Axion parameter space in terms of mass m_a and coupling to photons $g_{a\gamma\gamma}$. The figure can be reproduced by using the Python notebook available in the Ref, where it can be found also all the references to the data. In yellow the model band is shown, with KSVZ and DFSZ models marked. Red regions mark exclusions by direct detection experiments (helioscopes, haloscopes, LSW). Green regions represent exclusions from astrophysical searches in which is not considered the fraction of DM that axions make up. Blue regions represent exclusions from astrophysical searches which rely on DM axions.

This is an exclusion plot in the sense that the coloured regions, except yellow one, represent the limits put on axion parameters by various experiments. Light shining through walls, helioscopes and haloscopes will be described in Section 2.3 while bounds from astrophysical observations like sun or Supernovae in Section 2.2.3. The yellow band instead is called **model band** and it accounts for QCD axion models, such as KSVZ and DFSZ models. But why it is a band? Let's consider $z = m_u/m_d$ as the light quark mass ratio, based on this the mass can be written as:

$$m_a = \frac{m_\pi f_\pi}{f_a} \frac{\sqrt{z}}{1+z}; \tag{2.40}$$

taken from Eq. (2.35) with $x = 1$. From values of masses in [29], z can vary in the interval $0.4 < z < 0.55$, that results in a range for possible axion masses.
Moreover $g_{a\gamma\gamma}$ depends on this ratio too, but it also depends on the possible values that $\mathcal{K}_{a\gamma\gamma}$ can take. We expressed this latter quantity in the PQWW model but

more generally for invisible axion models it can be written in the form [30]:

$$\mathcal{K}_{a\gamma\gamma} = \frac{1}{2}\left(\frac{E}{N} - \frac{2}{3}\frac{4+z}{1+z}\right) \tag{2.41}$$

where E and N are the **electromagnetic and color anomalies** of the axial current associated with the axion. For a fixed value of z, there will be different straight lines in the plot, corresponding to different models that have distinct values of the ratio E/N. Usually are reported two lines: the one for DFSZ with E/N = 8/3 and the one for KSVZ with E/N = 0, if in this case the electric charge of the new heavy quark is taken to vanish. However the ratio E/N is not exactly known, and this allows to define a band of values for the coupling as funcion of the mass, the yellow region in the plot.
This is the ultimate task of axion searching experiments, to reach the model bands to cover all the expected possible values of coupling and mass. In this sense there must be seen the red vertical lines, they are all haloscope experiments, among which also figures QUAX, covering a different possible value of the mass. However, this band still does not exhaust all the possibilities. In fact, there exist classes of QCD axion models whose photon couplings populate the entire still-allowed region outside the yellow band, we will not deal with this models in this work tho.

2.2.3 Astrophysical and Cosmological constraints

The **green regions** in Fig. 2.3 accounts for Astrophysical bounds on mass and coupling. In fact, if axion exists, it can affect various astrophysical objects evolution. As said abundantly, axions are produced mainly by Primakoff effect. Considering a star for example, axions can be generated in their core if a photon interacts with the Coulomb field of the plasma. Then since axions are thought to interact very weakly with SM particles, they can escape the core providing a non-standard energy loss mechanism for stars. A stringent bound on the axion coupling can be extracted if one compare data from measurements on stellar evolution with the predicted rate of standard energy loss.
For completeness let's talk for a moment about axion interaction with **fermions**: we have already said that this type of interactions arise only in the DFSZ model. The interaction term in the lagrangian can be written as an effective, CP-conserving, Lagrangian term defining a dimensionless coupling constant g_{aff} [31]:

$$\mathcal{L}_{aff} = -ig_{aff}a(\overline{\Psi}_f\gamma_5\Psi_f)\,; \qquad g_{aff} = \frac{\mathcal{C}_{aff}m_f}{f_a} \tag{2.42}$$

where Ψ_f is a fermion Dirac field, $\mathcal{C}_{aff}$ a model-dependent dimensionless coupling constant and m_f the mass of the fermion entering the interaction. So beside axion processes concerning photons, also other processes like **nucleon bremsstrahlung** and **electron bremsstrahlung** are possible: the former is a typical axion like particle production process in neutron stars and Supernovae.
Returning to parameter space bounds, the most immediate astrophysical object from which we can take data is the **Sun**. Axions can be produced in the core and emitted as a flux, whose luminosity L_a is proportional to $g^2_{a\gamma\gamma}$ and the Sun luminosity $L_\odot$ [29]. The solar photon luminosity is fixed, so energy losses due to the Primakoff process require enhanced nuclear energy production and thus enhanced neutrino fluxes. The all-flavor measurements by the Sudbury Neutrino Observatory, together with a standard solar model, imply $L_a \leq 0.1L_\odot$, giving the constraint of

$|g_{a\gamma\gamma}| \leq 4.1 \cdot 10^{-10}$ Gev^{-1}. This is labelled in Fig. 2.3 as "**solar** ν".
A more restrictive limit derives from **globular cluster (GC)** stars that allow for detailed tests of stellar evolution theory. The stars on the horizontal branch (HB) in the color-magnitude diagram have reached **helium burning phase**; if axions undergo Primakoff effect, they take away energy and as a result the duration of the HB phase is shortened. Comparing the number count of HB stars with the number count of Red Giant Branch (RGB) stars, yields the upper bound $|g_{a\gamma\gamma}| \leq 6.6 \cdot 10^{-11}$ Gev^{-1}. This is very important because represents the strongest limit on $g_{a\gamma\gamma}$ for a wide mass range, see Fig. 2.3. The constrain on $g_{a\gamma\gamma}$, may be translated to $f_a > 3.4 \cdot 10^7$ Gev, corresponding to $m_a < 0.5$ eV, for the DFSZ axion model, with E/N = 8/3.
Another important constraint comes from the observation of the **SN1987A Supernova**: the duration of the neutrino burst measured on Earth would have been much shorter if axions interacted quite efficiently with nucleons through nucleon bremsstrahlung. But SN1987A allows to bound the axion photon coupling too if the mass is very small: in fact axions could be produced in the core via Primakoff effect, and then could reconvert into photons in the intergalactic magnetic field. The lack of a γ ray peak in correspondence with the neutrino pulse permits to constrain $|g_{a\gamma\gamma}| \leq 5.3 \cdot 10^{-12}$ GeV^{-1} for $m_a \leq 4.4 \cdot 10^{-10}$ eV.
As in this case, in the same way, large scale B fields exist in astrophysics that can induce axion photon oscillation. B is much smaller than in the laboratory, whereas the conversion region L is much larger. Therefore, while the product BL can be large, realistic sensitivities are usually restricted to very low-mass particles. In this sense, all those green areas on the left in Fig. 2.3 are present: they are upper bounds resulting from various observation of astrophysical objects [29].
Concerning all the blue regions, instead, they are placed in relatively large mass area. The two-photon decay infact, is extremely slow for axions with masses in the CDM regime, but could be detectable for eV masses. But the main difference between blue and green regions is that green ones represent exclusions from astrophysical searches for axions which are **independent** of the fraction of DM that axions make up, while blue represent exclusions from astrophysical searches which **rely** on DM axions. I will not discuss further this upper bounds, more details can be found in [29] while the complete bibliografy for the parameter space in [28]. Although it is instructive to talk about one cosmological constraint, in relation to the hypothesis of axions constituting CDM, concerning **CMB data**. Photons of the CMB could produce axions if they interact with intergalactic magnetic fields, this would lead to distortions in the CMB spectrum. Therefore in the hypothesis of axion CDM that will be explored soon, one of the requests that they must satisfy is to be stable particles. They should have a decay time greater that the age of the universe and so it can be shown that axions **become stable** in the universe time-scale if (in the KSVZ model) the mass is $m_a \leq 20$ eV.
As well as for the various blue regions that indicate direct experimental observation in the hypotesis of axions constituting cold Dark Matter, in these circumstances we have also possible indirect hints and bounds for axion parameter space. For very weak coupling the ultra-light axions are produced non-thermally in the early universe: at these early times, at temperatures well above the QCD phase transition, the axion is effectively massless and the corresponding field can take any value, parameterized by the **"misalignment angle"** θ_i [32]. Later, as the temperature of the primordial plasma falls below the hadronic scale, the axion develops its mass m_a and when it becomes of order the Hubble expansion rate, the axion field will start to oscillate around its mean value $\langle a \rangle = 0$. These coherent and spatially uniform

oscillations correspond to a coherent state of nonrelativistic axion particles, whose contribution to today's **energy density**, in terms of the critical energy density, can be estimated as [29]:

$$\Omega_a h^2 \approx 0.12\left(\frac{f_a}{9\cdot 10^{11} GeV}\right)^{1.165} \mathcal{F}\theta_i^2 \approx 0.12\left(\frac{6\mu eV}{m_a}\right)^{1.165} \mathcal{F}\theta_i^2 \tag{2.43}$$

where H_0 is expressed in terms of $h = 100$ km s^{-1} Mpc^{-1}. $\mathcal{F}$ is instead a factor accounting for anharmonicities in the axion potential. As it can be seen in this equation, Ω_a increases as m_a decreases, thus the axions cannot be too light because the axion energy density must satisfy the observational constraint that the **Dark Matter density** is $\Omega_{DM}h^2 \approx 0.12$ [33]. Assuming $\mathcal{F}\theta_i^2 \sim \mathcal{O}(1)$, the condition $\Omega_a h^2 \leq 0.12$ can be turned into a lower bound to the mass and to f_a:

$$m_a \geq 10^{-6}\ eV\ ; \qquad f_a \leq 10^{12}\ GeV. \tag{2.44}$$

With lower mass values, axions would alone exceed the observed DM density, leading to an "overclosure" of the universe.
In conclusion, what is important from astrophysical and cosmological constraints, is that it can be identified a **preferred region** for the mass. We can therefore take the axion mass to lie approximately in the range:

$$10^{-6}\ eV \leq m_a \leq 10^{-3}\ eV \tag{2.45}$$

and as can be seen in Fig. 2.3, this is the region with the majority experimental effort. Infact, in this region lies all the upper bounds from Haloscope experiments that reached in some cases the model band. Among these figures **ADMX**, the paradigm for haloscope detection, but also **QUAX**: the INFN experiment for axion search.
All methods of detection will be covered in the next section; in the mean time it is worth noticing that lower mass values are still viable if one drops the assumption that $\theta_i^2 \sim \mathcal{O}(1)$, considering small θ_i values. This hypotesis leads to a possible finetuning problem but also to anthropic selection [1, 34]

2.3 Detection techniques

In the previous two sections we discussed about how the axion model comes out from theory and about its potential in solving two of the greatest problems in particle physics. We described also which is the paradigm of Axion detection and production, with the purpose of set stringent limits on its parameter space. After talking about some constraints coming from indirect astrophysical and cosmological experiments, it's now time to approach at the various direct experimental techniques, such as **Light Shining through Walls**, **Helioscopes** and **Haloscopes**: all the red regions in Fig. 2.3.
A common point to the three detection techniques is that they make use of the axion to photons interaction: such a coupling modifies the Maxwell's equations and the propagation of a free axion. If we take the lagrangian that considers only axion and photon we have:

$$\mathcal{L} = \frac{1}{2}(\partial_\mu a)^2 - \frac{1}{2}m_a^2 a^2 - \frac{1}{4}F_{\mu\nu}F^{\mu\nu} + \frac{1}{4}g_{a\gamma\gamma}aF_{\mu\nu}\tilde{F}^{\mu\nu} \tag{2.46}$$

so that if we apply the **Euler Lagrange** equations for photon vector field and for axion field, one obtains the equations of motion in the absence of electromagnetic charges [10]:

$$\begin{aligned} &\nabla \cdot E = g_{a\gamma\gamma} B \cdot \nabla a \\ &\nabla \cdot B = 0 \\ &\nabla \wedge E + \partial_t B = 0 \\ &\nabla \wedge B - \partial_t E = g_{a\gamma\gamma}(E \wedge \nabla a - B\partial_t a), \end{aligned} \tag{2.47}$$

$$(\Box + m_a^2)\, a = -g_{a\gamma\gamma} E \cdot B. \tag{2.48}$$

In Eq. (2.47) the axion field is regarded as a source of electromagnetic fields while in Eq. (2.48) the solution gives the axion field in terms of an electric and a magnetic field. This ambivalence will be exploited in the detection techniques.

2.3.1 LSW and Helioscopes

Let's start with the most tricky of the three: **Light Shining through Walls** experiments are conceptually very simple to understand but in practice they rely on two consequent and dependent interactions. A typical experimental setup it's shown in Fig. 2.3: the sense of the experiment is to use Primakoff process to produce an axion like particle and then inverse Primakoff process to reconvert them in a photon.

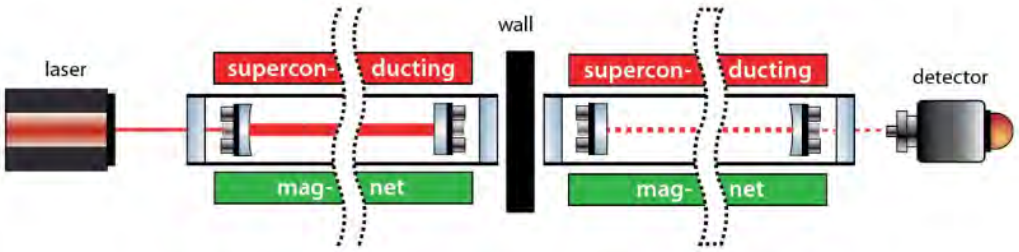

Figure 2.4. [35] Sketch of an LSW experiment.

A photon beam is injected in an optical cavity, in presence of a static magnetic field that provides a virtual photon: If an ALP is successfully produced, it can pass the opaque wall without interacting with it and reach the second cavity. At this point the same procedure is carried out, but in this case the focus is on the ALP-photon conversion. The probability that, starting with a photon ALP conversion, you get another photon is [32]:

$$P(\gamma \to a \to \gamma) = 16 \frac{(g_{a\gamma\gamma} B \omega cos\theta)^4}{m_a^8} sin^2\left(\frac{l_1 m_a^2}{4\omega}\right) sin^2\left(\frac{l_2 m_a^2}{4\omega}\right) \tag{2.49}$$

where ω is the laser frequency, θ the angle between the laser polarization and the static magnetic field B and l_1, l_2 the lengths of the two production regions. By tuning opportunely the ratio l_i/ω, this type of experiments are sensitive to different mass values.
The first such Light Shining through Walls experiment was performed by the **BFRT** (Brookhaven-Fermilab-RochesterTrieste) collaboration, it reached a sensitivity $|g_{a\gamma\gamma}| \leq 6.7{\cdot}10^{-7}$ GeV^{-1} for $m_a \leq 1$ meV. The current best limit, $|g_{a\gamma\gamma}| \leq 3.5{\cdot}10^{-8}$ GeV^{-1} for $m_a \leq 0.3$ meV, has been achieved by the **OSQAR** (Optical Search for

QED Vacuum Birefringence, Axions, and Photon Regeneration) experiment; the **ALPS I** (Any Light Particle Search I) experiment achieved a similar sensitivity too [29].
The probability can be enhanced if optical resonant cavities (Fabry-Perot) are employed in the production and regeneration regions: the experiment **ALPS II** (Any Light Particle Search II) is based on this concept and aims at an improvement of the current laboratory bound on $g_{a\gamma\gamma}$ by a factor $\sim 10^3$. Resonantly enhanced photon regeneration has already been exploited in experiments searching for "radiowaves shining through a shielding". For $m_a \leq 10^{-5}$ eV, the upper bound on $g_{a\gamma\gamma}$ established by the **CROWS** (CERN Resonant Weakly Interacting sub-eV Particle Search) experiment is slightly less stringent than the one set by OSQAR. All this discussed upper bounds are shown in red in Fig. 2.3.
Helioscopes instead exploit essentially the same mechanism as LSW experiments, even if they bypass the first conversion. They exploit a possible well known source of axion: our Sun. As said in section Section 2.2.2, the production mechanism is the Primakoff effect but in this case the role of an external field is played by the Coulomb field of the plasma. An experimental scheme is shown in Fig. 2.5, the photon regeneration takes place in a lab: intense static magnetic fields are applied for the conversion within a movable structure similar to telescopes, pointed towards the Sun. We anticipated that an interaction axion photon has the form like in Eq.

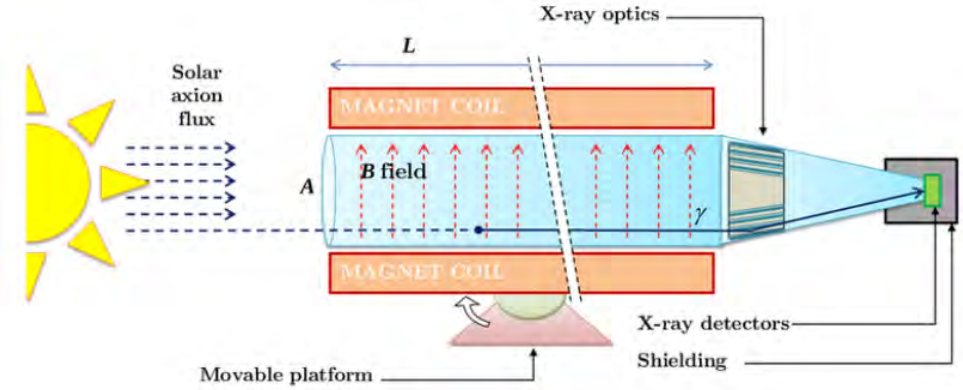

Figure 2.5. [1] Sketch of an Helioscope pointing to the sun with an intense magnetic field and optical readout.

(2.39), this allows us to choose the right direction for the external magnetic field. As **Sikivie** pointed out [7,36], the magnetic field has to be applied in an orthogonal direction with respect to the axion flux so that the direction of the generated photon polarization vector is parallel to B.
From the solar flux, axions with energies in the keV range are produced because the temperature of the core is in this range of energies. Therefore we expect axion convertion into x-ray photons in the lab: modern helioscopes are then equipped with x ray focusing optics and x ray detectors.
The differential flux of ALPs at Earth in the 1-11 keV range, due only to the Primakoff process, is [1]:

$$\frac{d\Phi_a}{dE} = 6.02 \cdot 10^{10} \left(\frac{g_{a\gamma\gamma}}{10^{-10}\ GeV^{-1}} \right)^2 E^{2.481} e^{\frac{-E}{1.205}} \frac{1}{cm^2\ s\ keV} \tag{2.50}$$

where E is the ALP energy in keV and the peak is at about 3 keV.
We expect a large ALP's flux since there is a large number of photons inside the

sun, nevertheless we are searching for "invisible" model with a very small coupling so that the flux is not that high or otherwise the Sun would loose energy too fast with significant impact on its evolution.
The most recent helioscope **CAST** (CERN Axion Solar Telescope) uses a decommissioned LHC dipole magnet on a tracking mount. As it can be seen in Fig. 2.3, CAST has established the limit $|g_{a\gamma\gamma}| \leq 6.6 \cdot 10^{-11}$ GeV^{-1} for $m_a \leq 0.02\cdot$ eV. To cover larger masses, the magnet bores are filled with a gas at varying pressure: limits up to 1.17 eV then allowed CAST to "cross the axion line" for the KSVZ model.
Sensitivity to significantly smaller values of $g_{a\gamma\gamma}$ can be achieved with a next-generation axion helioscope with a much larger magnetic-field cross section: such a prospect should be satisfied by the "International Axion Observatory" (**IAXO**) [29].

2.3.2 Galactic Axion halo

In order to talk about haloscopes we must first justify the meaning of their introduction as a detection technique, we need to talk about all the properties of **galactic DM axions**: "halo" infact stands for the galactic CDM halo that is thought to surround our galaxy.
The two key parameters that we need to describe the DM halo in our galaxy are the **density** distribution $\rho(r)$ and the **energy**, or velocity, distribution. Our problem is luckily simplified becouse in order to talk about a detector localized at earth is sufficient to know only the value of the local DM density and the mean velocity with its dispersion. The **local** DM density ρ_{DM} is estimated to lie in the range $(0.2, 0.56)$ GeV cm^{-3} from several experiments [37] but researches focused on axion detection usually refer to a value of 0.45 GeV cm^{-3} [38]. Another assumption that is usually done is that the axion density equals the DM local density, so $\rho_a = \rho_{DM}$ is employed in all the equations below.
A series of assumptions are made about the velocity distribution too: it is assumed that the galactic halo has **virialized**, so that it reached an equilibrium condition in which the kinetic and potential energies are related by the virial theorem. Following this, the **velocity distribution** is approximately Maxwellian and can be written as [39]:

$$f(v)d^3v = n_a\left(\frac{m_a}{2\pi T}\right)^{\frac{3}{2}} e^{\frac{-m_a v^2}{2T}} d^3v \tag{2.51}$$

with T as the "halo temperature" and where n_a, the axion **number density**, is given by:

$$n_a = \frac{\rho_a}{m_a} \simeq 4.5 \cdot 10^{12}\left(\frac{10^{-4}\ eV}{m_a}\right) cm^{-3}. \tag{2.52}$$

Knowing the velocity distribution it can be calculated the rms velocity of the halo, often called dispersion, that is defined as $\overline{v} = \langle v^2\rangle^{\frac{1}{2}}$ where $\langle v^2\rangle = \int v^2 f(v) d^3v$. From Refs. [39] it is estimated to be $\overline{v} = 270$ km/s that in natural units can be took to be $\overline{v} \sim 10^{-3}$. All this quantities are calculated with respect to the center of our galaxy, but as we know the Earth moves with respect to it with velocity labelled as v_E. As a conseguence the Earth moves inside the CDM halo and an hypotetical haloscope on its surface should experiment an effective axion "wind" with a velocity $v_a = v - v_E$. There are three components that characterize the **Earth's velocity** v_E: the orbital velocity around the Sun, its rotational velocity and the velocity of the Solar System in the galaxy that has a dominant contribution with respect to the other two. The axion wind velocity therefore still follows a Maxwellian distribution, but with a value $\overline{v}_a \simeq 305$ km/s that is still of order $\sim 10^{-3}$.

All this discussion is useful because we can continue with our assumption of **non relativistic** DM particles constituting the halo: in this sense we can identify the energy of an axion with its mass energy, $E_a = m_a$. All this because the halo energy dispersion about the central line is given by:

$$E_a = m_a + \frac{1}{2} m_a \overline{v}_a^2 \simeq m_a[1 + \mathcal{O}(10^{-6})] \tag{2.53}$$

and provided this, the **axion linewidth** is very narrow, its definition is:

$$\frac{dE_a}{E_a} = \frac{m_a \overline{v}_a^2/2}{m_a} \simeq 5.2 \cdot 10^{-7}. \tag{2.54}$$

What is important respect all this properties it's the following quantity: the inverse of the linewidth, that is the ratio of the energy to the energy spread, is called **figure of merit** or **quality factor** of the galactic axion halo and is defined as:

$$Q_a = \frac{m_a}{m_a \overline{v}_a^2/2} \simeq 1.9 \cdot 10^6 \tag{2.55}$$

This quantity characterize the kinetic properties of a generic CDM galactic halo, independently of the axion mass and it will be very important when we will discuss about the power emitted by an axion signal in a microwave cavity in Chapter 3.
Let's introduce here another two quantities that are useful in haloscopes design: axion's **coherence length** and **coherence time**. In order to talk about the former let's consider the De Broglie wavelength of an axion:

$$\lambda_a = \frac{2\pi}{m_a \overline{v}_a} \simeq 6.9 \left(\frac{200\ \mu eV}{m_a} \right) m \tag{2.56}$$

that is of order of some meters. It's really important because we will have microwave cavities with diameters of order some cm so it allows us to treat the axion field uniform in the region of space where our experiment is located. The coherence length is related to λ_a through $\mathcal{O}(1)$ factors so in our case of small cavities the hypothesis of De Broglie wavelenght identified with it holds.
We can think of the coherence length as the region of space in which the axion field can be considered spatially constant, due to the broad oscillations two points in this volume always have approximately the same phase, and it is connected to the coherence time that is the time after which two points within the coherence length will dephase, this because the axion field is not perfectly monochromatic. This quantity is defined as:

$$\tau_a \simeq \frac{2\pi}{m_a} Q_a \tag{2.57}$$

and is very important for haloscopes design because we can think of the interaction between the axion field and a resonant cavity as a pair of **coupled oscillators**: the coupling will hold only for a time $\sim \tau_a$.

2.3.3 Haloscopes

We have finally arrived to the last kind of experiment, the one this thesis is about. As the other two techniques, haloscopes relie on the inverse Primakoff process where now the virtual photon is provided by a static magnetic field.
We will discuss extensively about all haloscopes details, such as microwave cavity

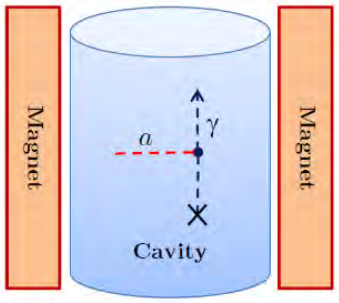

Figure 2.6. [1] Microwave cavity with an applied external magnetic field that provides an axion photon conversion.

and readout electronics, in Chapter 3 but it is important to mention here the main characteristics. A very introductory sketch is reported in Fig. 2.6.

An haloscope is based on the **equality** that holds between the photon frequency and the axion mass $\nu_{res} \simeq m_a$, this derives from the fact that the axion is non-relativistic ($E_a \simeq m_a$) and that after an interaction the photon energy is equal to the axion energy ($\nu_{res} = E_a$) because when a magnetic field is static, it is considered as constituted by many virtual photons, so when a single photon interacts the energy transfer is negligible. Moreover the photon energy and the resonant frequency of the cavity have to be matched, in this sense a **cavity mode** can be excited.
Not all the cavity modes are usefull in our experiment, concerning our case of axion photon interaction we have seen that the lagrangian is of the type of Eq. (2.39). Therefore if $\hat{z}$ is the axis direction of the cavity and the external magnetic field is applied along $\hat{z}$, the only cavity modes that can be excited by an axion are the **transverse magnetic** modes for which the electric field has component along the $\hat{z}$ axis.
Another very important requirement of an haloscope is that the microwave cavity must have the possibility to vary somehow its **resonant frequency** to scan over a range of axion masses. The most intuitive way is to vary the geometric parameters of the cavity, in this sense we will see in further discussions that one possible way is to insert a rod inside the empty volume to modify the resonant frequency of the mode with its movement.
The feasibility of this technique was established in early experiments, like **RBF** (Rochester-Brookhaven-Florida) and UF (University of Florida), of relatively small sensitive volume, setting limits in the range $4.5 < ma < 16.3$ μeV but lacking the sensitivity required to reach the model band [29]. Later, the first generation of **ADMX** achieved sensitivity to KSVZ axions over the mass range $1.9 - 3.3$ μeV. This experiment mploys a NbTi superconducting magnet up to 8 T with a copper microwave cavity with a volume of about 200 L. Inside the cavity there are two movable rods that allow to tune the resonant frequency approximately in the range (0.46 - 2) GHz, that corresponds to the mass range (1.9 - 8.26) μeV [40]. Somewhat later, the ADMX experiment commissioned an upgrade that replaced the microwave HFET amplifiers by nearquantum limited low noise dc SQUID microwave amplifiers and, more recently, with Josephson parametric amplifiers, with noise near quantumlimited too. ADMX has so achieved an unprecedented axion DM sensitivity in the mass range between 2.7 and 4.2 μeV , down to the DFSZ benchmark axion photon coupling over much of the range.
The **HAYSTAC** experiment reported results from a microwave cavity search for DM axions with masses above 20 μeV while **ORGAN** experiment aims to probe

axions over the relatively high-mass range 60 μeV $< m_a <$ 210 μeV exploiting long thin cavities. Then there is **CAPP** that has recently reported results approaching KSVZ sensitivity in the mass range 6.62 – 8.82 μeV and last but not least the **QUAX** experiment, all this limits can be seen in Fig. 2.3.
The first experimental results done with the new haloscope of the QUAX experiment located at Laboratori Nazionali di Frascati of INFN (LNF) have been obtained between november and december 2023. The cavity frequency was varied in a 6 MHz range that corresponds to a previously unprobed mass range between 36.52413 and 36.5511 μeV. No excess was observed in the power spectrum so it was set a limit corresponding to $|g_{a\gamma\gamma}| \leq 0.861 \cdot 10^{-13}$ GeV^{-1} [9].
To finish this introductory part it is very pedagogical to show all the experimental projection on the axion parameter space: they are all reported in Fig. 2.7. Among these there are the proposed **MADMAX** experiment that will place a stack of dielectric layers in a magnetic field in order to resonantly enhance the photon signal, aiming a sensitivity to probe the mass range 40 μeV $< m_a <$ 200 μeV and the proposed **FLASH** (Finuda magnet for Light Axion SearcH) experiment. This project plans to employ the Finuda magnet of 1.1 T for a copper cavity of about 4 m^3 in order to search galactic axions in the mass range 0.5 - 1.5 μeV [41,42].
What is important from this projections tho, is the fact that in the next 10 years more or less all the model band will be covered. This can lead to two scenarios: QCD axion model ruled out by experiment or its discovery resulting in a revolution in particle physics that will shift all the experimental effort to this field.

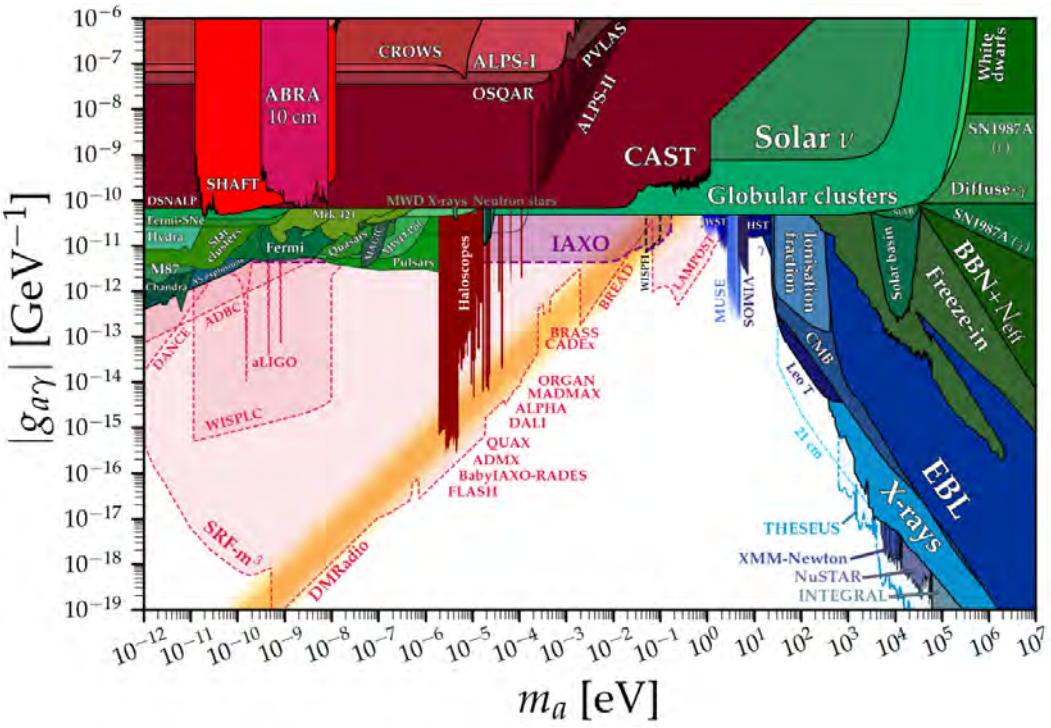

Figure 2.7. [28] Axion parameter space with all the experimental bounds from Fig. 2.3. Semi transparent regions correspond to future experiments. The figure can be reproduced by using the Python notebook available in the Ref, where it can be found also all the references to the data of all the future experiments displayed.

Chapter 3

QUAX experiment

3.1 Radiofrequency

In the previous chapter we overviewed the axion landscape of particle physics, passing through all the theoretical motivations and the experimental effort to discover this new type of physics. Now it's time to go into more details about haloscopes: we need to talk about microwave cavities, magnets, cryogenic systems etc.
For this reason this chapter starts with a detailed description of a resonant cavity, the characterizing part of an haloscope. Moreover, the working frequencies of QUAX are in the microwave range (order 10 GHz) so some radio frequency concepts are introduced. The main goal is to establish a model to describe a resonant cavity from a circuit point of view, for this reason the scattering matrix is introduced. This description leads us to the functions employed for calibrating the experiment. The content of this section is adapted from the textbook of Refs. [43], a standard reference in the field of radio frequency.

3.1.1 Resonant cavities

Resonant cavities are, in their simpliest description, volumes enclosed by conducting surfaces. In this sense, we will firstly find general solutions to Maxwell's equations for the specific cases of TE (transverse electric) and TM (transverse magnetic) wave propagation in cylindrical waveguides. Later on, we will apply a further boundary condition that takes into account the fact that the conducting plates of a cavity are short circuited at both ends. In Fig. 3.1 the geometry of an arbitrary waveguide is shown, it is characterized by conductor boundaries that are parallel to the z axis and is assumed to be infinitely long.

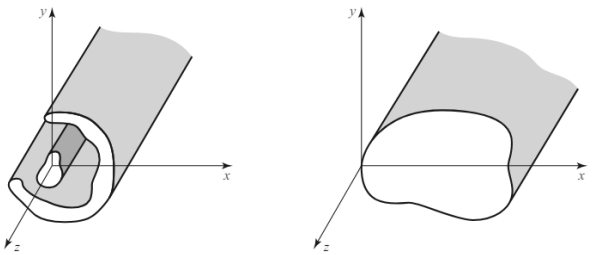

Figure 3.1. [43] On the left a general two conductor transmission line and on right a closed waveguide.

A **waveguide** is a conducting structure made of one ore more conductors. We treat resonant cavities then only TE and TM modes can propagate since only one conductor is present.
Assuming perfect conduction, time harmonic fields with an $e^{j\omega t}$ dependence and wave propagation along the z axis; the electric and magnetic fields can be written as:

$$\begin{aligned}\mathbf{E}(x,y,z) &= [\mathbf{e}(x,y) + \hat{z}e_z(x,y)]e^{-j\beta z} \\ \mathbf{H}(x,y,z) &= [\mathbf{h}(x,y) + \hat{z}h_z(x,y)]e^{-j\beta z}\end{aligned} \tag{3.1}$$

where the wave is propagating in the positive z direction, propagation in the negative z can be obtained simply by replacing the propagation constant β with $-\beta$.
Moreover, assuming that the waveguide region is source free, we can write Maxwell's equations as:

$$\begin{aligned}\nabla \times \mathbf{E} &= -j\omega\mu\mathbf{H}, \\ \nabla \times \mathbf{H} &= j\omega\epsilon\mathbf{E}\end{aligned} \tag{3.2}$$

and these six equations can be solved for the four transverse field components in terms of E_z and H_z as follows:

$$\begin{aligned}H_x &= \frac{j}{k_c^2}\left(\omega\epsilon\frac{\partial E_z}{\partial y} - \beta\frac{\partial H_z}{\partial x}\right), \\ H_y &= \frac{-j}{k_c^2}\left(\omega\epsilon\frac{\partial E_z}{\partial x} + \beta\frac{\partial H_z}{\partial y}\right), \\ E_x &= \frac{-j}{k_c^2}\left(\beta\frac{\partial E_z}{\partial x} + \omega\mu\frac{\partial H_z}{\partial y}\right), \\ E_y &= \frac{j}{k_c^2}\left(-\beta\frac{\partial E_z}{\partial y} + \omega\mu\frac{\partial H_z}{\partial x}\right),\end{aligned} \tag{3.3}$$

where $k_c^2 = k^2 - \beta^2$ is defined as the cutoff wave number: its name will be clear later. k is instead the wave number of the medium filling the guide: $k = \omega\sqrt{\mu\epsilon}$.
Now the solutions to the transverse fields are obtained imposing the field configurations of the various modes and the boundary conditions. We will focus, as said, to the **Circular waveguide**: Fig. 3.2 shows the geometry of such a guide with inner radius a.

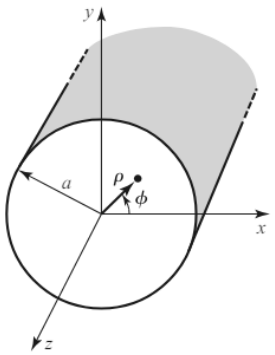

Figure 3.2. [43] Geometry of a circular waveguide.

Because cylindrical geometry is involved, it is appropriate to employ cylindrical coordinates, in the same way as before we can derive the cylindrical components of the transverse fields from the longitudinal components:

$$\begin{aligned} E_\rho &= \frac{-j}{k_c^2}\left(\beta\frac{\partial E_z}{\partial \rho} + \frac{\omega\mu}{\rho}\frac{\partial H_z}{\partial \phi}\right), \\ E_\phi &= \frac{-j}{k_c^2}\left(\frac{\beta}{\rho}\frac{\partial E_z}{\partial \phi} - \omega\mu\frac{\partial H_z}{\partial \rho}\right), \\ H_\rho &= \frac{j}{k_c^2}\left(\frac{\omega\epsilon}{\rho}\frac{\partial E_z}{\partial \phi} - \beta\frac{\partial H_z}{\partial \rho}\right), \\ H_\phi &= \frac{-j}{k_c^2}\left(\omega\epsilon\frac{\partial E_z}{\partial \rho} + \frac{\beta}{\rho}\frac{\partial H_z}{\partial \phi}\right). \end{aligned} \tag{3.4}$$

Transverse electric modes (TE) are defined as $E_z = 0$ and so we need to find only H_Z, the latter is a solution to the wave equation:

$$\nabla^2 H_z + k^2 H_z = 0. \tag{3.5}$$

If, $H_z(\rho, \phi, z) = h_z(\rho, \phi)e^{-j\beta z}$, we can express the equation in cylindrical coordinates:

$$\left(\frac{\partial^2}{\partial \rho^2} + \frac{1}{\rho}\frac{\partial}{\partial \rho} + \frac{1}{\rho^2}\frac{\partial^2}{\partial \phi^2} + k_c^2\right)h_z(\rho, \phi) = 0. \tag{3.6}$$

Using the method of separation of variables, factorizing $h_z(\rho, \phi) = R(\rho)P(\phi)$ and substituting it in the differential equation, the general solution is found:

$$P(\phi) = Asin(n\phi) + Bcos(n\phi) \tag{3.7}$$

where n is an integer number because the solution to h_z must be periodic in ϕ due to the cilindrical simmetry of the system.
Conversely, the differential equation for $R(\rho)$ is recognized as Bessel's differential equation; the solution to it is then:

$$R(\rho) = CJ_n(k_c\rho) + DY_n(k_c\rho) \tag{3.8}$$

where $J_n(x)$ and $Y_n(x)$ are respectively the Bessel functions of first and second kinds. Thanks to the simmetry of the system, the solution with $Y_n(x)$ is physically unacceptable because becomes infinite for $\rho = 0$. The solution for h_z can then be simplified:

$$h_z(\rho, \phi) = [Asin(n\phi) + Bcos(n\phi)]J_n(k_c\rho) \tag{3.9}$$

where the C constant has been absorbed into the A and B constants. We must still determine the cutoff wave number k_c. This can be achieved by enforcing the boundary condition that the two tangential components of the field must vanish on the waveguide wall. By our initial assuption we know that $E_z = 0$ so this lead us to the another condition $E_\phi(\rho = a, \phi) = 0$. To satisfy this last one condition we must have:

$$J_n^{'}(k_c a) = 0 \tag{3.10}$$

where $J_n^{'}$ is the first derivative of J_n. If the roots of $J_n^{'}(x)$ are defined as $p_{nm}^{'}$, so that $J_n^{'}(p_{nm}^{'}) = 0$, where $p_{nm}^{'}$ is the mth root of $J_n^{'}$, then k_c must have the value:

$$k_{c_{nm}} = \frac{p_{nm}^{'}}{a} \tag{3.11}$$

where values of p'_{nm} are given in mathematical tables shown in Refs. [43]. What is important in all this discussion is that all the TE_{nm} modes are labelled by this two subscripts, they are defined by the cutoff wave number where n refers to the number of circumferential (ϕ) variations and m refers to the number of radial (ρ) variations. The propagation constant is instead:

$$\beta_{nm}^{TE} = \sqrt{k^2 - k_c^2} = \sqrt{k^2 - \left(\frac{p'_{nm}}{a}\right)^2}, \tag{3.12}$$

and now is clear why the name cutoff was used: β_{nm} is real when $k > k_{c_{nm}}$ so the waves can propagate. On the contrary, in the other case, the corresponding mode becomes evanescent since β_{nm} becomes pure imaginary and the propagation factor $e^{-j\beta z}$ takes the form of a decaying exponential. Moreover a cutoff frequency can be defined:

$$f_{c_{nm}}^{TE} = \frac{k_c}{2\pi\sqrt{\mu\epsilon}} = \frac{p'_{nm}}{2\pi a\sqrt{\mu\epsilon}}. \tag{3.13}$$

The first TE mode to propagate is the mode with the smallest p'_{nm}, from tables [43] is seen to be the TE_{11} mode. This mode is therefore the dominant circular waveguide mode and the one most frequently used. Because $m \geq 1$, there is no TE_{10} mode, but there is a TE_{01} mode.
Finally, having found the solution for $h_z(\rho, \phi)$ we can write all the transverse field components for the TE_{nm} modes; I will not write explicitly the solutions, they can be found in Refs. [43].
The difference with **transverse magnetic modes** (TM) is that this ones are defined for $H_z = 0$ so in this case we need to find E_z. The procedure is the same as before and lead us to this soluzion for $e_z(\rho, \phi)$:

$$e_z(\rho, \phi) = [Asin(n\phi) + Bcos(n\phi)]J_n(k_c\rho). \tag{3.14}$$

This is still the point to apply the boundary conditions, now $E_z(\rho = a, \phi) = 0$ can be directly applied to e_z, giving us the condition:

$$k_{c_{nm}} = \frac{p_{nm}}{a} \tag{3.15}$$

where p_{nm} are the mth roots of the nth bessel function of the first kind J_n and not of his derivative like before. In this case too it can be defined the propagation constant and the cutoff frequency that are determined in terms of $k_{c_{nm}}$:

$$\begin{aligned} \beta_{nm}^{TM} &= \sqrt{k^2 - \left(\frac{p_{nm}}{a}\right)^2}, \\ f_{c_{nm}}^{TM} &= \frac{p_{nm}}{2\pi a\sqrt{\mu\epsilon}}. \end{aligned} \tag{3.16}$$

All the discussion about the available modes inside the cavity is the same as in the TE case. Also in ths instance I will not report the explicit solution of all the transverse modes: it is only necessary to insert the solution for $e_z(\rho, \phi)$ inside Eq. (3.4), it is done in Ref. [43].
In order to describe resonant cavities the last step is missing: it is sufficient to impose one additional boundary condition to the system. A **cylindrical cavity**

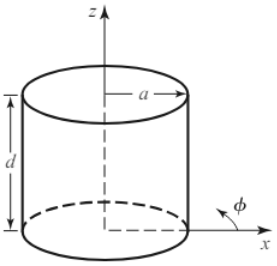

Figure 3.3. [43] Geometry of a cylindrical resonant cavity.

resonator can infact be constructed from a section of circular waveguide shorted at both ends. In Fig. 3.3 is shown the geometry of the system.

Our discussion is simplified by the fact that we can now start from the solutions we found for the circular waveguide modes, they already satisfy the necessary boundary conditions on the wall of the circular waveguide. Let's write the solutions for the transverse electric fields E_ρ and E_ϕ of the TE_{nm} and TM_{nm} circular waveguide mode, that can be written as:

$$\mathbf{E}_t(\rho,\phi,z) = \mathbf{e}(\rho,\phi)(A^+ e^{-j\beta_{nm}z} + A^- e^{j\beta_{nm}z}). \tag{3.17}$$

Here $\mathbf{e}(\rho,\phi)$ represents the transverse variation of the mode while A^+ and A^- the arbitrary amplitudes of the forward and backward traveling waves.
Recalling that the propagation constants are the ones from Eq. (3.12) and Eq. (3.16) respectively for TE_{nm} and TM_{nm} modes, in order to have $\mathbf{E}_t = 0$ at $z = 0$ and $z = d$ we need to choose $A^+ = A^-$ and $A^+ sin\beta_{nm}d = 0$. This means in other words that:

$$\beta_{nm}d = \ell\pi, \qquad \ell = 0, 1, 2, 3... \tag{3.18}$$

and this implies that the waveguide must be an integer number of half guide wavelengths long. Therefore the consequence is that now we have an additional subscript for the modes which represents the variations along z from 0 to d. It is now time to define the most important quantity that we will need, the **resonant frequency of the modes**. For $\mathrm{TE}_{nm\ell}$ is:

$$f^{TE}_{nm\ell} = \frac{c}{2\pi\sqrt{\mu_r\epsilon_r}}\sqrt{\left(\frac{p'_{nm}}{a}\right)^2 + \left(\frac{\ell\pi}{d}\right)^2}, \tag{3.19}$$

while for $\mathrm{TM}_{nm\ell}$ is:

$$f^{TM}_{nm\ell} = \frac{c}{2\pi\sqrt{\mu_r\epsilon_r}}\sqrt{\left(\frac{p_{nm}}{a}\right)^2 + \left(\frac{\ell\pi}{d}\right)^2} \tag{3.20}$$

and this two equations tell us what are the dominant modes for a resonant cavity. The dominant TE mode is the TE_{111} while for TM mode is the TM_{010} one. This two equations are obviously useful for the design of circular cavity resonators: they show us what modes can be excited at a given frequency for a given cavity size. Although we need to remember the cutoff frequencies: only the modes with $f > f_{c_{nm}}$ can be excited inside a cavity, below this value the propagation constant becomes pure imaginary and the waveguide modes are evanescent, the electromagnetic field decays

exponentially with the distance.
One last important thing which can be noticed from the resonant frequency expressions is that they vary with the inverse of the geometric dimensions: this explains the fact that smaller cavity volumes are needed to probe higher axion masses, that correspond to higher frequencies.
In conclusion of the subsection it is useful to give a visual demonstration of one electromagnetic mode inside a cylindrical cavity, in particular the one that is used in the QUAX experiment. In Fig. 3.4 is shown a simulation for the TM_{010} mode, at left is depicted the electric field while at right the magnetic one.

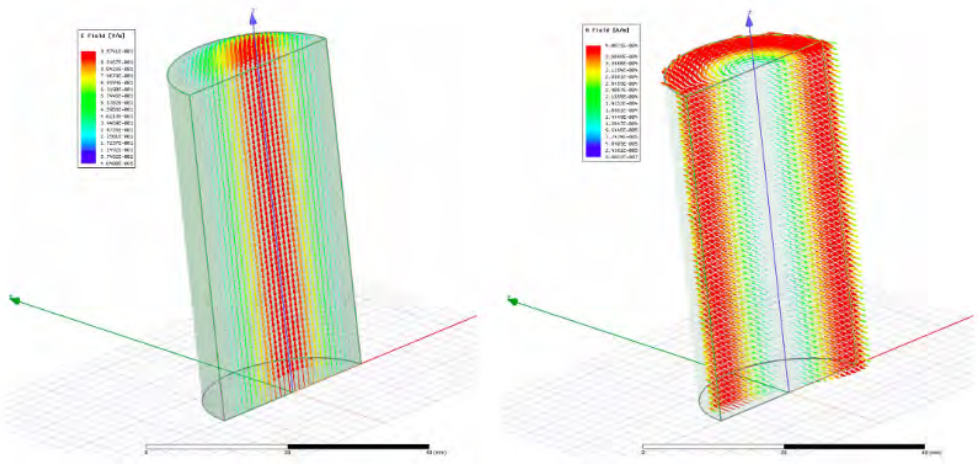

Figure 3.4. A simulation of the fields of TM_{010} mode. Field lines of electric (left) and magnetic (right) fields are drawn. The pictures are provided by Ing. Simone Tocci and obtained with the ANSYS-HFSS software[56] .

Red arrows correspond to regions where the field is more intense and only half of the cavity is shown. This picture is useful because we can have a concrete example of the role of the three subscripts we discussed about. This mode has $\ell = 0$ so as can be seen the electric field has no variation along the z direction. Moreover, it has $n = 0$ and $m = 1$ so there is no variation in the ϕ coordinate: the field is maximum at $\rho = 0$ and falls off until it reaches a null value at $\rho = a$. One important thing that will be useful later is that all the modes with $\ell = 0$ don't depend on the length d of the cavity and so scale only with the radius with a dependence a^{-1}, as can be seen in Eq. (3.19) and Eq. (3.20). This will be crucial when discussing about the way to change the resonant frequency of the cavity.
But why is it the favourite mode utilized in the QUAX experiment and in all the conventional haloscopes? Conventional haloscopes exploit the axion photon interaction and in the previous chapter we saw in Eq. (2.39) that the interaction lagrangian is proportional to $\mathbf{E}\cdot\mathbf{B}$, where $\mathbf{E}$ is the electric field of the excited resonant mode and $\mathbf{B}$ is the external static magnetic field. The external B field it is indeed oriented along the axis of the cylindrical cavity: in this sense the interaction can be maximized by the field lines of the TM_{010} where E is parallel to the z axis and maximum at $\rho = 0$.

3.1.2 Parametrization of a resonant cavity

After describing a resonant cavity from an electromagnetic point of view, it is now time to characterize it from the circuital one to underline its main properties

and quantities.
Therefore the cavity will be parametrized as a **parallel RLC circuit**, that behaves as a resonator. Lumped-element circuit theory is assumed, and the calculations are made in phasor notation.

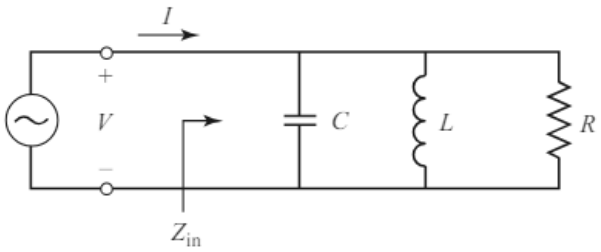

Figure 3.5. [43] A parallel RLC circuit.

The parallel RLC resonant circuit, shown in Fig. 3.5, has an imput impendance that is:

$$Z_{in} = \left(\frac{1}{R} + \frac{1}{j\omega L} + j\omega C\right)^{-1} \tag{3.21}$$

and the complex power delivered to the resonator is:

$$P_{in} = \frac{1}{2} Z_{in} |I|^2 = \frac{1}{2} |V|^2 \frac{1}{Z_{in}^*} = \frac{1}{2} Z_{in} \frac{|V|^2}{|Z_{in}|^2}. \tag{3.22}$$

Recalling that the real power dissipated in the circuit and the electric and magnetic energies stored in the resonator are:

$$\begin{aligned} P_{loss} &= \frac{1}{2}\frac{|V|^2}{R} \\ W_e &= \frac{1}{4}|V|^2 C \\ W_m &= \frac{1}{4}|V|^2 \frac{1}{\omega^2 L} \end{aligned} \tag{3.23}$$

our expression for the complex power becomes:

$$P_{in} = P_{loss} + 2j\omega(W_m - W_e), \tag{3.24}$$

while the impendance:

$$Z_{in} = \frac{2P_{in}}{|I|^2} = \frac{P_{loss} + 2j\omega(W_m - W_e)}{\frac{1}{2}|I|^2}. \tag{3.25}$$

Resonance occurs when $W_e = W_m$ and correspondigly the input impedance at resonance is $Z_{in} = R$ which is purely real. This condition implies also that the resonant frequency, ω_0, can be defined as:

$$\omega_0 = \frac{1}{\sqrt{LC}}. \tag{3.26}$$

Another very important quantity is the **quality factor** that is defined as the ratio of the energy stored in the cavity and the power dissipated by it:

$$Q = \omega \frac{W_m + W_e}{en./sec} \tag{3.27}$$

and for the parallel resonant circuit, evaluated at its resonance, can be expressed as:

$$Q = \omega_0 \frac{2W_m}{P_{loss}} = \omega_0 RC = \frac{R}{\omega_0 L}. \tag{3.28}$$

This quantity is important because it quantifies the losses of the system, that can be conductor, dielectric or radiation losses (all due to R). It is very useful because it also quantifies the width of the resonance curve of a resonator in its power spectrum. Until now we treated only the isolated resonator, so the quality factor that we wrote is defined as the **unloaded** quality factor Q_0 and corresponds to the intrinsic Q factor of the system.
Nevertheless, in an experiment, our system needs to the coupled to other circuit elements in order to be fed and measured. This configuration has the result of lowering the quality factor because external elements introduce additional losses. Therefore the whole system has now an external quality factor too, Q_{ext}, and the combination of the two is the loaded quality factor, Q_L:

$$\frac{1}{Q_L} = \frac{1}{Q_0} + \frac{1}{Q_{ext}}. \tag{3.29}$$

Now with this two definitions of the resonant frequency and quality factor we can modify the expression of the input impendance of Eq. (3.21):

$$Z_{in} = \frac{j\omega RL}{R - \omega^2 RLC + j\omega L} = \frac{R}{1 + jQ_0\delta} \tag{3.30}$$

where now δ is:

$$\delta = \frac{\omega}{\omega_0} - \frac{\omega_0}{\omega}. \tag{3.31}$$

As said, our system needs to be coupled to an external line in order to be fed and in order to have an output signal. In our whole scheme, the cavity will be parametrized as a parallel RLC circuit because the walls are short-circuited for construction while two antennas will be coupled with it. The **coupling of the antennas** can be schematized as two ideal transformers, in the following i will not make an exhaustive discussion about it but i will underline the most important properties of this couplings because we will need them in the making of the experiment. A detailed treatment can be found in Ref. [11]

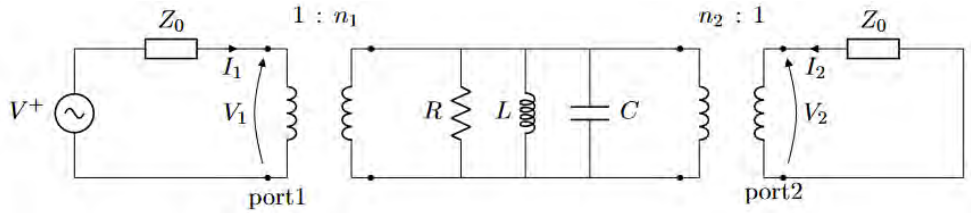

Figure 3.6. [11] Equivalent circuit of the cavity, assumed as a parallel RLC, and the exitation of the antennas, schematized as transformers.

In Fig. 3.6 is schematized the parametrized circuit: this is the particular case in which the device is excited from port 1, where an ideal generator has been placed. The ciruit can be further simplified and this is done from the generator point of view. In our specific case the ratio of the windings between the cavity and the second

antenna is set to $n_2 : 1$, this lead us to consider the second port as an impedance in parallel to the cavity. Using the relations between voltages and currents of an ideal trasformator, we can calculate V_{Cav}, the voltage of the parallel RLC, using the voltage and the current of port 2:

$$V_{Cav} = n_2 Z_0 I_{Cav} \frac{n_2}{1} = Z_2 I_{Cav} \tag{3.32}$$

where $Z_2 = n_2^2 Z_0$ is the impendance seen by the cavity looking towards port 2. Iterating this procedure, the impedance seen by the generator looking towards port 1 is the parallel between Z_{Cav} and Z_2 times $\frac{1}{n_1^2}$ and the resulting equivalent circuit is shown in Fig. 3.7.

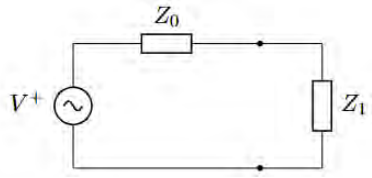

Figure 3.7. [11] Final equivalent circuits of the system formed by resonant cavity and antennas.

Before evaluating the impedance Z_1 it is very useful and instructive to map the arbitrary constants n_1 and n_2 into two observable quantities. We will refer now to the coupling coefficients k_1 and k_2 that are defined as the ratio of the power dissipated in the external circuitry and the power dissipated inside the cavity:

$$k_1 = \frac{P_1}{P_{Cav}}; \quad k_2 = \frac{P_2}{P_{Cav}} \tag{3.33}$$

but in general if one defines an external quality factor with the power dissipated by external circuit, Q_{ext}, the common definition for one coupling is:

$$k = \frac{Q_0}{Q_{ext}} \tag{3.34}$$

where if we use the definition for the loaded quality factor as in Eq. (3.29) we get:

$$Q_L = \frac{Q_0}{1+k}. \tag{3.35}$$

That will be very useful later in this work.

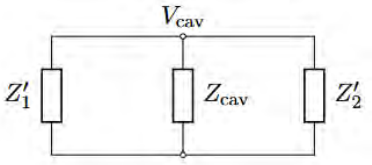

Figure 3.8. [11] Equivalent circuit as seen from the cavity, for the evaluation of k_1 and k_2.

If now we want to evaluate the two couplings of our system, the equivalent circuit seen from the cavity of Fig. 3.8 helps us to evaluate them. In this case, Z'_1 and Z'_2

are the impedances seen by the cavity that are:

$$\begin{aligned} Z_1' &= n_1^2 Z_0 \\ Z_2' &= n_2^2 Z_0. \end{aligned} \tag{3.36}$$

They are both in parallel with Z_{Cav} so the voltage at their edges is the same and is equal to V_{Cav}. From circuit theories, time averaged powers can be calculated as in Eq. (3.22), thus for our equivalent circuit they are:

$$\begin{aligned} P_1 &= \frac{1}{2}\frac{|V_{Cav}|^2}{n_1^2 Z_0} \\ P_2 &= \frac{1}{2}\frac{|V_{Cav}|^2}{n_2^2 Z_0} \\ P_{Cav} &= \frac{1}{2}\frac{|V_{Cav}|^2}{R} \end{aligned} \tag{3.37}$$

where the power dissipated by the cavity is real and only due to the resistance R. Thanks to them, we can now calculate the coupling coefficients:

$$k_1 = \frac{P_1}{P_{Cav}} = \frac{R}{n_1^2 Z_0}; \qquad k_2 = \frac{P_2}{P_{Cav}} = \frac{R}{n_2^2 Z_0} \tag{3.38}$$

so that finally we can calculate the impedance Z_1 seen by the generator looking towards port 1 that is the parallel between Z_{Cav} and Z_2 times $\frac{1}{n_1^2}$, all is represented in the equivalent circuit of Fig. 3.7:

$$Z_1 = \frac{Z_{Cav}//n_2^2 Z_0}{n_1^2} = Z_0 k_1 \left(\frac{\frac{1}{k_2} \cdot \frac{1}{1+jQ_0\delta}}{\frac{1}{k_2} + \frac{1}{1+jQ_0\delta}} \right) = \frac{Z_0 k_1}{1 + k_2 + jQ_0\delta} \tag{3.39}$$

3.1.3 Scattering matrix of a resonant cavity

In the previous subsection we schematized our whole system from a circuital point of view, identifying its main charactristics and properties. Nonetheless one problem still holds, networks in radio frequency regime cannot be treated with lumped element circuit theory. The problem is that wavelengths of electromagnetic signals are comparable with the size of the circuit elements. Complications come because we don't have unique voltage and current values at every point of a given branch, so a distributed element theory has to be taken into account. In the following therefore it will be used the formalism said of the **scattering matrix**.
As in the Ref. [43] equivalent voltages and currents can be defined for an arbitrary lossless waveguide. In this description all the quantities are expressed in phasor form and are complex quantities, while z is taken as the direction of propagation:

$$\begin{aligned} V(z) &= V_0^+ e^{-j\beta z} + V_0^- e^{j\beta z} \\ I(z) &= I_0^+ e^{-j\beta z} - I_0^- e^{j\beta z} \end{aligned} \tag{3.40}$$

where $V_0^{\pm}$ and $I_0^{\pm}$ are the complex amplitudes of the incident and reflected waves and thanks to them we can calculate also the impedance of the line, that is defined as:

$$Z_0 = \frac{V_0^+}{I_0^+} = \frac{V_0^-}{I_0^-} \tag{3.41}$$

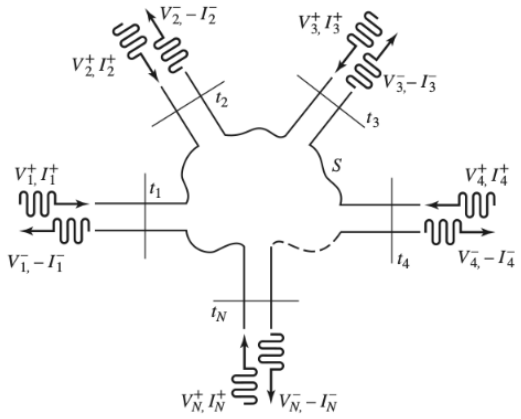

Figure 3.9. [43] An arbitrary N port microwave network.

In Fig. 3.9 is shown a completely generic **N port network**, any kind of waveguide or trasmission line can converge in a port. For every port we have an associated phase reference plane t_n, this corresponds to the plane where the coordinate of the direction of propagation of the nth line is zero: $z_n = 0$. For every port we have the voltage amplitude of the incident wave entering the port, V_n^+, and the reflected amplitude V_n^-; the same goes for the two currents $I_n^{\pm}$. So that we can calculate the total current and voltage at one generic plane t_n:

$$\begin{aligned} V_n(Z_n = 0) &= V_n^+ + V_n^- \\ I_n(Z_n = 0) &= I_n^+ - I_n^- \end{aligned} \tag{3.42}$$

The principle around which an n port network works is that the voltage outgoing from the nth port is due to a fraction of the incident wave into the same port and a fraction of the incident waves entering the network from all the other ports. Following this scheme, the scattering matrix relates all the reflected waves with the incident ones in this simple way:

$$[V^-] = [S]\,[V^+]\,, \tag{3.43}$$

where the single elements of the matrix are:

$$\begin{bmatrix} V_1^- \\ V_2^- \\ \vdots \\ V_N^- \end{bmatrix} = \begin{bmatrix} S_{11} & S_{12} & \cdots & S_{1N} \\ S_{21} & & & \vdots \\ S_{N1} & \cdots & & S_{NN} \\ \vdots & & & \end{bmatrix} \begin{bmatrix} V_1^+ \\ V_2^+ \\ \vdots \\ V_N^+ \end{bmatrix}$$

Figure 3.10. [43] The scattering matrix [S] of the microwave network that relates reflected and incident voltages.

A specific element of the scattering matrix can be determined as:

$$S_{ij} = \left.\frac{V_i^-}{V_j^+}\right|_{V_k=0, k\neq j} \tag{3.44}$$

and can be experimentally obtained by driving a port j with a voltage V_j^+ while the amplitude V_i^- is measured at port i; all this is implemented after matching all the other k ports so that neither incoming V_k^+ or reflected V_k^- are present in the experimental scheme. This formalism is very useful because this setup will be used later in the experiment. For example one can measure all the reflection coefficients S_{ii} by matching all the other ports except the i one; while in the same sense all the transmission coefficients S_{ij} can be calculated by injecting a wave from port j and measuring the ouput from the port i, matching all the others. In this context, a transmission line is said to be matched when ended with a load impedance equal to its characteristic impedance, so that the reflection coefficient is zero.
It is now time to put aside the general case and to talk about our specific case. In our experimental setup we have our resonant cavity that is coupled with the outside through two antennas. Both the ports of the cavity are connected via two transmission line to a **vector network analyzer (VNA)** that provides and measures the power delivered to and from the cavity. The key role of the VNA will be described when dealing about the experimental setup in Section 3.3, now the important thing is that we restricted to a 2 port network that has this scattering matrix:

$$[S] = \begin{bmatrix} S_{11} & S_{12} \\ S_{21} & S_{22} \end{bmatrix} \tag{3.45}$$

where in our specific case $S_{12} = S_{21}$ because we have a reciprocal network, meaning that we don't have a preferred direction for the system inspection.
Remembering all the discussion done in the previous subsection, dealing with the resonant cavity coupled with two antennas, we can now calculate the scattering parameters of our system. From its definition, S_{11} is the reflection coefficient Γ at port 1, we refer to Fig. 3.7 for our calculations: Z_0 is considered a lossless transmission line that is terminated on a load Z_1 that we calculated in Eq. (3.39). Moreover, the voltage contribution to port 1 comes both from an incident and a reflected wave $V_1 = V_1^+ + V_1^-$, with all this ingredients we can now calculate our reflection coefficient at port 1:

$$S_{11} = \left.\frac{V_1^-}{V_1^+}\right|_{V_2^+=0} = \frac{Z_1 - Z_0}{Z_1 + Z_0} = \frac{k_1 - (1 + k_2 + jQ_0\delta)}{1 + k_1 + k_2 + jQ_0\delta}. \tag{3.46}$$

Before evaluating the transmission coefficient it is immediate to calculate the other reflection coefficient S_{22}. Thanks to the symmetry of the configuration, this is easily found by swapping the roles of k_1 and k_2 in the expression of S_{11}:

$$S_{22} = \frac{k_2 - (1 + k_1 + jQ_0\delta)}{1 + k_1 + k_2 + jQ_0\delta}. \tag{3.47}$$

Last but not least is the S_{21} coefficient, port 2 must be again matched to have V_2^+ so the only contribution comes from V_2^- that is calculated using transformer laws as we used in the model of Fig. 3.6, combining the voltages from the two different transformers it is found:

$$V_2 = \frac{V_{Cav}}{n_2} = \frac{n_1}{n_2} V_1. \tag{3.48}$$

By definition of S_{21} the system is injected from port 1 and in this case we have both the contribution, $V_1 = V_1^+ + V_1^- = V_1^+(1 + \Gamma)$, where $\Gamma = S_{11} = V_1^+/V_1^-$. Therefore we can now use this value for V_1 in Eq. (3.48) and finally evaluate our transmission

coefficient using its definition:

$$S_{21} = \frac{V_2^-}{V_1^+}\bigg|_{V_2^+=0} = \frac{n_1}{n_2}(1+S_{11}) = \frac{2\sqrt{k_1 k_2}}{1+k_1+k_2+jQ_0\delta}. \tag{3.49}$$

The discussion for the last parameter is not relevant, because as we stated before our network is reciprocal so in our experimental scheme we have $S_{21} = S_{12}$.
A more detailed description of this model can be found in Ref. [11], I wasn't exhaustive but I underlined the most important elements because all this coefficients will have a key role when dealing the calibrations of the QUAX experiment, and therefore the majority of my experimental activity.

3.2 Haloscopes in practice

In the previous section we discussed about all the radiofrequecy concepts we need, we ended up with the scattering parameters of a 2 port microwave cavity that we will measure during the experiment in order to calibrate our whole system. This section is, conversely, concentrated on how to detect an axion signal; therefore it will exploit all the key properties of an **haloscope**.
An axion haloscope relies on the interaction of Eq. (2.39) to locally convert the axion CDM energy density into an observable electromagnetic signal, which is enhanced by the large local density, by the coherence of the axion field oscillations, and finally by the application of a large external magnetic field.
Following the introduction of the working principle of an haloscope, the two best figure of merit in axion detection will be presented, such as the power of the produced photon and the scan rate. In the end it will be treated also the way to find a possible axion signal and how to enhance it.
In this case too, my discussion will be only an overview about all the essential physics we need. For a more comprehensive discussion please refer to Refs. [10,44].

3.2.1 QUAX collaboration

An axion haloscope is a cryogenic, tunable high-Q microwave cavity immersed in a strong magnetic field and coupled to a low-noise receiver. The Quax collaboration between LNF and LNL exploits two different ways to detect and axion from the CDM halo, we will treat in detail the mode of operation of the QUAX experiment in the Laboratori Nazionali di Frascati where it runs in the ADMX configuration, i.e. with an **empty cavity**. Later on in the end of this subsection we will have a brief digression about the other configuration, the one with a **magnetic sample** inside the cavity as implemented in the Laboratori Nazionali di Legnaro.

In Fig. 3.11 are shown the basic elements of an haloscope, we will start by dealing with the role of the **magnetic field**. We already stated that in an haloscope we have the axion photon conversion schematized as in Fig. 2.2 where one external photon line of the inverse primakoff process is substituted by an external static magnetic field. A classical electromagnetic field corresponds to a large density of virtual photons. Removing a single photon does not appreciably change the energy of this field configuration. Thus in a Primakoff process the incoming axion scatters elastically and emerges as a photon with the same total energy, and polarization parallel to the applied magnetic field as Eq. (2.39) suggests.
We already saw in Eq. (2.47) that the axion field is regarded as a source of

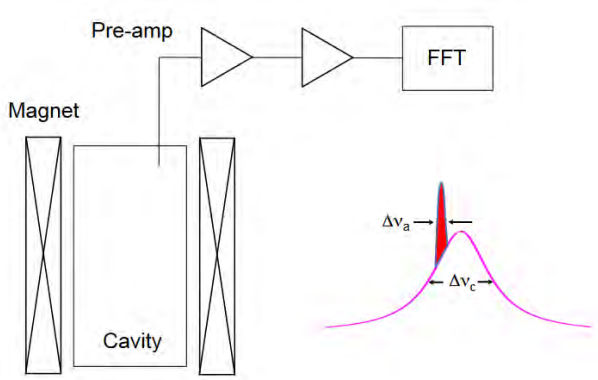

Figure 3.11. [44] Schematic of the microwave cavity search for DM axions. The axion signal is designated by the narrow peak (red) within the bandpass of the cavity (pink).

electromagnetic fields: in our qualitative discussion it's suffient to note that in the presence of large static magnetic field B_0, a homogeneous oscillating axion field induces an electric field oscillating at the same frequency ν_a with an amplitude:

$$E_0 \sim g_{a\gamma\gamma} B_0 a_0. \tag{3.50}$$

Unforuntately, this value of the electric field is still too small to be detectable in a reasonable experiment because of the very weak coupling, although with the enhancement of a strong magnetic field ($B_0 \sim 10$T) and with an high density of axions in the CDM halo. We have therefore to consider the effect of the enhancement of the haloscope signal by the **coherence of axion field oscillations**.
In our experiment we have enclosed the high field region in a microwave cavity with resonant frequency ν_a. As treated before, microwave resonators have many different resonant modes but just for now let's treat a simple model where the axion field and cavity mode are a pair of **coupled oscillators**. By assumption the axion field and cavity mode have the same frequency so the only other useful parameters are the oscillator linewidths $\Delta\nu_a$ and $\Delta\nu_c$ and their mutual coupling k.
We have two limits for this model: the strong coupling ($k \gg \Delta\nu_a, \Delta\nu_c$) where we can neglect damping entirely so the equations of motion are easy to solve and the oscillators exchange energy at the beat frequency k. However this is not the limit in which the haloscope operates, let's assume we have the nominal parameters $m_a = 20\mu$eV and $B_0 = 10$ T; from Eqs. (2.56) and (2.57) we have $\Delta\nu_a = \tau_a^{-1} = 1/(200\mu s)$ and as we will see we have $\Delta\nu_c \gg \Delta\nu_a$ (as illustrated in Fig. 3.11). This means that the lifetime of an excitation in the cavity $\tau_c \sim \Delta_{\nu_c}^{-1}$ will always be shorter than the coherence time of the axion. Using the nominal parameters $m_a = 20\mu$eV and $B_0 = 10$ T in Eq.(3.50) and adopting natural units, we obtain $k = (g_{a\gamma\gamma} B_0)/2\pi \sim 1/(3.5 \text{ days})$. The axion and cavity mode are then exceptionally weakly coupled. What happens is that the amplitude of the cavity field oscillations will grow coherently until time $t = \tau_c$ after which the power dissipated in the cavity will balance the incoming axion conversion power. Therefore we can approximate the behavior in this regime by just cutting off the slow dynamics of the strongly coupled solution at $t = \tau_c$; this lead us to an amplitude for the induced electric field like:

$$E_0 \sim g_{a\gamma\gamma} B_0 a_0 Q_L, \tag{3.51}$$

that is just Eq.(3.50) but enhanced by the **cavity quality factor** Q_L.
This is the first time that we encounter a key feature of all the haloscopes, the

optimal value for Q_L is infact Q_a so this is an experimental limit. It is then not useful to increase indefinitely the cavity quality factor further beyond this point because the haloscope would be limited by the finite coherence time of the axion field itself.
It should however be noted that in classical physics the cavity does not amplify the axion photon interaction, it is only the volume where the interaction takes place. Large Q_L just allows the coherent oscillations to grow for longer, and the larger the amplitude of the cavity field oscillations, the easier it becomes for the axion to "push" the cavity mode.
As anticipated before, QUAX can operate also in a different configuration that is implemented in the LNL laboratories. This consists in the employment of magnetized media to exploit the coupling of the axion to the electron spin, as first proposed in Ref. [45]. They stressed that aligned electron spins stimulate the axion photon conversion because having a spin density of $n_s \sim 10^{23}$ cm^{-3} would be equivalent to applying a 270 T magnetic field in a conventional haloscope. This idea was the backbone of the QUAX proposal [46] that is therefore a type of experiment sensitive to the coupling with electrons g_{aee} as we defined in Eq. (2.42).
This research activity is then divided between LNF with a conventional haloscope and LNL where magnetized media and a conventional haloscope are already employed. I will not discuss further about the experimental activity at LNL but it's worth our time to underline the results obtained in the last years. In particular it was carried out an upper limit on the coupling of DFSZ axions to electrons of $g_{aee} < 4.9 \cdot 10^{-10}$ GeV^{-1} for a mass $m_a = 58\mu$eV [47] and more recently an upper limit of $g_{a\gamma\gamma} < 0.766 \cdot 10^{-13}$ GeV^{-1} for a mass $m_a = 43\mu$eV reaching in this case the sensitivity necessary for the detection of galactic QCD axion [48]

3.2.2 Power emitted and Scan rate

We briefly discussed about the coupled oscillator model that gives us an idea of the role of the resonant cavity in the axion detection. This model however does not capture the effects of spatial coherence that will emerge now naturally from the treatment of the haloscope signal power. The equations of axion electrodynamics are derived from the Lagrangian in appendix A of Ref. [10] and in the same Ref. are also solved with boundary conditions appropriate to a haloscope detector. In this thesis I will only underline the key passages, the first of which is the inhomogeneous wave equation for the electric field in the presence of an axion source:

$$\nabla^2 \mathbf{E} - \partial_t^2 \mathbf{E} = -g_{a\gamma\gamma} B_0 \partial_t^2 a \hat{\mathbf{z}} \tag{3.52}$$

where the cavity walls define the boundary conditions. We already exploited in Section 3.1.1 that we have a complete set of orthogonal modes $\mathbf{e}_m$ for the electric and $\mathbf{h}_m$ for the magnetic field inside the cavity. If we use the orthogonality condition for the modes and integrate over the cavity volume our wave equation becomes:

$$(\omega_n^2 + \partial_t^2) E_n(t) = g_{a\gamma\gamma} B_0 \frac{k_n}{\lambda_n} \partial_t^2 a(t) \tag{3.53}$$

where λ_n is the arbitrary normalization for each mode, the subscript n comes from the orthogonality condition ($\mathbf{E}$ can be written in terms of the orthogonal basis) and k_n includes within itself the integration, it is defined as:

$$k_n = \int d^3\mathbf{x} \hat{\mathbf{z}} \cdot \mathbf{e}_\mathbf{n}^*. \tag{3.54}$$

Eq.(3.53) is the equation of motion for a driven, undamped harmonic oscillator. The damping coefficient for a mode with resonant frequency ω_n and quality factor Q_n is its linewidth ω_n/Q_n so a term of the form $(\omega_n/Q_n)\partial_t E$ that takes into account losses of the system can be added to our equation. Togheter with this new piece, Eq.(3.53) is carried to the Fourier domain and this lead us to the amplitude of the Fourier component at ω that is just:

$$E_n(\omega) = g_{a\gamma\gamma} B_0 \frac{k_n}{\lambda_n} \frac{\omega^2 a(\omega)}{\omega_n^2 - \omega^2 - i\omega\omega_n/Q_n} \tag{3.55}$$

which can be compared to Eq.(3.51) to note that we found again the scaling with $g_{a\gamma\gamma}$, B_0 and a.
To simplify the dependence on parameters of the cavity mode, it is easiest to proceed directly to evaluating the total steady-state **electromagnetic energy stored** in the cavity mode:

$$U_n = \lambda_n \int_{-\infty}^{+\infty} \frac{d\omega}{2\pi} |E(\omega)|^2 = g_{a\gamma\gamma}^2 B_0^2 \frac{k_n^2}{\lambda_n} \int_{-\infty}^{+\infty} \frac{d\omega}{2\pi} \frac{\omega^4 |a(\omega)|^2}{(\omega^2 - \omega_n^2)^2 + \omega^2\omega_n^2/Q_n^2}. \tag{3.56}$$

Now it is time to do some approximation, $|a(\omega)|^2$ is sharply peaked near the cavity resonance: in particular we have that $\omega_{max} \approx m_a = \omega_n - \delta\omega_a$ where the detuning $\delta\omega_a$ is $\sim \mathcal{O}(\omega_n/Q_n)$ and $Q_a \gg Q_n \gg 1$. All this means that the coefficient of $|a(\omega)|^2$ is approximately constant over the range of frequencies that contributes appreciably to the integral. Moreover with a high Q cavity, we can expand to lowest nonvanishing order in the small quantity $\delta\omega_a/\omega_n$ and we can also write the ramaining term of $|a(\omega)|^2$ inside the integral in terms of m_a and ρ_a. What we get the for the energy stored is:

$$U_n = g_{a\gamma\gamma}^2 B_0^2 \frac{k_n^2}{\lambda_n} \frac{Q_n^2}{1 + (2Q_n\delta\omega_a/\omega_n)^2} \frac{\rho_a}{m_a^2}. \tag{3.57}$$

It is now time to define another very important quantity, remembering all our discussion in Section 3.1.1 for a cylindrical cavity we have the three indices n, m, ℓ, so let's introduce the **form factor**:

$$\mathcal{C}_{nm\ell} = \frac{k_{nm\ell}^2}{V\lambda_{nm\ell}} = \frac{(\int d^3\mathbf{x}\hat{\mathbf{z}} \cdot \mathbf{e}^*_{nm\ell}(\mathbf{x}))^2}{V \int d^3\mathbf{x}\epsilon(x)|\mathbf{e}_{nm\ell}(\mathbf{x})|^2} \tag{3.58}$$

where V is the cavity volume and $\epsilon(x)$ is the permettivity. It is easy to see that $\mathcal{C}_{nm\ell} < 1$ and physically this quantity parameterizes the overlap between the cavity mode and the external magnetic field, that is a dependence that comes directly from the interacting lagrangian of Eq. (2.39).
Following our discussion of Section 3.1.1, an empty cylindrical cavity generally has both TE and TM modes and clearly, by definition, $\mathcal{C}_{nm\ell}$ will vanish identically for any TE mode so we can restrict our attention only to the TM ones. Moreover, thanks to our homogeneous external field $B_0\hat{\mathbf{z}}$, spatial oscillations in the electric field profile lead to other cancellations in $\mathcal{C}_{nm\ell}$. For an empty cylindrical cavity infact, $\mathcal{C}_{nm\ell} \neq 0$ only for TM_{0m0} modes, furthermore it falls also rapidly with increasing mode index m. It is for all this reasons that our attention is restricted now only to the TM_{010} mode that is the one used in practice by most haloscope detectors.
Thanks to this discussion we can now concentrate only to one mode and drop the mode subscript on U, ω_n and Q_n. Our final result for the steady-state energy transferred to the cavity mode by axion field oscillations is then:

$$U = g_{a\gamma\gamma}^2 \frac{\rho_a}{m_a^2} B_0^2 V \mathcal{C}_{nm\ell} Q_L^2 \frac{1}{1 + (2Q_L\delta\omega_a/\omega_c)^2} \tag{3.59}$$

where is important to note the Q_L^2 dependence that we would have obtained from Eq.(3.51).
It all adds up with our qualitative discussion of the previous subsection but what we care really about is not the energy deposited in the mode, but how much power we are able to couple into our receiver chain. The total power dissipated in any electromagnetic resonator is given by:

$$P_{tot} = \omega_c \frac{U}{Q_L} \tag{3.60}$$

while the **signal power coupled to the receiver** is:

$$P_{sig} = \omega_c \frac{U}{Q_{ext}} = g_{a\gamma\gamma}^2 \frac{\rho_a}{m_a^2} \frac{k}{1+k} \omega_c B_0^2 V \mathcal{C}_{nm\ell} Q_L \frac{1}{1+(2Q_L \delta\omega_a/\omega_c)^2} \tag{3.61}$$

where we used the relationships between Q_L, Q_0 and Q_{ext} of Eqs. (3.29), (3.34) and (3.35). The last needed step is to put aside all the natural units because we need to make contact with the experiment, inserting the appropriate constants inside our last equation we get:

$$P_{sig} = \left(\frac{g_{a\gamma\gamma^2}}{m_a^2} \hbar^3 c^3 \rho_a\right) \left(\frac{k}{1+k} \omega_c \frac{1}{\mu_0} B_0^2 V \mathcal{C}_{nm\ell} Q_L\right) \left(\frac{1}{1+(2Q_L \delta\omega_a/\omega_c)^2}\right). \tag{3.62}$$

From this equation we can also appreciate the experimental role of the coupling parameter k. Our last expression is written in terms of Q_L that is more related to measured quantity than Q_0 that is fully determined by the geometry and material composition of the cavity so it remains fixed. Q_L and k are adjustable so it gives us the opportunity to find the optimal value, if we infact insert Eq. (3.35) in our expression for the signal power we can note that P_{sig} has a $k/(1+k)^2$ dependence. Then our signal is maximized for $k = 1$ that is a very specific configuration, in this case the cavity is said to be **critically coupled** to the receiver chain. In this peculiar case, half the signal power is dissipated by the resistance of the cavity walls and the other half is coupled into the receiver.
We have also an undercoupled ($k < 1$) case where Q_L and P_{sig} increase but most of the power is absorbed internally and an overcoupled ($k > 1$) case where most of the conversion power is measurable but Q_L decreases.
It all appears very straightforward but the critical coupled case is not the optimal haloscope operating point. This new experiment point of view comes along with one important request: m_a is unknown so the cavity resonance ν_c must be tunable.
In all haloscope experiments, the standard procedure is to sit at one frequency ν_c, measure the cavity noise for whatever integration time is required to attain the desired sensitivity, increment ν_c by $\delta\nu_c$ and repeat this process many times. The axion sensitive resonant mode of any microwave cavity can be tuned by using an automated mechanical system to adjust the position of internal conductors or dielectrics, this will be discussed in detail in section Section 3.3.1. In practice all the cavity parameters such as Q_L, k and $\mathcal{C}_{nm\ell}$ will vary throughout the tuning range but for the derivation of the scan rate it's assumed that only ν_c vary during the tuning process. Morevore it is also assumed that the tuning step size is some constant faction 1/F of the cavity linewidth ($\delta\nu_c = \Delta\nu_c/F$). All this discussion will enable us to determine an appropriate value for $\delta\nu_c$ and derive a useful approximate expression relating the haloscope **scan rate** $d\nu/dt$ to the coupling sensitivity $g_{a\gamma\gamma}$.
In this case I will not treat the discussion at all, presenting directly the expression of the scan rate used in the article of the first run of the QUAX experiment [9]. A

very exhaustive discussion of the scan rate derivation is given in Ref. [10] but a more general one is given in Ref. [49] where different cases are taken into account. Therefore the following expression can describe two different cases, the one with $Q_L \ll Q_a$ and the one with $Q_L \gg Q_a$:

$$\frac{d\nu}{dt} = g_{a\gamma\gamma}^4 \frac{\rho_a^2}{m_a^2} \frac{1}{SNR^2} \left(\frac{B_0^2 V C_{010}}{k_B T_{sys}} \right)^2 \frac{k^2}{(1+k)^2} Q_a min(Q_L, Q_a), \tag{3.63}$$

where the signal to noise ratio, SNR, , is defined as the ratio between the signal power and the uncertainty of the noise power SNR$= P_{sig}/\delta P_{noise}$, while T_{sys} is the system noise temperature, whose reduction is of fundamental importance in speeding up the scan rate of the experiment. We will return and discuss more in detail about this two parameters in the next subsection. As it can be immediately seen, this expression allows us to reconnect to the discussion we did about the enhancement of Q_L in the previous subsection: we can increase Q_L as we want but we will always have the experimental limit of Q_a that is of order 10^6. It doesn't make sense at all to use a resonant cavity with a quality factor greater than Q_a.
Eq. (3.63) is then the most useful figure of merit for the design of a haloscope detector. The most important thing here is that the scaling with Q_L (so with Q_0) is weaker that the one of Eq. (3.62): this suggests us to design a cavity to maximize $\mathcal{C}_{nml}^2 Q_0$ rather than $\mathcal{C}_{nml}^2 Q_0^2$. This makes sense because when we increase Q_L we enhance the signal power but also reduce the cavity linewidth, slowing the scan rate. The expression for the scan rate gives us also the optimal experimental configuration that has to be used in an haloscope detection. Once the cavity design is fixed, so Q_0, we can then determine the optimal value for k. From Eq. (3.62) it can be seen that we have a scaling of $k^2/(1+k)^3$ which is maximazed when $k = 2$. This will be the aim for our experimental setup, we will return to it later when dealing with the experiment details.
The scan rate gives us also another importan experimental hint, it furnish the required measurement time τ in order to reach the desired sensitivity $|g_{a\gamma\gamma}|$ at each step. In practice then, assuming some nominal values for the detector parameters, the target sensitivity is reached after **a time of integration** of about:

$$\tau = \delta\nu_c \left(\frac{d\nu}{dt} \right)^{-1} \tag{3.64}$$

therefore it is very important to chose the right tuning step, thanks to it we don't have to stick in one experimental point for an impractical experimental time. Nevertheless we have to remember that the tuning step depends from the bandwidth of the resonant mode of the cavity that in turn depends from Q_L. We will return to this later in this thesis work.

3.2.3 Coherent detection

We have introduced and discussed the two figures of merit in the axion search, they will play the fundamental role on the data analysis in order to put upper limits on the axion parameter space in the working range of the QUAX experiment.
Before starting to describe the details of the experiment it is needed to handle some numbers and to talk about the experimental challenges of this line of research. Let's start again from the power emitted of one possible axion event: using Eq. (3.62), plugging in some benchmark parameter values for a detector and considering a coupling $|g_{a\gamma\gamma}|$ arising from the model band, it can be obtained a power that is of

order $P_{sig} \sim 10^{-24}$ W. A value given at random is meaningless if it is not compared to a real experimental case. We will get a better sense of just how small P_{sig} is when we compare it to the noise power in any real haloscope.
To understand the noise limiting the sensitivity of a haloscope search, it is important to appreciate that the haloscope signal is itself a noise signal in any measurement of duration $\tau > \tau_a$. The conversion power will be distributed over a finite bandwidth and then if we happen to be looking around the right frequency, the presence of axions will manifest in incoherent fluctuations of the cavity's electric field which are in principle indistinguishable from other contributions to the total noise in the same bandwidth.
The main contribution to the total noise that we must take into account is the **Johnson (thermal) noise** [50] associated with the resistance of the cavity walls. In Ref. [51] is showed that the voltage noise on an antenna receiving blackbody radiation is completely equivalent to the Johnson noise of a matched load at the same temperature. Therefore we can think of Johnson noise as arising from a blackbody photon gas inside the cavity, in thermal equilibrium with the walls. For our description we will write then the total noise power in any bandwidth Δ_ν in the form:

$$P_N = k_B T_{sys} \Delta\nu \tag{3.65}$$

where the system noise temperature T_{sys} is not necessarily equal to the physical temperature T of the haloscope. Now we can put some numbers in, let's consider a room temperature system ($T_{sys} \sim 300$ K) and a bandwidth equal to $\Delta\nu_a = \tau_a^{-1}$: this provides us a noise power $P_N \sim 10^{-17}$ W that is larger than the P_{sig} of before by a huge factor of 10^6. This is a lot but luckily **cryogenic temperatures** come to help: a dilution refrigerator can be used to reach a physical temperature of $T \sim 30$ mK but also in this case we will have a ratio of about $P_{sig}/P_N \sim 10^{-3}$. This is less than before but not yet the arrival point; in any case we have demonstrated one of the key motivation to bring the whole system to cryogenic temperatures.
Becoming aware of the main source of noise of the system, the real figure of merit of an haloscope shouldn't be the signal power alone but instead:

$$R = \frac{P_{sig}}{\delta P_N} \tag{3.66}$$

where δP_N is the uncertainty in our estimate of the total noise power and R is the signal to noise ratio (SNR) that we anticipated in Eq. (3.63). To develop the discussion further, we need a specific expression for δP_N in an axion haloscope which in turn depends on how we intend to couple our microwave cavity: to a coherent or incoherent receiver.
The main distinction from the two approaches relies on whether the first element to amplify the input signal and protect the SNR from further degradation is linear or nonlinear, as can be observed by treating both regimes in a unified formalism [52]. The defining feature of a coherent or linear receiver infact, is that its output is a linear function of the electric field at the receiver input. Thus a **coherent receiver** has intrinsic spectral resolution: the Fourier component of the input signal at frequency ω will show up at the same frequency in the output signal. On the contrary, in an **incoherent or bolometric receiver**, the output is proportional to the average intensity and thus does not preserve the phase information in the input signal. But what to keep in mind when chosing between the two principles? Our whole discussion applies to detectors of electromagnetic radiation at any frequency, but in the practical world technological limitations conspire to favor coherent detection at low frequencies ($\nu < 1$ THz) and bolometric detection at high frequencies ($\nu > 1$

THz). This because the electronic response of common materials is too slow to implement a linear amplifier in the optical frequencies, while at microwave frequencies the small energies of individual photons make bolometric detection, such as single photon detection, demanding.
The working frequencies of the QUAX experiment are the microwave ones so we restrict our attention to the coherent receiver case. What it's done in practice is a pairing of our microwave cavity to a coherent receiver by inserting a small antenna through a port in one of the endcaps. What happens then is that the motion of electrons in the antenna transduces the cavity's fluctuating electric field E_z into a fluctuating voltage at the receiver input. At this point all the key passagges of an haloscope search are done: the signal is amplified by the receiver chain, digitized at room temperature, processed using a discrete Fourier transform and analyzed in the frequency domain as a power spectrum.
To understand the sensitivity of the haloscope search, it is sufficient to consider the statistics of the noise voltage at the receiver input, where we evaluated the signal power in Eq. (3.62).
Let's finally write the relation that describes the uncertainty in the (effective) Johnson noise power in any bandwidth Δ_ν, I report only the final expression but for a detailed discussion refer to [10]:

$$\delta P_N = \frac{k_B T_{sys} \Delta\nu}{\sqrt{\Delta\nu\tau}}. \tag{3.67}$$

Thanks to this equation it's immediate to see that the optimal bandwidth for a haloscope search is $\Delta\nu_c \approx \Delta\nu_a$. $\Delta\nu_c > \Delta\nu_a$ will lead us to add more noise without appreciably increasing the signal power while we can't capture the whole signal if we have $\Delta\nu_c < \Delta\nu_a$. Thus using this optimal configuration and considering the signal to noise ratio we obtain the **Dicke radiometer equation**:

$$R = \frac{P_{sig}}{k_B T_{sys}} \sqrt{\frac{\tau}{\Delta\nu_a}}. \tag{3.68}$$

Assuming T_{sys} known, this equation gives us an estimate of the time τ required to detect or exclude axion conversion power P_{sig}. As usual, the signal to noise ratio, is the key fundamental quantity to estimate the sensitivity of a search with a given set of experimental parameters: also in this case it is demanded a value of $R = 5$ for both a discovery or an exclusion in the parameter space.

3.3 Experimental setup

This section is dedicated to the set up of all the instrumentation that served in the first run of the QUAX experiment. First of all it's advantageous to show a global picture of the whole experimental structure as in Fig. 3.12 and its corresponding graphic diagram that serves as schematic summary like in Fig. 3.13. After providing a general overview of the setup, a more accurate description of all the constituent parts will be presented. Thanks to this we will have all the tools to treat the whole experimental run in the next chapter.

In Fig. 3.12, can be seen all the constituent parts of the experiment that will be explored further in the next subsections. The main actor is the **microwave resonant cavity** which is located under the cryostat. All the radiofrequency electronics starts from this region and reaches up to the rack, which on the lower floor has the down conversion part with low frequency electronics in order to acquire data with a low

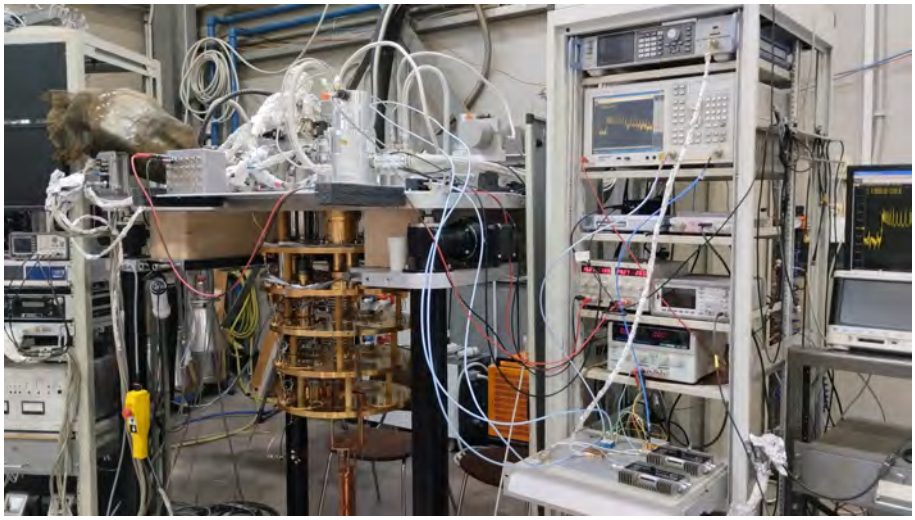

Figure 3.12. [53] A general view of all the experimental setup including the cryostat, the radio frequency and low frequency electronics, the data acquisition part and the rack.

sampling rate ADC. Above this part, we have all the other instruments that provide us radiofrequency signals such as an RF signal generator, or that allow us to measure the scattering parameters of the cavity such as the vector network analyzer (VNA), or simple DC signal generators. Before describing the details of all this specific areas of the experiment, let's talk about Fig. 3.13. This is a **schematic of the RF setup** of the experiment. The isothermal lines corresponds to different plates of the diluition refrigerator. We have three input lines available (L1, L2, L3) that togheter with the output L5 line serve to calibrate the whole system, I will return to this procedure in the next chapter when I will cover all the key passages of the calibration procedure. We have 3 room temperature switches (RT1, RT2, RT3) and one cryogenic, CR7, that serves us to send and receive the signal with the VNA each time in different lines combinations. This is the key passage in order to achieve the goal to measure all the scattering parameters of the cavity. The L5 line is designated as the output line because it includes two amplifiers in it: the HEMT and FET that are, respectively, the cryogenic and room-temperature amplifiers that begin our amplification chain in order to measure the haloscope noise. Two circulators (C1, C2) are also inserted in the RF lines, their role is to force a directionality of the input signal and they act as isolators avoiding reflections. In the L5 line is also indicated a superconductive RF cable in yellow which limits losses, and a power splitter indicated with S1 that serves us to carry out both calibration procedures and subsequent noise data acquisition. The three input lines have intrinsically 15 dB each of attenuation of the signal but L3 have two more attenuators of 20 dB each. The end of L5, after the splitter, arrives to the down conversion part; here it is not fully specified but is schematized as a whole area, I will return to it in the next pages.

3.3.1 Cavity and mechanical rod

As previously emphasized, the microwave cavity represents the core component of an haloscope. In this run of the QUAX experiment is used a cylindrical oxygen free high thermal conductivity (OFHC) copper resonant cavity, with inner radius $r = 13.51$ mm and height $h = 246$ mm, for a total volume $V = 0.141$ l [9]. The

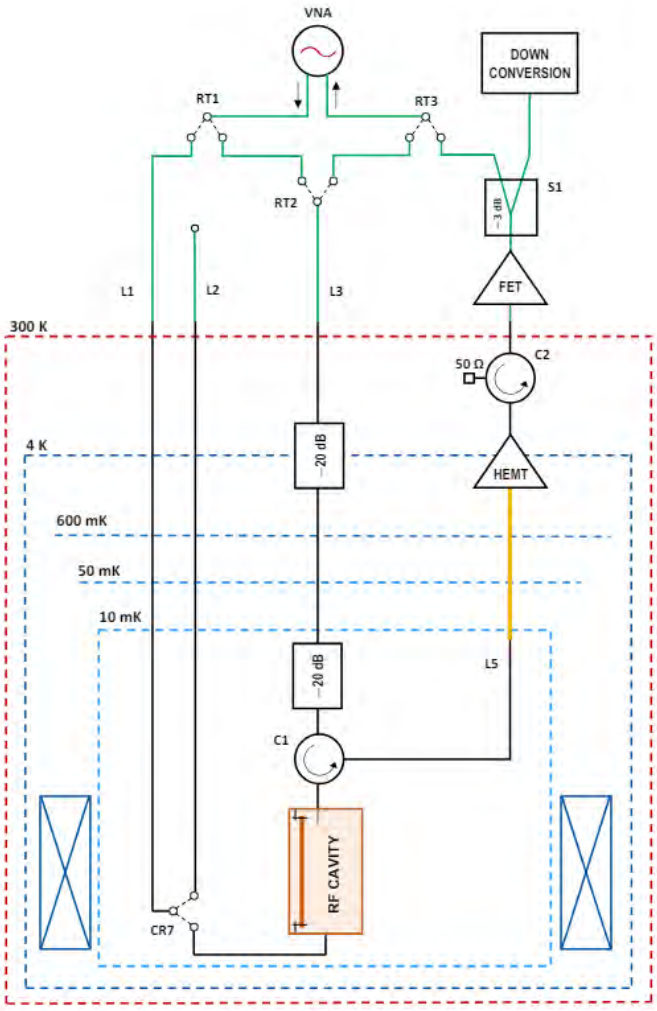

Figure 3.13. [53] Experimental setup sketch with the temperature stages of the dilution refrigerator and with the consituents of all the RF lines. L1 and L3 are input RF lines, L5 is the output amplified line and L2 is an auxiliary line used for further checks. Room temperature switches (RT1, RT2, RT3), cryogenic switch (CR7), attenuators indicated with their attenuation values and the two circulators (C1, C2) are also shown. A superconductive RF cable in L5 is indicated in yellow while the magnet, thermalized in the 4 K vessel, is shown as two crossed squares. The HEMT and FET are the two radio frequency amplifiers mounted on L5 that, through the power splitter indicated as S1, bring the output signal to the down conversion part.

body is divided into two semicylinders, including the endcaps, sealed together with screws. In Fig. 3.14 are visible the two sections of the cylindrical cavity, with the **mechanical rod** that served to shift the resonant frequency of the modes. In addition to the terminations for the rod, are present also the holes for the dipole antennas: through them the cavity is coupled with two coaxial cables. One antenna is fixed and weakly coupled, with coupling estimated from simulations $1.4 \cdot 10^{-3}$ and verified to be less than $7 \cdot 10^{-3}$ from calibration data (we will return to this point in the next chapter), such that Eq. (3.62) and Eq. (3.63) are still valid. The other is obtained by stripping the end of a coax cable, leaving only the central conductor

for a 2 mm length as shown in the right image of Fig. 3.16. In the left image of Fig. 3.16 the structure that serves to maintain the two stepper motor is shown. The coax cable is connected to a linear motor, that is in grey in the background, whose movement allows the tunability of the coupling. The linear motor is the **attocube ANPz111** [54], a nanopositioner for vertical motion, it works also at cryogenic temperatures and as a piezoelectric motor allows us to insert the coaxial cable inside the cavity by feeding it with voltages from specifications. Inside the structure for the two motors there is a rotative stepper piezoelectric motor from Attocube Systems, the model **ANR240** [55]. As anticipated before, the frequency tuning is obtained by moving a copper rod with radius 1.5 mm and length 244 mm inside the cavity volume that is in turn reduced to an effective volume of $V = 0.139$ l. The rod is supported by PEEK nails, which are centered off-axis with respect to the rod, one of this is clearly visible in the right image of Fig. 3.15 where a zoom of the cavity wall is shown; here it can be seen the copper rod together with the PEEK and the hole to insert the dipole antennas. At one end, the PEEK is grabbed by a copper mandrel, which is rotated by the stepper motor, as in Fig. 3.16. Thanks to this movement, the rod accomplishes an arc of circumference approaching the center of the cavity.
All the electromagnetic behavior of this system was simulated with the ANSYS HFSS suite [56] by Ing. Simone Tocci, this includes in order: the simulation of the modes of the empty cavity, their modification with the copper rod inside and lastly their shift due to its rotation. The resonant mode of interest, TM010, has a starting frequency of 8.817 GHz when the (ideal) rod is at rest in contact with the cavity wall. Moving the rod towards the center, the mode is squeezed and simulations indicate that the frequency is tuned up to 9.106 GHz with a rotation of 80 degrees, while keeping the geometric factor C_{010} close to its ideal value and with a reduction of the quality factor of about 10%.
Although the intrinsic quality factor of the cavity without the tuner is measured to be $Q_0 \simeq 10^5$ at cryogenic temperatures, the PEEK supporting the rod and the nonideality of the rod itself caused field losses, reducing the quality factor to about 50000. Also the coupling, that we wanted to be equal to $k = 2$ for the optimal value of the scan rate, resulted to be $k = 0.5$ after a more accurate analysis of calibration data. I will return to this point in the next chapter where I will analyze in detail all the calibration procedure; it is still useful though to show at this point the effect of the rotative motor to the whole system.

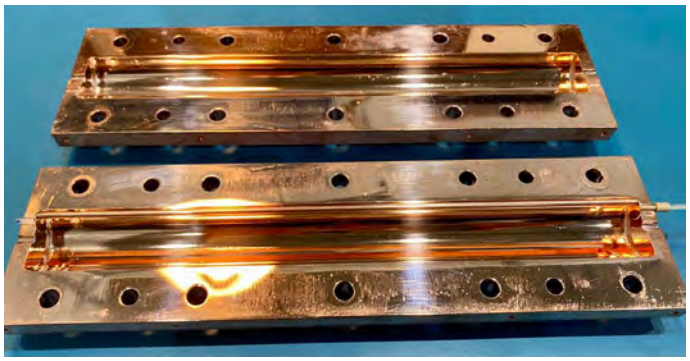

Figure 3.14. [53] The two sections of the cilindrical cavity, with the mechanical rod and the holes for the dipole antennas. The mechanical rod is present in the cilindrical section in the foreground, it can be noted because it is connected with the PEEK which comes out of the base of the cylindrical cavity.

In Fig. 3.17 the transmission coefficient of Eq. (3.49) relative to the TM_{010} mode is shown, this photo is taken from the VNA during a test of the cavity at room temperature with the measuring apparatus as in Fig. 3.18. In the latter figure are present the VNA, the whole cavity, one coaxial cable for the fixed antenna and a movable antenna without the stepper motor, just to test in a simple way the resonant mode of the cavity. Returning to the former figure, with a marker provided by the VNA, the resonant frequency of the TM_{010} mode is shown with its bandwidth and the calculated load quality factor Q_L. The bandwidth is defined as the two points around the peak where the power of the VNA is reduced of about 3 dB with respect to the central frequency, from this quantity the VNA calculates immediately the loaded quality factor; the intrinsic quality factor Q_0 is instead extracted from the fit procedure illustrated in the next chapter.
In Fig. 3.19 a test regarding the effect of the movement of the rod in the cavity is shown: four screenshot of all the first TM and TE modes of our cavity are illustrated. Starting from the upper left, the mode of our interest, TM_{010}, is the very first mode from the left side. The starting frequency on the screen is 8.7 GHz, the stopping is 9.5 GHz so the division is of 80 MHz each block. Moving the copper rod starting from the wall of the cavity to its center, all the mods shift from a lower frequency to a higher one; this can be seen in Fig. 3.19 starting from the upper left and going in order to upper right, lower left and lower right.

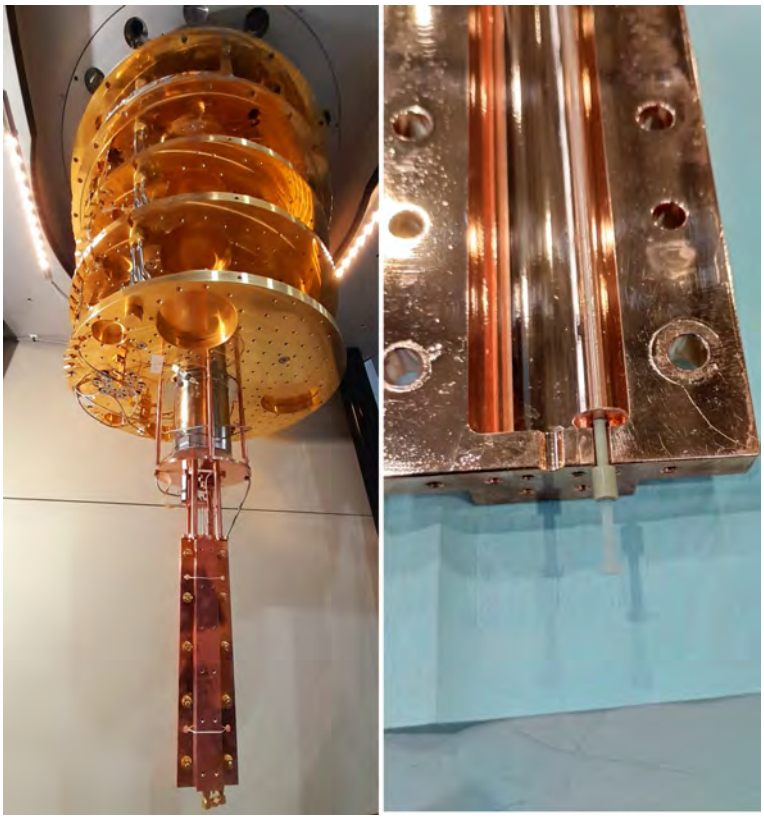

Figure 3.15. [53] In the left image a general view of the cavity mounted in the cryostat while on the right image a zoom on the cavity wall: in it, it can be seen more closely the copper rod together with the PEEK and the hole to insert the dipole antennas.

In the first graph of Fig. 3.20 the frequency of the TM_{010} is plotted vs the movement in degrees of the ANR240. All the points are the experimental frequencies

in which all the first QUAX run took place. Because of the bandwidth of the transmission mode we chose a step of 260 kHz for each point, this obviously depends on the loaded quality factor that from measurements resulted to be of around 32000. The starting frequency of the QUAX axion search is of 8.831516 GHz while the stopping frequency is of 8.837765 GHz, corresponding respectively to an arc of circumference of initial angle 2.95° and final angle of 13.17° for the tuning rod starting from the cavity wall as a reference. We have 24 experimental points, each of them spaced by a step of about 260 kHz, implying a 6.25 MHz span.
The second plot in Fig. 3.20 is about the sensitivity of the tuning procedure. The data points are the same as in the previous plot; however, in this case, the y axis shows the ratio between the frequency difference and the angle difference at each step. The points follow a linear distribution, meaning that the sensitivity of the tuning increases as the rod approaches the center of the cavity. As described before the frequency step is always the same because is fixed by our choice so since the sensitivity increases, it means that the step in degrees decreases. In fact, as the circumferential angles increased, the necessary step of the motor was always shorter to make every time the same step in frequency.

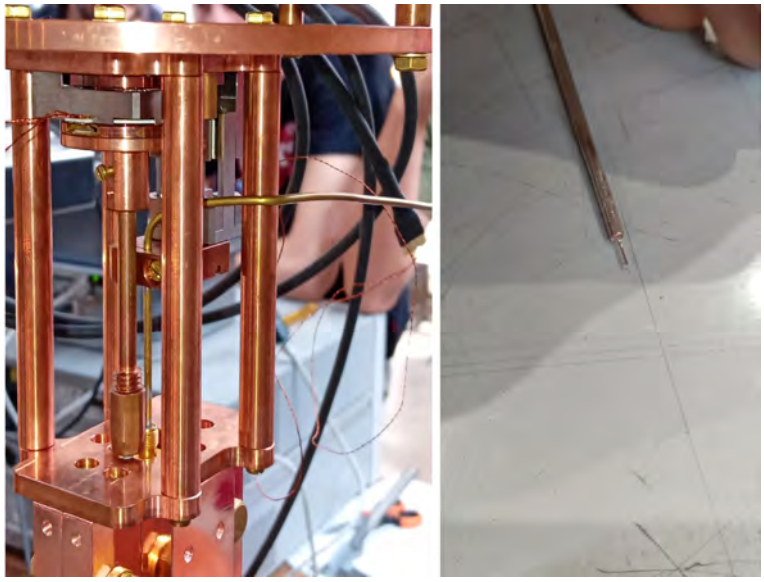

Figure 3.16. [53] In the left image the structure that maintains the two stepper motor is shown. The linear motor is the one in grey in the background that is connected to a coax cable, while the rotative one is connected to a copper mandrel that grabs the PEEK of the copper rod. In the right image the coax cable that is used as the movable antenna is instead shown.

3.3.2 RF electronics and cryostat

In this subsection we will deal the **radiofrequency setup** of the experiment contained in the cryostat. There are two main reasons why we need to go to cryogenic temperatures. The first relies on the two figure of merit of an haloscope, Eq. (3.62) and Eq. (3.63), as we said the larger is Q_L the better is the detection capability of an haloscope. The intrinsic quality factor Q_0, although determined by the cavity geometry, increases significantly at cryogenic temperatures, which is why superconducting materials are used.

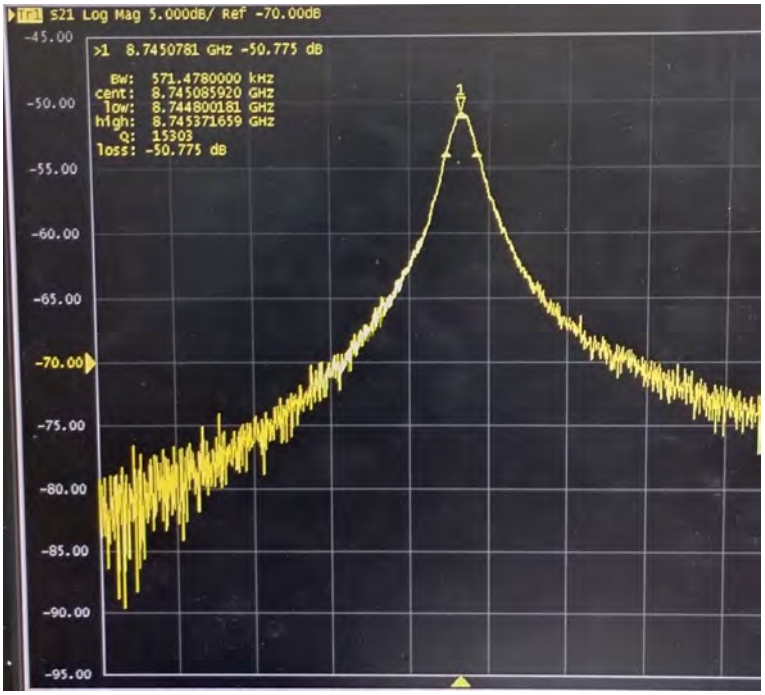

Figure 3.17. [53] Close look to the transmission coefficient of the TM_{010} mode. The VNA, through the 3 dB method, permits us to measure directly the loaded quality factor Q_L too.

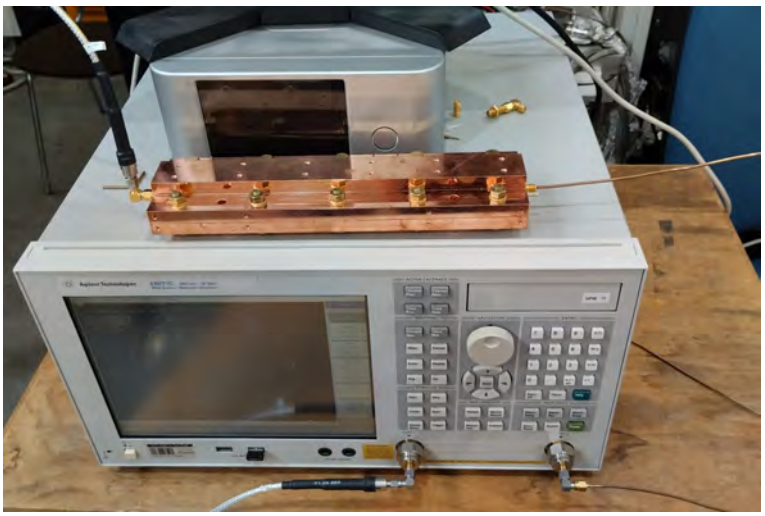

Figure 3.18. [53] Measurement apparatus that leads to the transmission coefficient shown in Fig. 3.17, the VNA provides the RF input and it allows us to directly measure the output signal coming from the resonant cavity.

The second reason is the fact that as we go down in temperature the noise is reduced, as Eq. (3.65) tells us about. Due to this motivation most of the setup is hosted in a Leiden Cryogenics CF-CS110-1000 **dilution refrigerator** equipped with two Sumitomo pulse tubes with cooling power of 1.5 W at 4 K each, all the main parts of the refrigerator as the mixing chamber (MC), the still and the heat exchangers

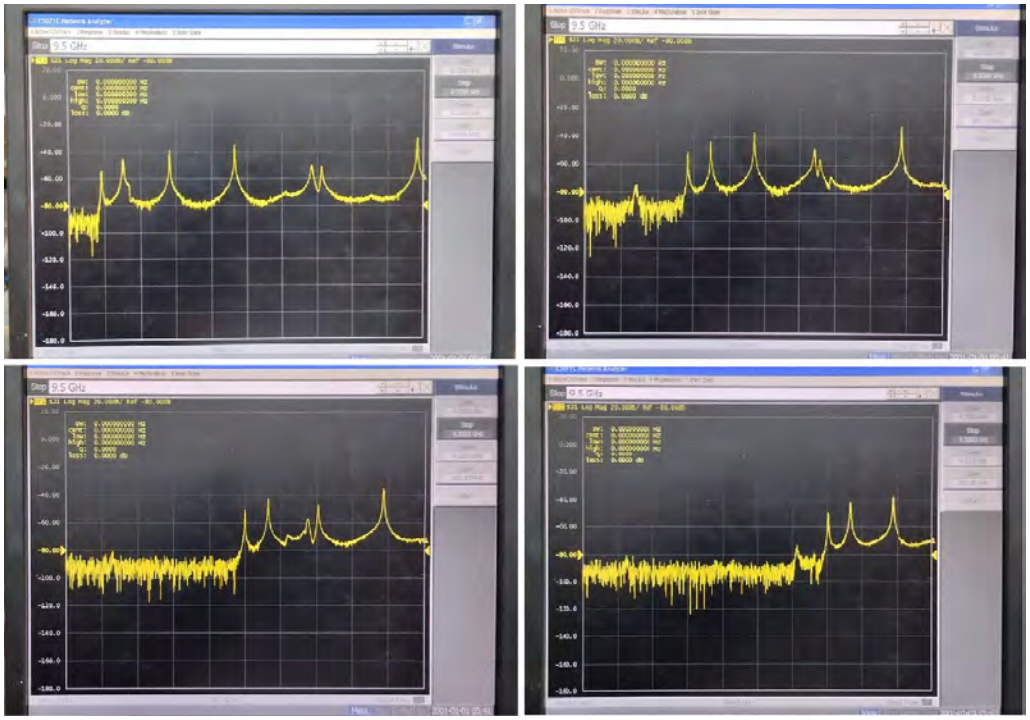

Figure 3.19. [53] In this four figures are present the first TM and TE modes of the cavity. Starting from the upper left and going to the lower right, it can be seen the effect of the movement of the copper rod that shifts the frequencies of all the modes.

are indicated in detail in Fig. 3.21, including the thermalization plates with their temperatures during regular operation.
The LNF haloscope employs a dry dilution refrigerator, whose operation relies on a ^{3}He-^{4}He mixture: the workflow starts from the MC that contains the pure ^{3}He phase on top of the dilute phase of ^{4}He contaminated with 6.6% of ^{3}He. The dilute phase in the mixing chamber is connected with an upward pipe to the still that is partially filled with liquid ^{3}He and mainly vapor ^{3}He, which is removed by vacuum pumps. This causes a gradient in the ^{3}He concentration in the dilute phase of the MC so to maintain an equilibrium, the pure ^{3}He in the mixing chamber crosses the phase boundary in a diffusive motion downwards the dilute phase. The whole process is endothermic, thus subtracting heat from the external environment, allowing to cool the whole system [57].
In the practice, as a precooling operation we use liquid Nitrogen, that flows in the LN pipes in thermal contact with each plate indicated in figure, to bring the temperature from 300 K to 77 K. Then, a pulse tube, which operates compression and decompression cycles to the ^{4}He gas, is switched on and brings the temperature down to about 4 K. Finally, circulation of the ^{3}He-^{4}He mixture is activated and the system is cooled down to about 10 mK in the coldest plate where the mixing chamber is thermally anchored. The MC is a stainless steel cylindrical container closed with a copper cap on the bottom side, with a diameter of about 120 mm. The still plate is usually at about 0.8 K, and this is an optimal temperature for the operation of our refrigerator. In fact, due to the parasitic heat input on the 0.8 K plate, the still does not need to be heated, although being provided with an internal heater. The 4 K plate is instead stabilized at this temperature thanks to the contact with the pulse tube.

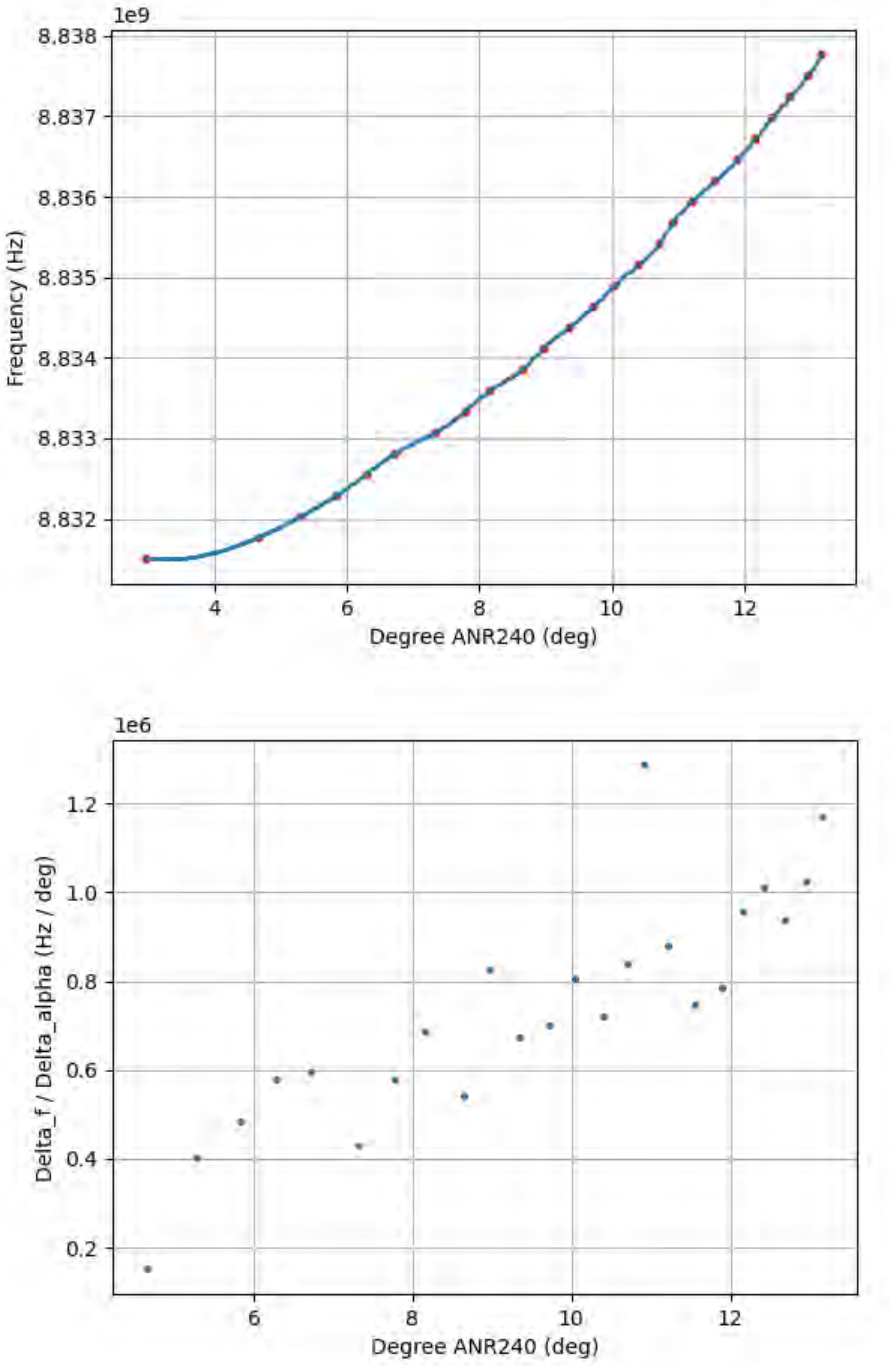

Figure 3.20. [53] In the upper figure the frequencies of the TM_{010} mode of our interest are plotted vs the movement in degree of the rotative stepper motor. In the lower figure the sensitivity of the rotative motor is instead plotted. In this case it is in fact shown on the y axis the ratio of the frequency and angle difference at each step.

The refrigerator is then segmented into different temperature stages constantly monitored by a series of thermometers: a platinum resistive one in the 50 K plate while on all the other plates ruthenium oxide (RuO2) thermometers are mounted.

The magnet and the HEMT are thermalized at the 4 K stage, while the cavity is connected to the last temperature stage which attained 20 mK at equilibrium. The cavity temperature, monitored during the data taking, reached about 30 mK [9].
A **NbTi magnet** was installed inside the cryostat [58], its dimensions are 486 mm height and 100 mm of cold bore diameter. The maximum current in the coils is of about 90 A, supplying energy for a 9 T magnetic field at the magnetic center. As said the magnet is anchored to the 4 K radiation shield, thus thermalized at the pulse tube temperature; his coils are made of NbTi, therefore being superconductive at 4 K.
At the start of the run the magnet initially operated at the nominal field of 9 T, but it was set to a lower safety value following a quench during a current ramp. The experiment here described was then conducted at 8 T, with a field inside the cavity volume of r.m.s $\sqrt{\langle B_0^2 \rangle} = 6.73$ T.

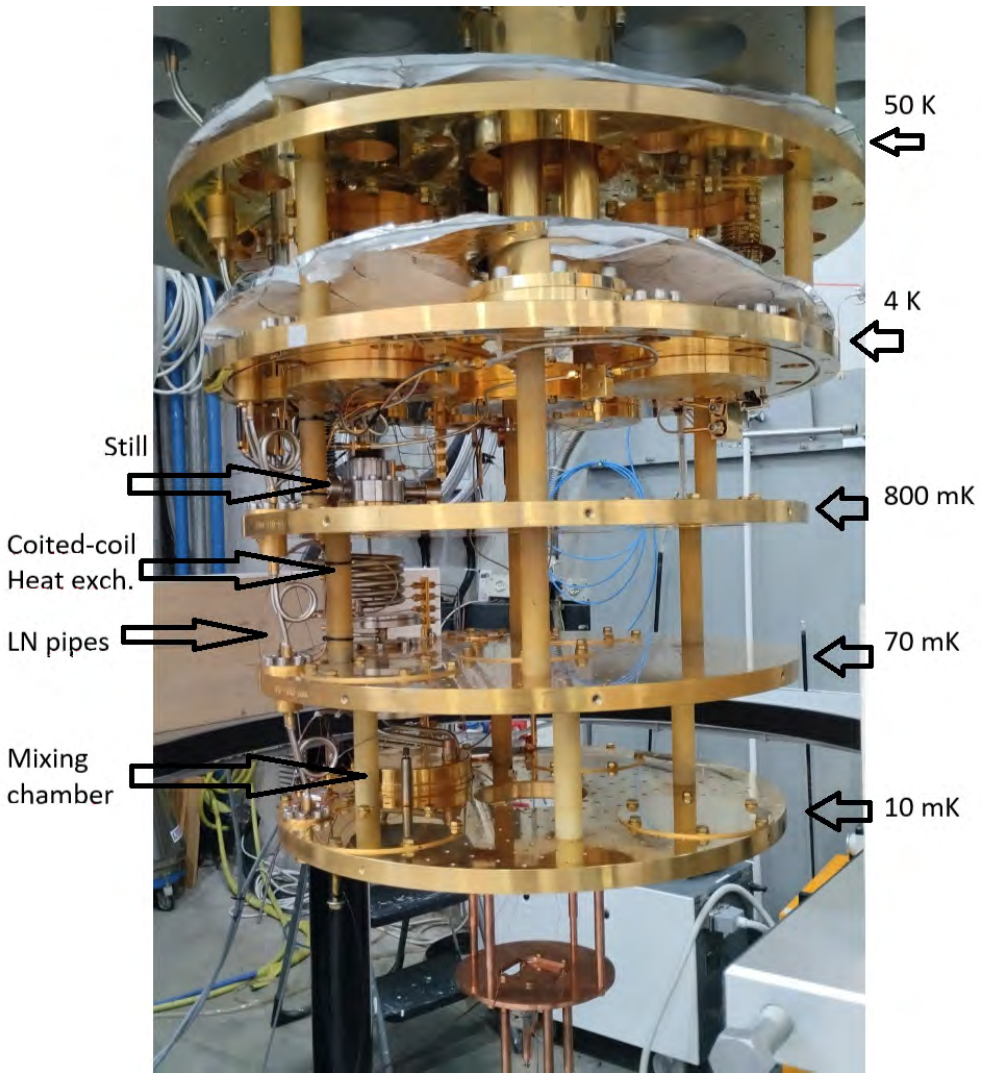

Figure 3.21. [53] Detail of the Leiden Cryogenics CF-CS110-1000 dilution refrigerator, showing the plate temperatures of all the thermalization stages. The main parts where the dilution process happens are also indicated: the mixing chamber, the still and heat exchanger.

For testing samples with microwave radiation, the cryostat is provided with four high-attenuating rf lines, from 300 K to the 10 mK stage, used as inputs, and one low-attenuation rf line used as output. The rf wires are coaxial cables made of BeCu-Ag-CuNi with SMA connectors endlines and are thermalized in each plate of the fridge. In the rf lines used as inputs power attenuators are mounted along the wires to reduce the amount of thermal power coming from the 300 K environment. Concerning the one output line instead, it's equipped with two linear amplifiers in the radiofrequency regime. The two commercially available microwave amplifiers are a **cryogenic HEMT** and a **room-temperature FET**, and are both field-effect transistor amplifiers: they are shown in the Fig. 3.22 below.

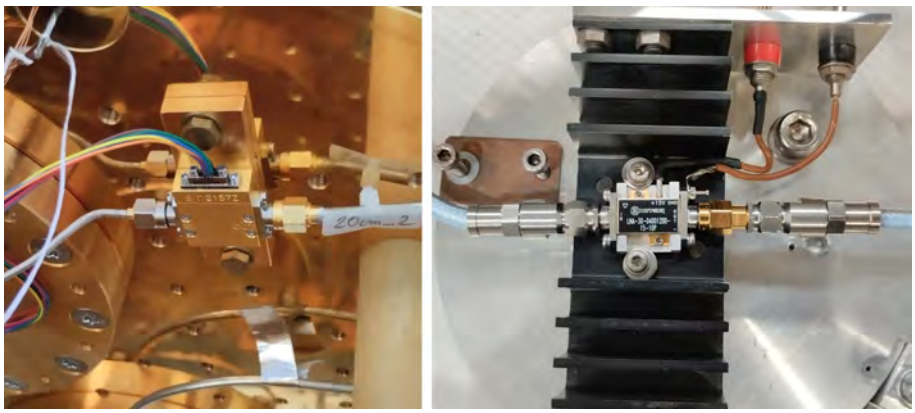

Figure 3.22. [53] At left the cryogenic HEMT amplifier attached to the 4 K plate. At right the Room temperature FET amplifier, mounted on a radiator.

The HEMT is a model LNF-LNC6_20C s/n 1403Z from Low Noise Factory and is installed on the 4 K plate. Its main features are gain, compression point, and noise temperature, which have been tested to verify the nominal values given in the datasheet [59].
The HEMT gain results in 30 dB over a large bandwidth, between 4 and 12 GHz, consistent with the nominal value. The 1 dB compression point defines the saturation of the amplifier, and is defined as the input power value at which the gain is decreased by 1 dB with respect to the linear regime, where the gain is constant: as a reference, it is approximately -27.5 dBm at 10 GHz. The measured noise temperature instead differs a bit from the nominal value of about 3 K added noise, given at 10 GHz when the temperature is 4 K. An added noise temperature of about $T_n^{HEMT} \approx 4.7$ K was estimated.
The FET is a model LNA-30-08001200-09-10P from Narda-Miteq and is put at 300 K on the outside of the cryostat. The gain has been verified only between 8 and 12 GHz, resulting in 30 dB. The 1 dB compression point at 10 GHz has been found to be about -16.5 dBm [60].
The tests are also repeated with the two amplifiers in series. The various contributions to T_{sys} were introduced in Section 3.2.3. For any haloscope at physical temperature T coupled to a coherent receiver, the most general expression for the **system noise temperature** is:

$$k_B T_{sys} = h\nu N_{sys} = h\nu\left(\frac{1}{e^{h\nu/k_B T}-1} + \frac{1}{2} + N_A\right). \tag{3.69}$$

The first additive term on the RHS represents the actual thermal noise, which we see is proportional to the average number of blackbody photons inside the cavity

at physical temperature T. The second term is quantum noise associated with the zero-point fluctuations of the blackbody gas while the added noise N_A encompasses the total **input-referred noise** originating in the receiver itself.
What does this last term consist of? We said that the crucial element which defines a coherent receiver is a linear amplifier whose output is just the input signal multiplied by some gain G $\gg 1$. The energy required to achieve this amplification has to come from somewhere: Any device capable of amplifying a signal can also couple noise into the output signal through whatever channel serves as the 'power line' [10].
By definition, the added noise of any amplifier is not already physically present in the input signal. Therefore, what is done in practice is to define the input-referred added noise N_A as the physical added noise divided by the gain G. In this sense, the input-referred added noise is just the additional noise that would have to be present at the input of an ideal noiseless amplifier with gain G to reproduce the noise we actually observe at the real amplifier's output. This definition is convenient because it allows us to define the input-referred added noise of the entire receiver chain in an analogous way. It is easy to see that if the receiver chain includes several linear amplifiers with gain G_i and added noise N_{Ai} in series, the net input-referred added noise of the receiver chain will be:

$$N_A = N_{A1} + \frac{1}{G_1} N_{A2} + \frac{1}{G_1 G_2} N_{A3} + ... \tag{3.70}$$

Therefore this is the key feature of an amplifier chain: the noise performance of the first amplifier (or preamplifier) determines the added noise of the whole receiver chain, provided it has sufficiently high gain G_1.
In this sense our preamplifier is the HEMT that has an high gain and is thermalized at 4 K. Plugging in numbers we see that in our configuration, the noise temperature of the FET amplifier (with nominal value of about 66 K) does not contribute significantly to the total noise temperature of the receiver chain. In fact, referring it to the HEMT input, the contribution should be $T_n^{FET} = 66$ K/1000 = 66 mK, where 1000 is the HEMT gain in linear units, thus being small compared to the HEMT noise [58].
The HEMT and FET amplifiers are then put in series on an rf line used exclusively as readout line; since the four original lines are very lossy, this is a fifth custom one. To minimize loss contributions, the fifth rf line pieces between the 10 mK stage and the still plate are constituted of NbTi-PTFE-NbTi coaxial cables, which remain superconducting under about 10 K. After this special part, the line is formed, in order, by a normal metal cable from the latter to the 4 K stage, the HEMT, a normal metal cable for the remaining route from 4 K to 300 K, a commercial room-temperature cable to the FET and lastly another commercial room-temperature cable from the FET to the low frequency part we are going to deal in the next section.

3.3.3 Low frequency setup and DAQ

This third section is dedicated to the final part of the experimental setup, namely the elements situated outside the cryostat, following the FET stage.
We refer then to all the instrumentations that are placed at 300 K in Fig. 3.13. In this figure are evident the VNA, the three room temperature switches, the splitter S1 and the box that represents the down conversion part: in what follows we are going to talk more explicitly about all of them.
In this sense, a specific zoom on the rack as Fig. 3.23 serves as a reference for what we lack to describe. In it the various instruments that are useful for measuring or

for allowing other instruments to work are shown, together with this latter ones. As we previously anticipated, the **VNA** measures scattering parameters S_{ij} of a two-port network by reading the reflected or transmitted wave from the network with respect to the incident wave. This is an Agilent E5071C from 300 kHz to 20 GHz and has two ports.
The signal generator is a Rohde&Schwarz SMA100B from 8 kHz to 20 GHz, with one channel available. We use it as a source oscillator in continuous wave mode for the Mixer that is the main actor of the down conversion part. The DC generators are necessary to put in action the three room temperature switches and the cryogenic switch that all together allow all the combinations required for measurements and calibrations.

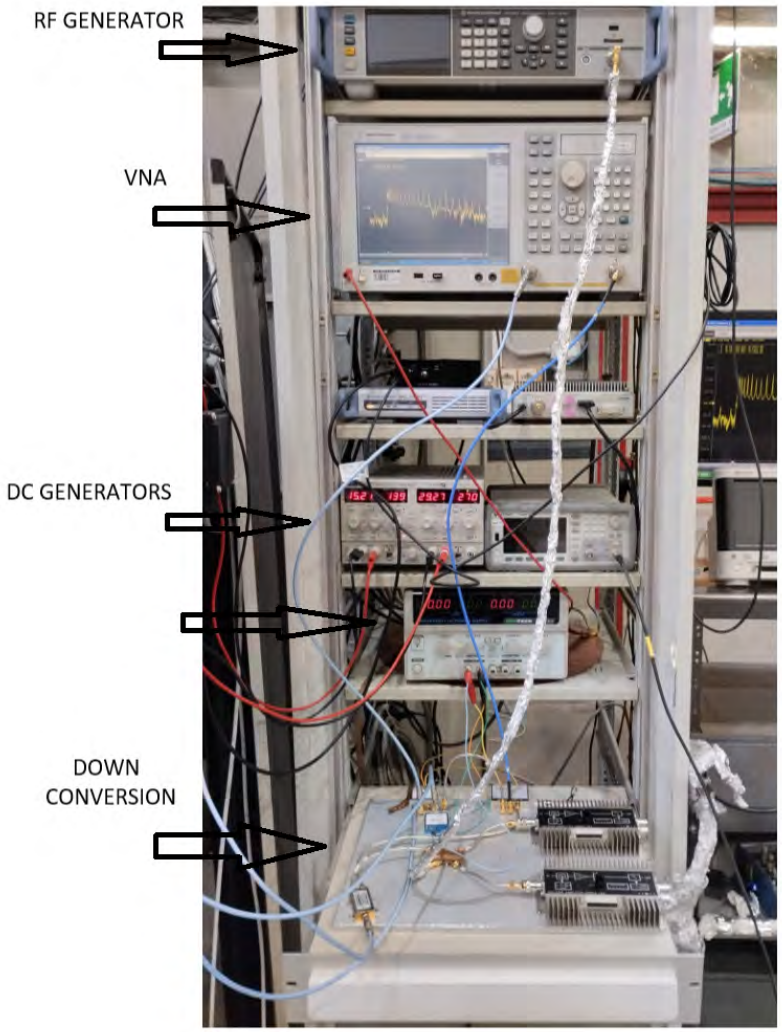

Figure 3.23. [53] A general view on the rack. In it the RF and the DC generators, the VNA and the down conversion part that connects the output line of the cryostat with the data acquisition board are all present.

As mentioned earlier, the **mixer** plays a central role in the down conversion stage. But why we need this? The dominant motivation is that the available ADC board in the laboratory can't work in the RF regime so thanks to the mixer we

can take the signal from L5 that comes out from the FET and bring it to $\sim$ MHz frequencies.
A mixer is a non linear component with two signals as input. The IQ outputs, instead, correspond respectively to the real and imaginary part of a base-band frequency signal. We can see it, together with all the other down conversion part, in Fig. 3.24.
This part of the setup starts with the splitter S1 that collect the signal that comes out from the FET. Just as the name implies, it splits the incoming signal in two to redirect it to the down conversion (mixer) and acquisition electronics (VNA through the switches). The splitter is then very useful, although it induces some losses of $\sim$ 3 dB to the whole line.

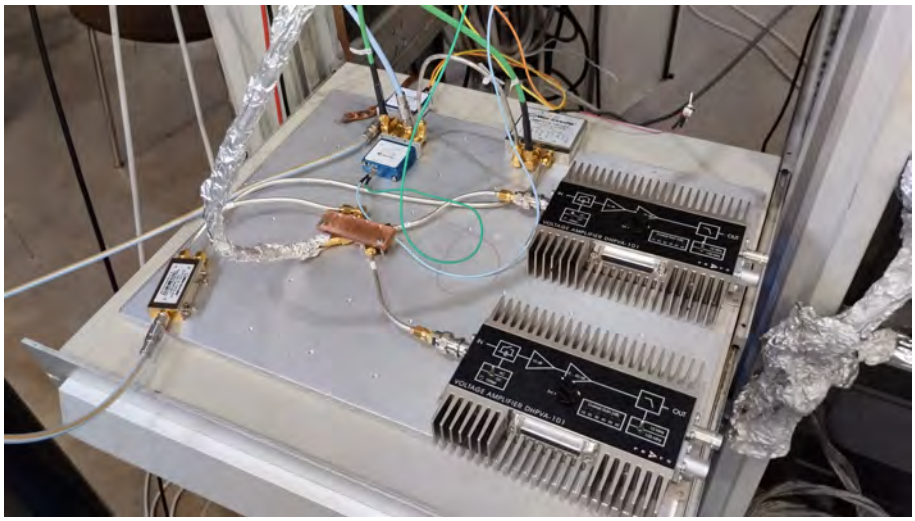

Figure 3.24. [53] A zoom on the down conversion part: the splitter S1 takes the output coming from L5 and brings it to one IQ mixer. Here the signal is down converted and then the I and Q outputs are first amplified by two low noise voltage amplifier and then acquired by a 16 bit ADC board.

Here it follows the role of the I–Q mixer: its RF port is connected with the L5 that goes through the splitter while its LO port, that stands for local oscillator, comes from the RF generator as we anticipated before. From the I-Q ports then the two signals I and Q are generated, characterized by a frequency equal to the difference between the two input ports.
In this sense the LO port has to be interpreted: it provides a reference rf signal from which one can see the differences with the signal that comes from inside the resonant cavity, which should include in it the expected axion signal. We will return to this in the next chapter which concerns all the data analysis to detect an axion signal.
Therefore, as we said, the I–Q mixer converts the frequency to the baseband, and the I and Q quadratures are amplified by low-noise voltage amplifiers ($\times 10^3$ factor, 10 MHz bandwidth) before being digitized by a 16-bit ADC board, which has a 2 MHz bandwidth and sampling of 2 MS/s.

Chapter 4

Axion search with QUAX @ LNF

4.1 Calibration procedures

In the last chapter we have discussed the principle of operation of a microwave resonant cavity, together with all the surrounding experimental setup which constitutes an Haloscope in its wholeness. We have specifically described the operating principle of the QUAX experiment. We now have everything we need to go straight into the data acquisition and analysis description.
This chapter provides a detailed description of the calibration procedure and the data acquisition process at each experimental point, along with the final data analysis. At the end of this work, then, we will be able to present the first experimental results obtained with the new haloscope of the QUAX experiment at LNF.
In what follows I will cover the work done in [9], focusing more specifically on the work that I have done in my own.

4.1.1 Scattering parameters acquisition

After the cool-down of the apparatus, the following procedure is used for calibrating and taking data at each frequency step, starting from the first measured value of 8.8317690 GHz:

- The cavity frequency is set moving the ANR240 motor step by step while monitoring the transmission scattering parameter from the VNA. Each time the frequency is increased by one cavity bandwidth, about 260 kHz, with respect to the previous data taking.

- The waveforms of the scattering parameters S_{21}, S_{22} and S_{12} are collected through the VNA thanks to all the possible configurations in which we can put the system due to the role of the four switches (RT1, RT2, RT3, CR7) and of the two circulators (C1, C2); along with the features of the VNA.
  Referring to the line numbering in Fig. 3.13 we can see which lines are used for each of the scattering parameters. S_{21} is acquired measuring from L5 an injected signal from L1, S_{22} measuring from L5 an injected signal from L3 and S_{12} measuring from L1 an injected signal from L3.

- The raw data acquisition is started, lasting about 3600 s.

The data acquisition for the subsequent analysis consists in recording the power coming from the output line L5. But certaintly, to use this data, we need to calibrate the output power and then to know the gain of the readout line.
The problem here resides in the fact that after the cool-down of the apparatus we can't measure any of the components inside the cryostat, unless via input signals we can inject thanks to the VNA through the lines of the cryostat.
Therefore we follow the procedure developed in [61]; the first step is that the RF diagram of Fig. 3.13 can be represented, in dB units, by the following system of three coupled equations:

$$\begin{aligned} S_{21} &= G_{L1} + S_{21}^{cav}(\nu_c, Q_0, k) + G_{L5}, \\ S_{22} &= G_{L3} + S_{22}^{cav}(\nu_c, Q_0, k) + G_{L5}, \\ S_{12} &= G_{L1} + S_{12}^{cav}(\nu_c, Q_0, k) + G_{L3}, \end{aligned} \tag{4.1}$$

where with S_{21} we refer to the measured scattering parameter while with S_{21}^{cav} we refer to the intrinsic parameter which doesn't include the various amplification/attenuation of the lines. The function S_{21}^{cav} depends on cavity parameters that will be estimated through the fitting procedure, such as the resonant frequency, the intrinsic quality factor, and the coupling coefficient k_2. Since k_1 is fixed, determining k_2 also allows us to obtain the total coupling $k = k_1 + k_2$.
We have now then a system of three equations in three indipendent variables: G_{L1}, G_{L3} and G_{L5} that are the attenuations/gains of the respective input and output lines and therefore what we are trying to estimate with the calibration procedure.
To describe what is done in practice, let's examine a specific experimental point in its entirety: we will now focus on the fifth Cavity resonance frequency taken that corresponds to $\nu_c = 8.83282190$ GHz.
As we anticipated before, the various configurations in which we can put all the four switches allow us to measure all the scattering parameters of the resonant cavity. In particular, to measure the transmission scattering parameter S_{21} we have to send an input signal from one channel of the VNA to one port of the cavity and collect the electromagnetic signal through its second port that have to be connected with the second channel of the VNA. As it can be seen in our specific configuration of Fig. 3.13 then, in this case we use the line L1 to send the input from the VNA and the line L5 that is designed as output and therefore has all the amplification chain mounted in it.
The calibration procedure then continues with the use of the switches, whose role is to allow the measurement of the remaining scattering parameters. By applying a nominal DC signal, we can change their configuration as needed. Particular care must be taken with the cryogenic switch CR7: since it is located inside the cryostat, the applied DC signal causes heating of the system. After switching its configuration, it is therefore necessary to wait a few minutes for the cavity to cool down before proceeding.
Returning to the scattering parameters, let us now consider the measurement of the reflection coefficient S_{22}. In this case, the input signal is sent into one port of the cavity and the reflected signal is collected from the same port. According to our convention, port 1 is connected to the cryogenic switch CR7, while port 2 is located near the circulator C1. Therefore, to measure S_{22}, we send the signal through line L3 and detect the reflected signal via L5. The circulator C1 plays a key role here, serving both to direct the RF signal in a specific direction and to isolate the cavity from the HEMT amplifier. In the measured S_{22} coefficient, we observe the combined effect of L5's amplification chain and the -40 dB attenuation introduced by the two attenuators on L3, as well as the intrinsic losses of both lines. This makes S_{22}

significantly different from S_{21}, which is affected only by the amplification on L5 and is therefore more strongly amplified. It is also notably distinct from the last scattering parameter we will discuss next.
The other transmission coefficient S_{12}, theoretically the mirror of S_{21}, is in practice measured using as input the line L3 and as output the line L1. What is specific here is that we can't use the designed output line L5 and so we were forced to bypass the amplification chain. This resulted in a weaker signal for this last parameter and a noisier waveform.
In Fig. 4.1 are therefore plotted the module of the three coefficients: via the VNA we take both the real and imaginary part of all of them but for the fits that we are going to discuss we worked with modules because it was easier than working with the phases of the functions. The three coefficients appear in descending order of amplification, consistently with the configuration of the input/output lines of the cryostat and the methods used to measure S_{21}, S_{22} and S_{12}. Before providing a detailed discussion of the plots, we first need to introduce the fitting functions employed. For now, it is important to note that the plots are shown in linear units, and unless otherwise specified, all subsequent analysis will be carried out in linear scale rather than in decibels (dB).

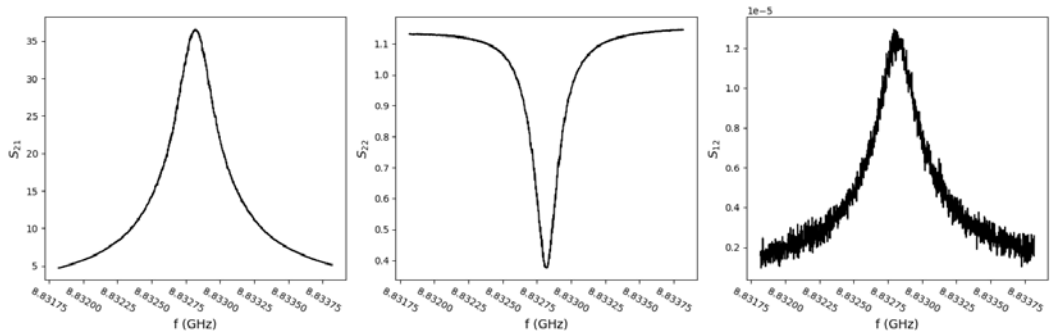

Figure 4.1. Modules of the experimental data acquired from the VNA of the three coefficients, in order: S_{21}, S_{22} and S_{12}.

In Section 3.1.3 we derived an expression of the Lorentzian functions of the cavity S_{ij}^{cav} that enters in Eqs. (4.1). For simplicity we rewrite them below, let's recall from Eq. (3.49) the expression for the two trasmission coefficients, from Eq. (3.47) the reflective coefficient and take the modulus of all of them:

$$S_{21}^{cav} = S_{12}^{cav} = \left| \frac{2\sqrt{k_1 k_2}}{1 + k_1 + k_2 + jQ_0\delta} \right|; \tag{4.2}$$

$$S_{22}^{cav} = \left| \frac{k_2 - (1 + k_1 + jQ_0\delta)}{1 + k_1 + k_2 + jQ_0\delta} \right|, \tag{4.3}$$

where k_1 is the coupling to the fixed antenna, k_2 is the coupling to the mobile antenna, Q_0 the intrinsic quality factor and

$$\delta = \frac{\omega}{\omega_0} - \frac{\omega_0}{\omega}, \tag{4.4}$$

with ω_0 as resonant frequency.
Let us temporarily assume all the fit parameters as given. Fig. 4.2 shows the three scattering coefficients used in the data analysis. It is worth noting that in the fits,

the parameter k_1 is kept fixed at 1.4×10^{-3}, a value obtained from simulations. At the end of this section, we will justify this assumption.

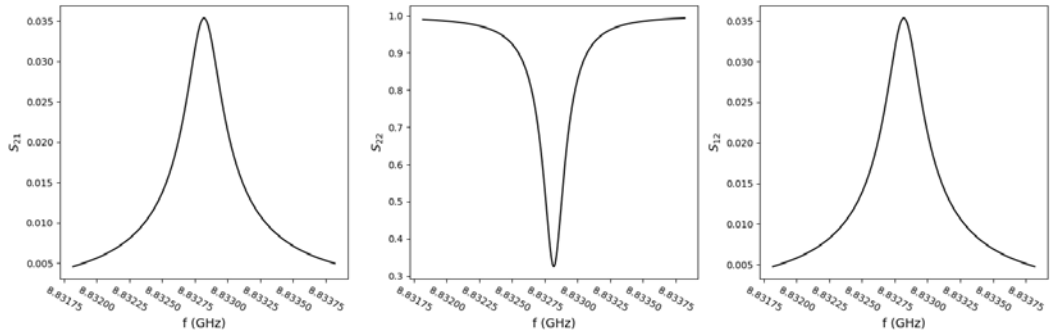

Figure 4.2. Plots of the theoretical functions of the three coefficients using the parameter estimated from the subsequent fit.

S_{21}^{cav} and S_{12}^{cav} share the same lorentzian function and are theoretically identical, infact, Eq. (4.2) is symmetrical in the two couplings then in principle the two transmission coefficients are the same. Let's infact look at Fig. 4.2, the two functions have the same trend and the same values. In particular, if we calculate the value at the resonance, so by setting $\omega = \omega_0$ and then $\delta = 0$, we obtain $S_{21}^{cav} = S_{12}^{cav} = 0.0353$. This two values that are ideally the same, in the practical world can be very different. If we look in fact to Fig. 4.1, we note that the shape of the functions are still lorentzians but the values are very different from each other due to the fact that the way we measured the two transmission coefficients is not the same. In our experiment, we measured S_{21} using lines L1 and L5, with L5 being the output line connected to the amplification chain. In contrast, S_{12} was measured using lines L1 and L3, which do not include the output line. As previously mentioned, only L5 contains amplifiers, while L3 not only lacks amplification but also includes two additional 20 dB attenuators, along with its intrinsic attenuation. This difference has a significant impact: at resonance, for example, the measured value of S_{21} is about 10^6 times larger than that of S_{12}. Furthermore, the absence of amplification in the S_{12} path results in much noisier data, as visible in Fig. 4.1 and as we will further discuss during the fitting procedure.
Before finally moving on to treat the fits, it's important to discuss about S_{22}^{cav} and its behavior too. Unlike the other two lorentzians, this last one has a hole on the resonance instead of a peak and, as we can see in Fig. 4.2 and in Eq. (4.3), for frequencies relatively distant to ω_0 the reflective coefficient tends to one. Also for this function we can see the effect of the amplification chain, in the experiment we measured S_{22}^{cav} through the lines L3 and L5 so we had to use both the lines with 40 additional dB of attenuation and the line with all the amplifiers. In Fig. 4.1 it can be seen that the two contributions more or less balance each other and in fact S_{22} it is almost not amplified or attenuated at all with respect to S_{22}^{cav} of Fig. 4.2. This description was quite qualitative, let's finally move on to the description of the fitting procedure that will also allow us to treat all the previous discussion in a more quantitative way.

4.1.2 Fit procedure

The calibration procedure is therefore done by a simultaneous fit of the S_{21}, S_{22} and S_{12} spectra with their analytical expressions, allowing the extraction of

the cavity parameters ν_c, Q_0, $k_{1,2}$ and of the attenuation and gain of the input and output lines. In particular, we are interested in the gain of line L5, which is calculated solving the system of Eq. (4.1) from which we can calculate also the value of L1 and L3. From the fit we can only extract the gain/attenuation of the scattering parameters therefore of the combined effect of the two lines that constitute a measured parameter, for example from the fit of S_{21} we can extract the combined effect of L1 and L5.
For the experimental data of the scattering parameters we acquire from the VNA both their real and imaginary part and then we calculate and plot their module. We do the same thing for the fit too, in considering the analytical expressions of the functions we start from the real and imaginary part separated. Let's treat first S_{21} and S_{12} that have the same analytical expression, we start from:

$$S_{21}^{cav} = S_{12}^{cav} = \frac{2\sqrt{k_1 k_2}}{1 + k_1 + k_2 + jQ_0\delta}, \tag{4.5}$$

and identifying

$$A = \frac{2\sqrt{k_1 k_2}}{1 + k_1 + k_2}, \tag{4.6}$$

we separate the real and the imaginary part:

$$S_{21}^{cav} = \frac{A}{1 + Q_L^2\delta^2} - j\frac{AQ_L\delta}{1 + Q_L^2\delta^2}, \tag{4.7}$$

where now the loaded quality factor appears with its expression

$$Q_L = \frac{Q_0}{1 + k_1 + k_2}. \tag{4.8}$$

We now calculate the module of the function that is the analytical expression we use to fit our experimental data:

$$|S_{21}| = Abs_{21}\frac{2\sqrt{k_1 k_2}}{\sqrt{(1 + k_1 + k_2)^2 + {Q_0}^2\delta^2}}, \tag{4.9}$$

where Abs_{21} is a parameter that we added a posteriori and identifies the contribution of the lines, in this specific case L5 and L1, to which S_{21} is subjected. More precisely is the number we sought before when we had to understand how much are amplified S_{21} data of Fig. 4.1 with respect to the analytical function S_{21}^{cav} of Fig. 4.2.
Before introducing the analytical expression for the reflection coefficient, it is worth noting that the expression for S_{12} is nearly identical to that of the other transmission coefficient, except for the parameter Abs_{12}, which in this case accounts for the influence of lines L1 and L3. The S_{12} fitting function is then:

$$|S_{12}| = Abs_{12}\frac{2\sqrt{k_1 k_2}}{\sqrt{(1 + k_1 + k_2)^2 + {Q_0}^2\delta^2}}. \tag{4.10}$$

Now, for the reflection coefficient, let's start from its analytical expression:

$$S_{22}^{cav} = \frac{k_2 - (1 + k_1 + jQ_0\delta)}{1 + k_1 + k_2 + jQ_0\delta}. \tag{4.11}$$

ν_c (GHz)	Q_0	k_2	Abs_{21}	Abs_{22}	Abs_{12}	q
8.8328	48950	0.5098	1031	1.1488	347.3×10^{-6}	0.01

Table 4.1. All the parameter estimated from the fit and their values.

In this case too we separate the real and imaginary part in order to calculate the module of the function:

$$S_{22}^{cav} = \frac{{k_2}^2 - (1+k_1)^2 - (Q_0\delta + q22)^2}{(1+k_1+k_2)^2 + {Q_0}^2\delta^2} - j\frac{2k_2Q_0\delta}{(1+k_1+k_2)^2 + {Q_0}^2\delta^2} \tag{4.12}$$

where we also added a posteriori the term q that is a parameter accounting for the small asymmetry in the reflection coefficient, an effect that we will see more specifically later on this work. We can now calculate the module of the complex function, adding in this case too the term concerning the contribution of the lines to which the scattering parameter is subjected:

$$|S_{22}| = Abs_{22}\sqrt{Re^2 + Im^2}. \tag{4.13}$$

Having all the analytical expression and the data we therefore perform a simultaneous fit of all the three scattering parameters together at each frequency step of the experiment. In this thesis only one experimental point is presented but the work was repeated identically and systematically for the other frequency points. Keeping then k_1 fixed, through the fit of Fig. 4.3, we estimate all the other parameters useful for the characterization of the cavity and of the lines of the cryostat such as ν_c, Q_0, k_2, Abs_{21}, Abs_{22}, Abs_{12} and q.

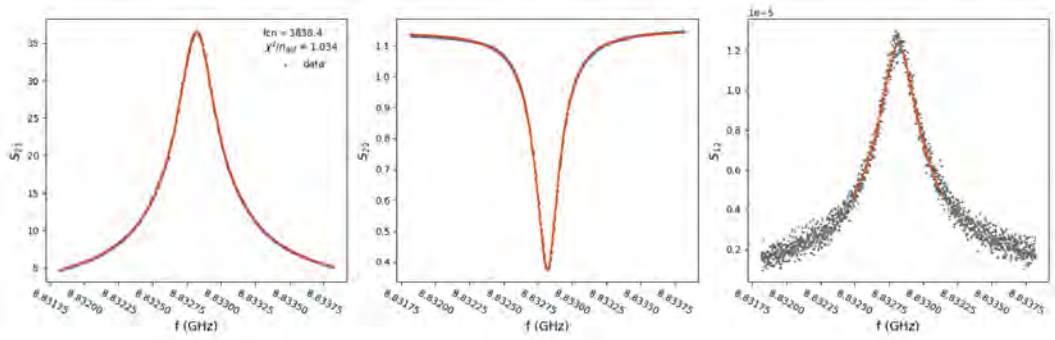

Figure 4.3. Fit example of the scattering parameters to extract the cavity parameters and the contribution of the lines.

What can be noticed is the larger noise on the S_{12} coefficient due to the large attenuation of the combined effect of L1 and L3 together. For this reason, we chose to perform the fit over a narrow frequency range centered around the resonance, excluding the data points in the tails, which are significantly noisier. Despite this restriction, the fit still provides a good agreement with Eqs. (4.1).
A quantitative proof of the larger noise and of the different ways of amplification/attenuation of the three measured coefficients can be seen instead in Tab. 4.1, here the three gains of the three scattering parameters are reported in linear units, together with the other parameters estimated from the fit. A discussion on the extracted parameters of the resonant cavity such as ν_c, Q_0, and k_2 can be found in

Section 4.1.4 while in Section 4.2 the q term added in Eq. (4.12) will be taken into account.
This extracted numbers confirm the discussion we did in a qualitative way before: from Abs_{21} we can see the amplification done in L5, from Abs_{22} the combined effect of amplification of L5 and attenuation of L3 and finally, from Abs_{12} it is evident the effect of attenuation of L3 alone. This three multiplicative factors are the numbers that will have the key role in obtaining the effective amplification of L5 alone which will bring us to the conclusion of the calibration, but before we get into it let's spend a few more words on the fit procedure.

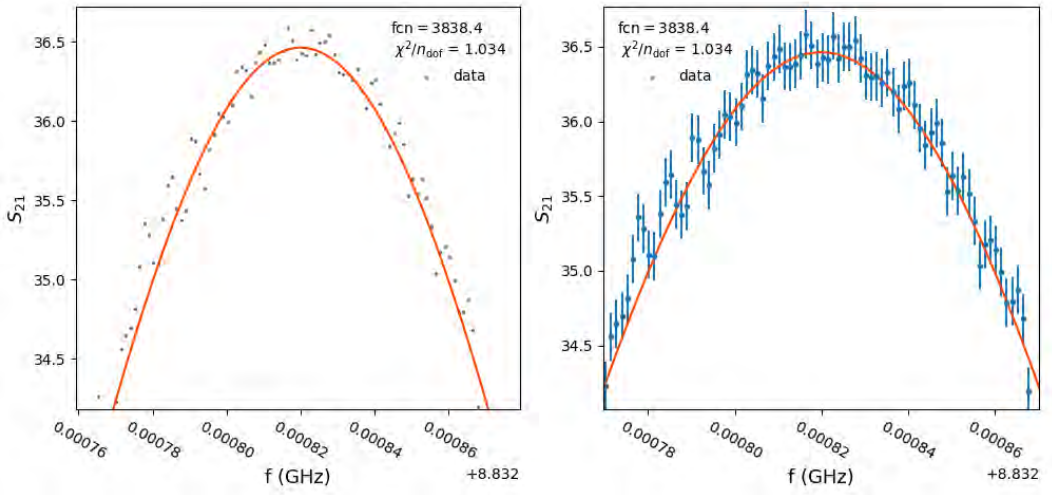

Figure 4.4. Zoom around the resonance of the fit on S_{21}, one with and one without the estimated statistical error.

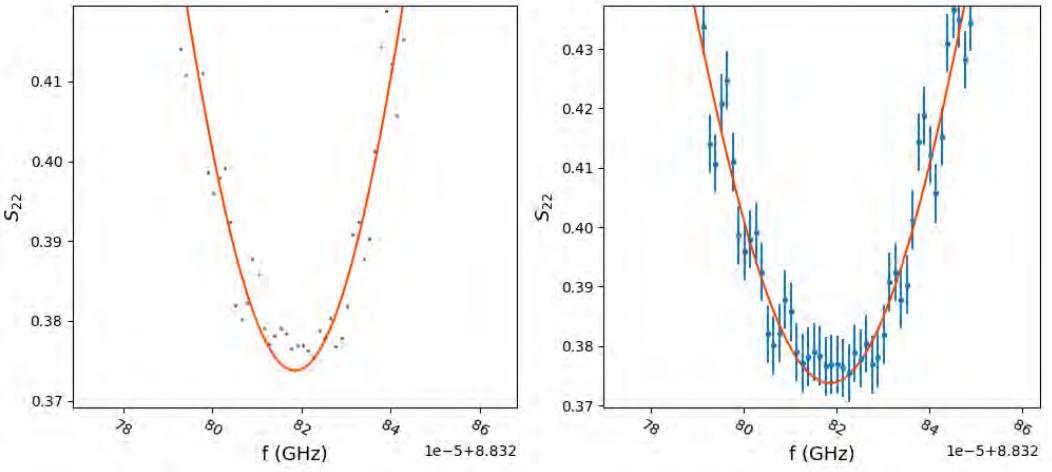

Figure 4.5. Zoom around the resonance of the fit on S_{22}, one with and one without the estimated statistical error.

The fits for each of the scattering parameters of Fig. 4.3 are shown in Fig. 4.4, Fig. 4.5 and Fig. 4.6, respectively. In each of the figures, on the left is shown a simple zoom around the resonance omitting the error bars of the points for graphic

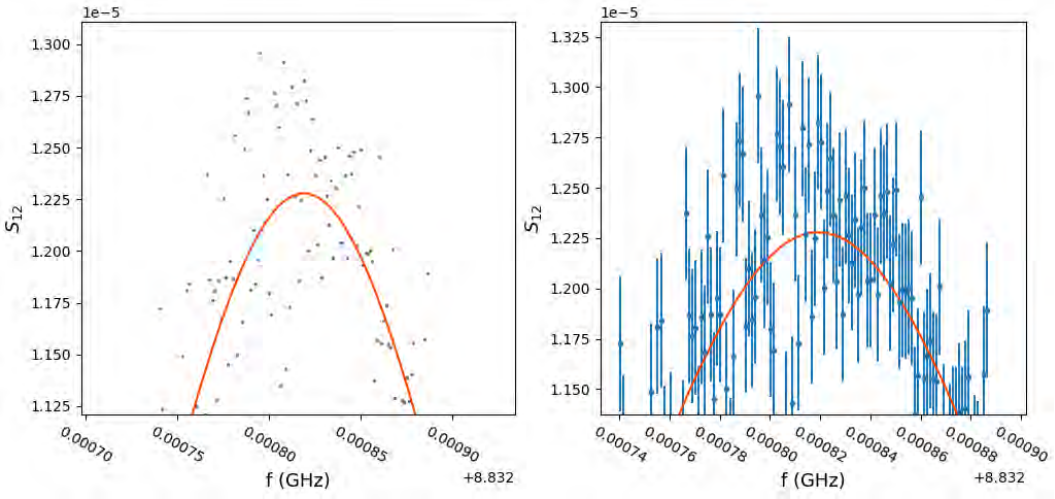

Figure 4.6. Zoom around the resonance of the fit on S_{12}, one with and one without the estimated statistical error.

purposes, while on the right error bars are present. In this way it can be noticed more clearly the goodness of the fit done: the points are described very well by the functions used, this can be seen above all from the S_{21} and S_{22} parameters while it cannot be stated with the same confidence for the S_{12} coefficient, it is in fact immediate to see that the points in the latter figure are noisier.
Points with greater noise also mean larger error bars, it can actually be seen the larger relative error in the right plot of Fig. 4.6 with respect to the other coefficients. In all three cases, anyway, the error bars give us a quantitative estimate on the quality of the fit: in all the three figures the experimental points lie on the theoretical curve within the calculated error. The error was estimated from the residuals between the experimental data points and the theoretical function, using the best fit parameters. We then created a histogram of the residuals and fitted it with a Gaussian to extract the mean and standard deviation. This procedure was carried out separately for each scattering coefficient. However, only the histogram for S_{12} is shown below in Fig. 4.7, as only the statistical error derived from S_{12} was used to estimate the uncertainty on line L5, which will be discussed in more detail in the next subsection. This choice was made because, as can also be seen from the plots, the relative statistical error on S_{12} is larger than that of S_{21} and S_{22}. As a result, only the uncertainty on S_{12} significantly contributes to the total statistical error on G_{L5}.

Fig. 4.7 shows the histogram of the S_{12} residuals along with its Gaussian fit. As expected, the mean is approximately zero, while the standard deviation is $\sigma = 3.35 \times 10^{-7}$, which corresponds to a relative error of $\sigma_x/x = 0.027$ when taking the experimental value at resonance as a reference.
Before proceeding with the discussion of the gain of L5 and its error, it makes sense to at least mention the Iminuit library that we used to write the fit codes: it gives us also the reduced χ^2 from each fit as an index of its success and it is displayed in all the figure regarding this topic in the S_{21} plot. This was one of my main works during my internship at LNF, having had the responsibility to do the fit for each experimental frequency of the QUAX run, modifying and adapting for this analysis the starting code of Dr. Alessio Rettaroli.
We have now finally all the ingredients necessary to calculate the gain of line L5,

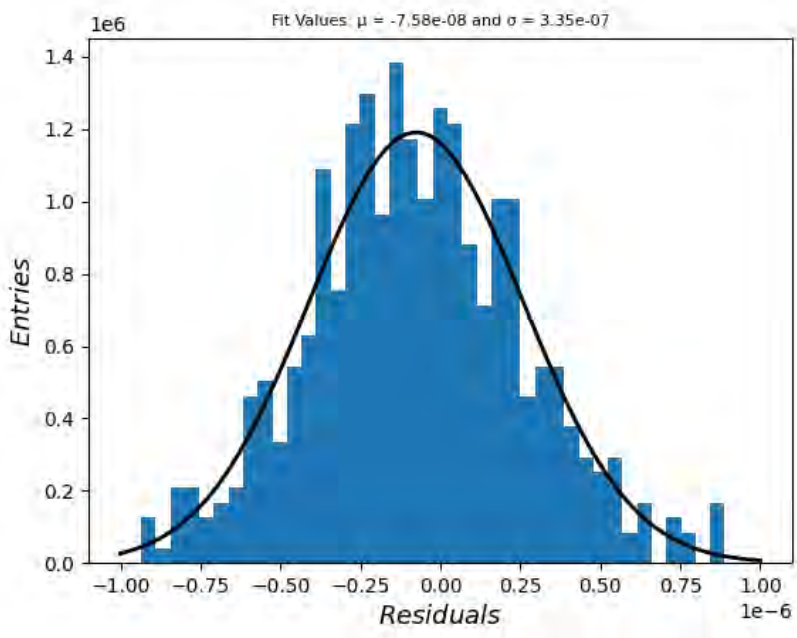

Figure 4.7. Histogram of the residuals of the S_{12} coefficient.

upon solving Eqs. (4.1) the gain in dB of the readout line is:

$$G_{L5} = \frac{(S_{21} - S_{21}^{cav}) + (S_{22} - S_{22}^{cav}) - (S_{12} - S_{12}^{cav})}{2}, \tag{4.14}$$

evaluated as the average of the spectrum. This gain was calculated for all the subruns of the experiment, this means that for all the frequency we did the combined fit of the three coefficient and then having estimated each time the parameters as in Tab. 4.1, we calculated the gain of L5 at the resonance using Abs_{21}, Abs_{22} and Abs_{12} converted from linear to dB:

$$G_{L5} = \frac{20log_{10}(Abs_{21}) + 20log_{10}(Abs_{22}) - 20log_{10}(Abs_{12})}{2}. \tag{4.15}$$

The maximum spread of the G_{L5} values within all the subruns is only 0.4 dB as it can be seen in Fig. 4.8 , so we can reasonably consider the gain constant in the evaluated frequency range and equal to the average value of $G_{L5} = 70.62$ dB. This value is referred at the input of the splitter so its not the value that we obtain from Eq. (4.15) but we have to consider another contribution. Since the S parameters are measured to and from the VNA ports, to calculate the right value for G_{L5} the contributions of the splitter (-3 dB) and of the cable from the splitter to the VNA have been subtracted.

The measured gain through all the sub-runs is then:

$$G_{L5} = (70.62 \pm 0.28_{syst.} \pm 0.13_{stat.})\ dB, \tag{4.16}$$

where the systematic uncertainty is mainly due to the gain flatness of the reconstructed G_{L5}, and the statistic uncertainty derives from the data scattering of the S_{12} trace.

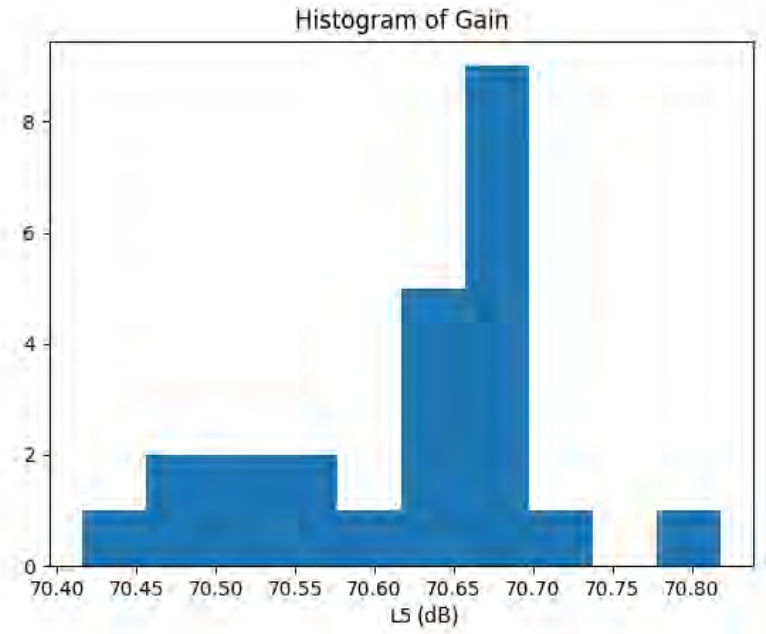

Figure 4.8. Histogram of the gain on L5 estimated from all the sub runs of the QUAX run.

4.1.3 Systematic and statistical effects

In the last subsection we arrived to our goal of the calibration procedure: we estimated the total gain on the output line (L5) of the cryostat. It's now time to discuss about the two errors that appear in Eq. (4.16). We have also already discussed about the statistical error on the S_{12} parameter but we dealt only the specific case of one of the experimental frequencies. We have to repeat each time for each frequency the procedure that brought us to Fig. 4.7, then after each fit we calculate the residuals between any S_{12} coefficient and its theoretical curve in order to obtain the statistical uncertainty deriving from the data scattering. Instead of plotting each histogram for each point and evaluating the statistical dispersion in each case separated, we calculate the residuals for all the frequency points and then we build the cumulative vector that contains the sum of all the individual residual vectors corresponding to the experimental points.
Considering then all the sub runs, we obtain a resulting cumulative histogram shown in Fig. 4.9, as expected it's not that different with respect to the histogram of a single frequency like the one of Fig. 4.7, but obviously having a lot more entries its much more gaussian. Operating in this case too a gaussian fit, we obtain a mean value of around zero with good approximation and a dispersion of $\sigma = 3.6 \times 10^{-7}$, which is in agreement with the value found for the single experimental point, but it deviates a bit from that due to the fact that now we are considering all the sub runs together.
Having all our experimental point and the fit parameters in linear form, this statistical uncertainty found from the residuals is in linear units too. The way to estimate the statistical uncertainty of G_{L5} shown in Eq. (4.16) is to propagate the uncertainty of S_{12} through Eq. (4.15), considering that we have to convert our values from linear to dB units. Thanks to the discussion we did for the statistical uncertainty on all the three coefficients, we now assume that only S_{12} contributes in a significant

way to the propagated error because its relative error is greater than the other two parameters. Therefore propagating the errors in Eq. (4.15), using $\sigma = 3.6 \times 10^{-7}$ found from the cumulative histogram, we have found the statistical uncertainty on G_{L5} shown in Eq. (4.16).

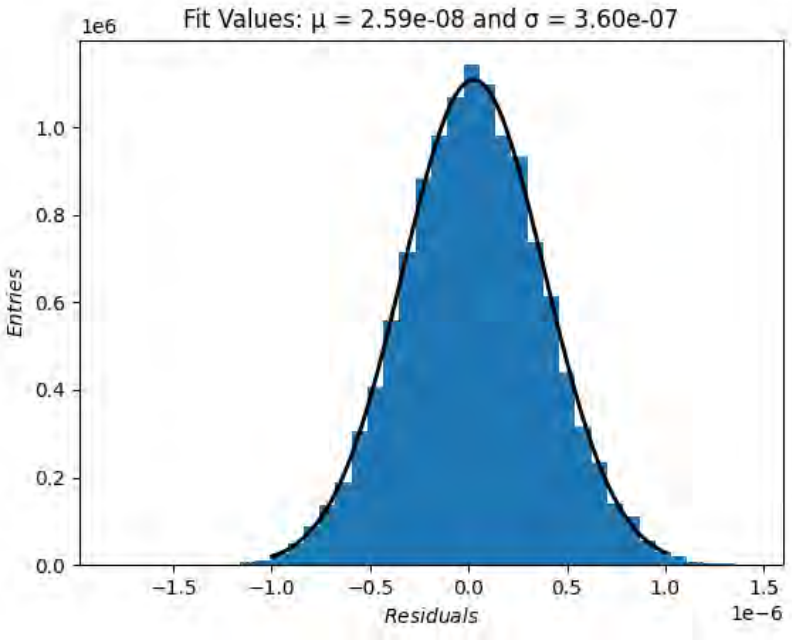

Figure 4.9. Cumulative histogram of the residuals of the S_{12} coefficients regarding all the experimental point of the QUAX run.

We have to talk now about the systematic uncertainty too. The procedure to estimate it is similar to the one just discussed but its source is different. The value we obtained for G_{L5} has been calculated from Eq. (4.14) and Eq. (4.15) but using only the value of each parameters at the resonance. It can actually be seen from Eq. (4.14) that we have to consider all the experimental points acquired from the VNA and not only the points at the resonance. All this points around the resonance and at the tails in fact contribute to the deviation from the gain flatness of the reconstracted G_{L5}.
In practice, the procedure consists in taking the difference between the experimental data acquired with the VNA (Fig. 4.1) and the theoretical curves obtained using the parameters from the fits (Fig. 4.2). This process was carried out for each sub-run, but we focus here on the specific case analyzed in detail.
For each sub-run, the gain of line L5, G_{L5}, was calculated using Eq. (4.14), considering the full frequency range around the resonance. The results are shown in Fig. 4.10, which presents the gain values as a function of frequency around the resonance corresponding to $\nu_c = 8.8328$ GHz. The value at resonance is highlighted in a different color to emphasize the spread of the other points relative to this central reference, which is used in the subsequent data analysis. It is immediately apparent that the further we move from the resonance, the larger the spread in the data becomes. This behavior is mainly due to the S_{12} coefficient, which, being the noisiest, shows larger deviations from the fitted curve compared to S_{21} and S_{22}.

To estimate the systematic uncertainty, we quantitatively evaluate the deviation

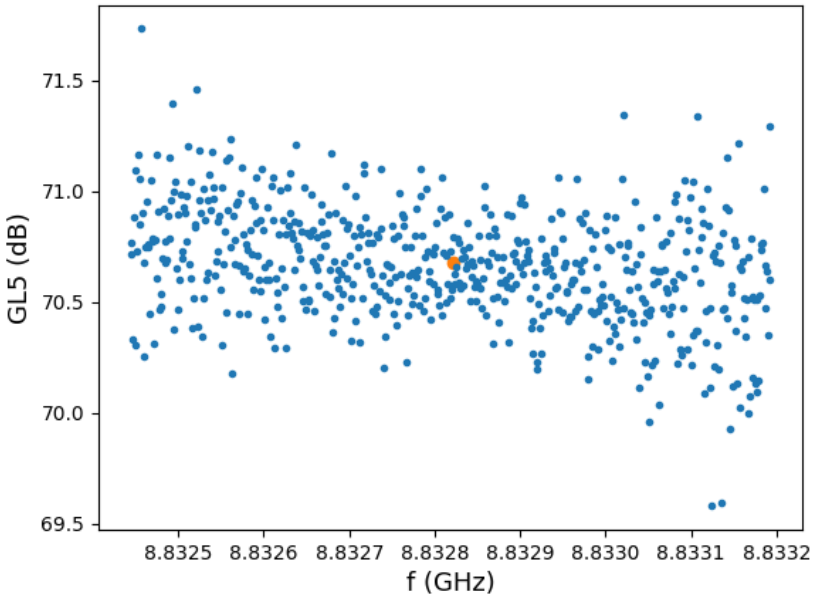

Figure 4.10. Gain of L5 calculated for all the frequency points in a window around the resonance (in yellow) of $\nu_c = 8.8328$GHz .

from gain flatness. This is done by calculating the residuals with respect to the gain at resonance, which is $G_{L5} = 70.68$ dB at $\nu_c = 8.8328$ GHz. The histogram of these residuals, along with a Gaussian fit, is shown in Fig. 4.11. As expected, the mean value is approximately zero, and the standard deviation is $\sigma = 0.25$ dB.
This value differs from the systematic uncertainty reported in Eq. (4.16) because the total uncertainty requires considering all frequency points from the entire measurement set. Therefore, Fig. 4.12 shows the final result of this procedure, repeated for all 24 experimental points of this first run of the QUAX experiment. Residuals were computed for each point and combined into a single cumulative dataset.
The Gaussian fit of this cumulative distribution also yields a mean close to zero, while the standard deviation slightly differs from the previous case. This combined analysis gives a final value of $\sigma = 0.28$ dB, consistent with the estimate in Eq. (4.16). The systematic error estimated in this way includes also a statistical contribution that should be subtracted. We retain it for a conservative estimate.

4.1.4 validation of the assumption on the fixed parameter k_1

Let's discuss briefly about the S_{11} parameter of the cavity. In the beginning we should have used it as the third parameter instead of the S_{12} one in fact, we only have three lines involved in the experimental setup so we need only three parameters to resolve a system of three equations in three independent variables like Eqs. (4.1). The input line L2 is shown in Fig. 3.13 but we used it only as an auxiliary line in the subsequent axion raw data acquisition as we will see later. Returning to S_{11}, It is more directly measurable than the S_{12} because it requires the use of only the line L1. This parameter would have added an equation in the system of Eqs. (4.1) like

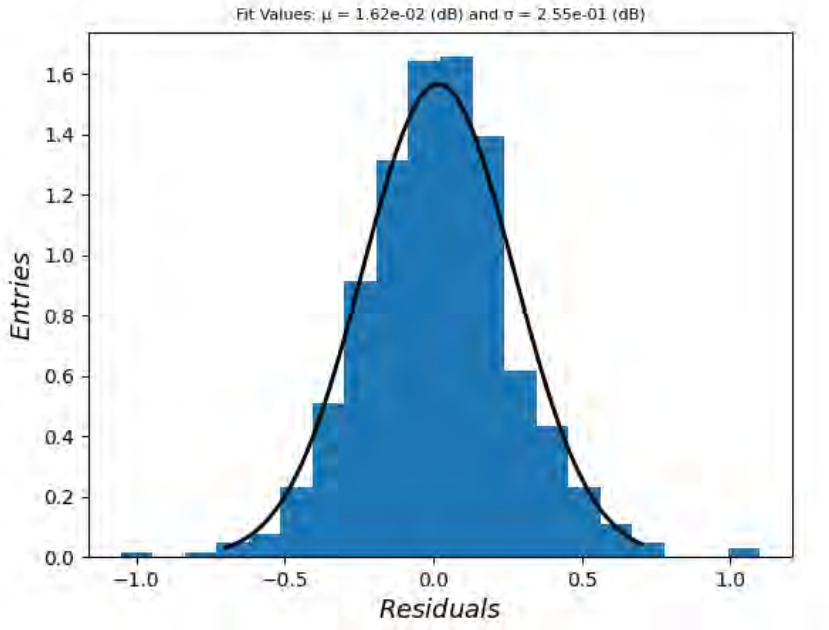

Figure 4.11. Histogram of the residuals of all the different G_{L5} (Fig. 4.10) with respect to the central G_{L5} calculated at the resonance point of $\nu_c = 8.8328$GHz.

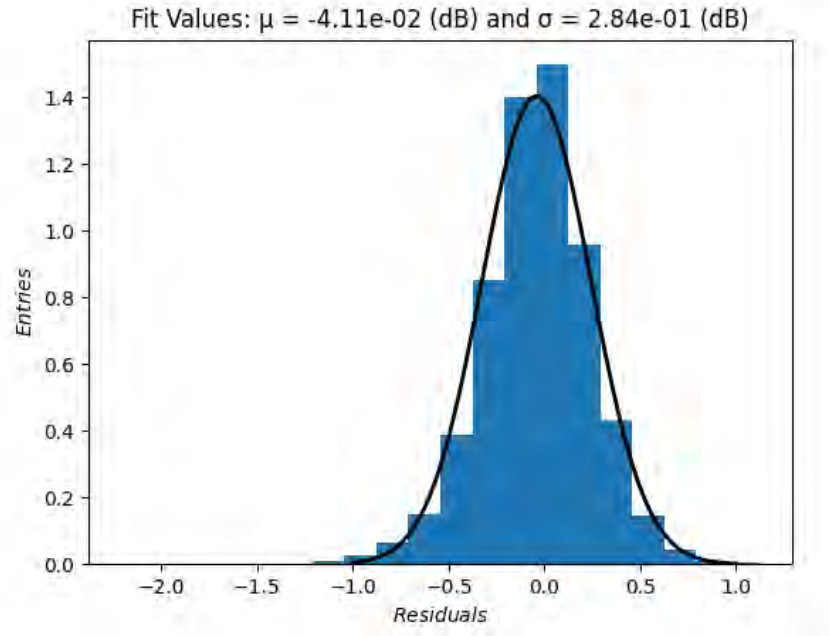

Figure 4.12. Cumulative histogram of the residuals of G_{L5} regarding all the experimental point of the QUAX run.

the one below:

$$S_{11} = 2G_{L1} + S_{11}^{cav}(\nu_c, Q_0, k). \tag{4.17}$$

In principle an equation like this was much better both for resolving the system and for the measurement procedure but in practice it turned out to be more challenging to measure S_{11} than the S_{12} coefficient, although, as we showed, this latter one resulted in a waveform with a lot of noise attached. However, the S_{11} parameter was not discarded a priori but it was measured anyway and used for other purposes than those expected. In fact, it was used for experimental verification of the fixed coupling parameter k_1.
In Fig. 4.13 the S_{11} parameter of the frequency point we examined in depth ($\nu_c =$ 8.8328 GHz) is shown, thanks to the experimental setup of Fig. 3.13 we were able to measure this parameter using only L1 to send the input via the VNA and to receive the output using the same line.

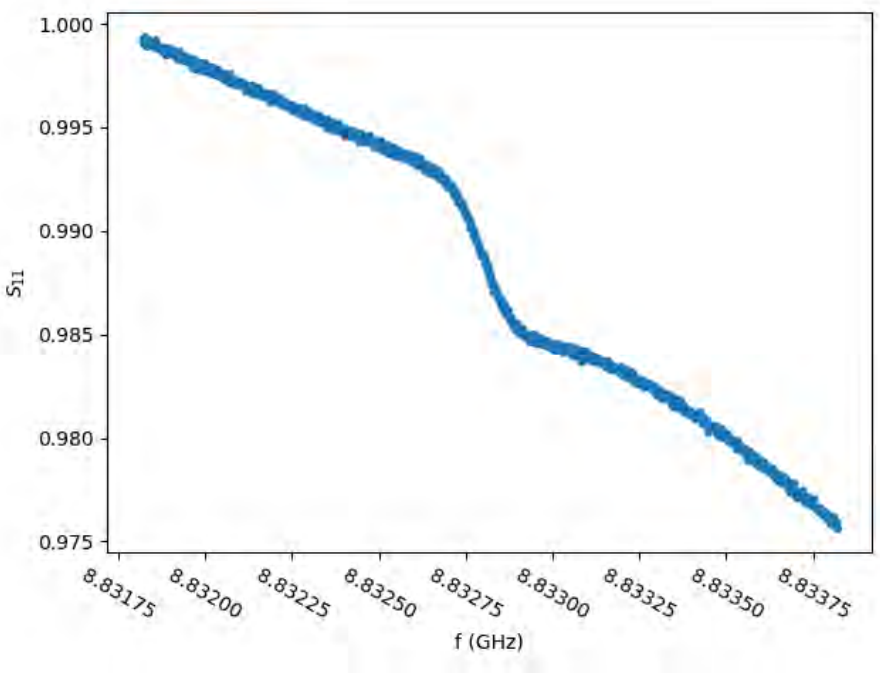

Figure 4.13. Normalized reflection scattering parameter S_{11}. It is not shown the directly measured one, but the cavity S_{11} which doesn't include all the contributions from the lines.

The S_{11}^{cav} coefficient has the same aspect of S_{22}^{cav} in Eq. (4.11) but with k_1 and k_2 exchanged:

$$S_{11}^{cav} = \frac{k_1 - (1 + k_2 + jQ_0\delta)}{1 + k_1 + k_2 + jQ_0\delta}. \tag{4.18}$$

In Fig. 4.13 we notice that the experimental points don't follow the theoretical lorentzian curve expected, in fact we don't have a hole corresponding to the resonant frequency point but a flex. This behavior is most likely due to interference with reflected signals down the coaxial cable of L1 in the frequency range of our interest around the resonance. For this reason we should have parameterized the theoretical curve that describes our experimental point in another way. This would have allowed us to estimate all the expected parameters of the lorentzian curve as we did for S_{21}, S_{22} and S_{12}. It was preferred though to not proceed along this path and to make an easier fit on the S_{12} instead, in fact we needed only three of the four parameter available in order to solve the starting system of Eqs. (4.1).

It is now appropriate to provide a justification for the assumption made in fixing the value of the coupling parameter k_1. This parameter was kept equal to the value $k_1 = 1.4 \times 10^{-3}$, consistent with previous simulation results. The motivations for this choice lies in the fact that, during the experimental measurements, k_1 accounts for the coupling between the resonant cavity and the fixed antenna, which was only minimally inserted into the cavity. This configuration ensured that the total coupling parameter $k = k_1 + k_2$ could be fully controlled by varying only k_2, which was adjusted using the ANPz111 linear stepper motor.
But how can we verify the validity of assuming such a small value for k_1? This is addressed through the analysis of the reflection coefficient S_{11}, as shown in Fig. 4.13. The experimental data points presented in this figure allows for a quantitative assessment of the assumption.
Before discussing the results, it is important to clarify that the data shown in Fig. 4.13 are not raw measurements. They are in fact normalized to obtain the theoretical reflection coefficient S_{11}^{cav} rather than using the directly measured S_{11}, which includes contributions from all gain and loss elements along the signal path. This normalization is evident from the behavior of the function away from resonance, where it approaches unity, as predicted by Eq. (4.18) and consistent with the theoretical expression of S_{22}^{cav} shown in Fig. 4.2.
The normalization procedure followed Eq. (4.17), using the raw S_{11} data and the known attenuation given by $2G_{L1}$. This attenuation was not obtained through fitting, but rather through direct measurement of the combined losses in lines L_1 and L_2. This was made possible by employing the cryogenic switch (CR7) shown in Fig. 3.13, which allows L_1 to be connected directly to L_2. The analysis also relies on the assumption that L_1 and L_2 are identical, assumption that is valid given that the lines inside the cryostat are identical by design and that the coaxial cables from the cryostat to the VNA are equal in length.
Having obtained the normalized reflection coefficient S_{11}^{cav}, we can now validate the assumption on k_1. This is done by estimating k_1 through Eq. (4.18) taking the value of S_{11}^{cav} at resonance and the corresponding fitted value of k_2 at the experimental frequency point we are considering in this analysis, as reported in Tab. 4.1. The resonant point is particularly suitable for this estimation, as it corresponds to $\delta = 0$, simplifying the analysis.
The result of this procedure confirms that, for this specific experimental point, the simulated value $k_1 = 1.4 \times 10^{-3}$ is consistent with an upper bound of $k_1 < 7 \times 10^{-3}$. This supports the validity of the initial assumption and allows it to be extended to the entire measurement run, given that the configuration of L1 remained unchanged across all sub-runs.
Before proceeding to the next stage of the experiment, it is appropriate to summarize the key parameters extracted from the 24 datasets, with particular attention to the coupling coefficients. Tab. 4.2 reports, for each sub-run, the values of the resonant frequency ν_c, the loaded quality factor Q_L, and the coupling coefficient k_2. The frequency values clearly confirm that the resonance frequency of the cavity is tuned over a 6 MHz range, spanning from 8.831769 GHz to 8.8377664 GHz, with 24 discrete and equally spaced steps.
Together, the triplet ν_c, Q_L, k_2 provides a complete description of the resonator's electromagnetic behavior for each sub-run. The loaded quality factor Q_L is directly measured from the VNA using the 3 dB bandwidth method, while the coupling coefficient k_2 is obtained from the fits performed on the measured scattering parameters. Since k_1 remains fixed throughout the data-taking procedure, knowledge of both Q_L and the total coupling $k = k_1 + k_2$ allows us to extract the intrinsic quality factor Q_0 for each sub-run via the relation in Eq. (3.35).

ν_c (GHz)	Q_L	k_2
8.83176900	32345	0.5206
8.83203080	32228	0.519
8.83229550	32273	0.5082
8.83255580	32332	0.5141
8.83282190	32387	0.5097
8.83307310	32401	0.5078
8.83334500	32300	0.5097
8.83360070	32503	0.5058
8.83386200	32540	0.5075
8.83412790	32752	0.5014
8.83438580	32573	0.5026
8.83464620	32904	0.5005
8.83490660	32957	0.4984
8.83516350	32863	0.4951
8.83542850	32872	0.4947
8.83568970	33326	0.4881
8.83594630	33051	0.489
8.83620570	33056	0.4894
8.83646975	33104	0.4857
8.83672330	33584	0.4823
8.83698660	33529	0.4803
8.83724500	33659	0.4823
8.83750860	33639	0.4793
8.83776640	33450	0.4793

Table 4.2. Values of the resonant frequency ν_c, the loaded quality factor Q_L, and the coupling coefficient k_2 for each of the sub run of the experiment.

However, a critical point emerged during the calibration process. As can be observed, the total coupling k is consistently around 0.5 for all sub-runs, which significantly deviates from the optimal coupling value for axion haloscope operation, namely $k = 2$. Although the cavity without the tuning rod had an intrinsic quality factor of approximately $Q_0 \simeq 10^5$ at cryogenic temperature, this value was degraded to about 50,000 due to dielectric losses introduced by the PEEK support and the imperfect geometry of the rod itself.
As a consequence, what was originally designed to be an optimally coupled system ($k = 2$) resulted, upon careful calibration, in a system with $k \simeq 0.5$. This discrepancy is further clarified by examining the two possible solutions of Eq. (3.35) for Q_0, given fixed Q_L and k_1. Specifically, for the sub-run at $\nu_c = 8.8328$ GHz, the expected solution corresponding to the design coupling yields $k_2 = 1.968$ and $Q_0 = 96160$, while the actual solution supported by calibration data results in $k_2 = 0.5098$, $Q_0 = 48950$. These two solutions are mathematically symmetric but correspond to physically distinct cavity conditions, only one of which, unfortunately the suboptimal one, was realized in our setup.

4.2 Data Acquisitions

The last section was primarily dedicated to the extraction of the gain of L5 that will serve us to calibrate the power spectrum that we obtained through the data

acquisition and processing that is the next topic we are going to discuss.
For each cavity frequency set moving the ANR240 motor, we collected with the VNA the waveforms of the scattering parameters to perform the calibration and as last step we started the raw data acquisition that lasted about 3600 s for each of the sub runs.
The data acquisition, essentially, consists in recording the power coming from the output line L5. During data acquisition, the switch CR7 is closed on line L2 to avoid noise leakage through the under coupled port, the switch RT1 is closed on the line L1 and the switch RT2 is closed on the switch RT3 which, in turn, is closed on a 50 ohm termination. In this way the cavity is only connected through its second port and L5 with the outside of the cryostat and with the data acquisition section of the experiment. The splitter S1 in fact, allows to redirect the signal to the downconversion and acquisition electronics we have described in Section 3.3.3. Here, with an I–Q mixer we convert the frequency to the baseband, and the I and Q quadratures are amplified by two different low-noise voltage amplifiers ($\times 10^3$ factor, 10 MHz bandwidth) before being digitized by a 16-bit ADC board, which has a 2 MHz bandwidth and sampling of 2 MS/s. In each sub-run, the I and Q signals are acquired for 4 seconds and saved to file. The total amount of files in each sub-run is 941, resulting in an integration time of $\Delta t = 3764$ s.
Simultaneously with the data acquisition, For each dataset of the 24 reported in Tab. 4.2, we calculate the power spectrum by combining the quadratures as I - iQ, computing the FFT and taking the squared module. This procedure is done separately for each of the 941 files of each single rub runs. Therefore, the 941 power spectra obtained from all the individual files are averaged to produce a single final power spectrum, representing the mean of all the individual spectra. At the end of the acquisition we end up then with 24 power spectra, one for each sub run. An example of one resulting spectrum is shown in Fig. 4.14. In this picture the final result of the procedure for one single sub run is present: more specifically the first experimental point corresponding to the $\nu_c = 8.831769$ GHz frequency. All the spectra have a bandwidth of 2 MHz due to the ADC board used and are centered at the LO frequency, which is always set at $\nu_{LO} = \nu_c - 500$ kHz for each single sub run. This means that the cavity is situated exactly at 0.5 MHz, near the bump structure that we are going to discuss more in detail soon.
First of all it is important to apply all the calibrations to the power spectrum, in fact all the spectra calculated directly with the raw data contain all the amplifications. In addition to the gain of L5 that we have previously estimated, there is another source of gain/attenuation we have to deal with: the one of the downconversion electronics from the splitter input to the ADC board. This latter one has been performed only once and is valid for all sub runs, since it does not depend on the frequency change. We send a known power at the splitter and measure the downconverted signal at the DAQ input with a Spectrum Analyzer, which gives an absolute power. We repeat the measurement at different LO frequencies to cover all the acquisition bandwidth of the ADC board, from -1 to 1 MHz. In this way we obtain the calibration curve that describes all the downconversion sector and which must be subtracted to the raw power spectra.

The calibration curve is shown in Fig. 4.15, where the roll-off is due to the ADC internal filters and then this specific trend reappears necessarily in the measured spectrum of Fig. 4.14. In red the measured point described previously are presented, the ones obtained by changing the LO frequency, while in blue the interpolation of the experimental points that we will use to calibrate the measured power spectrum is shown. The amplification values measured reflect what we expected from the downconversion sector, being composed from coaxial cables, one mixer and two

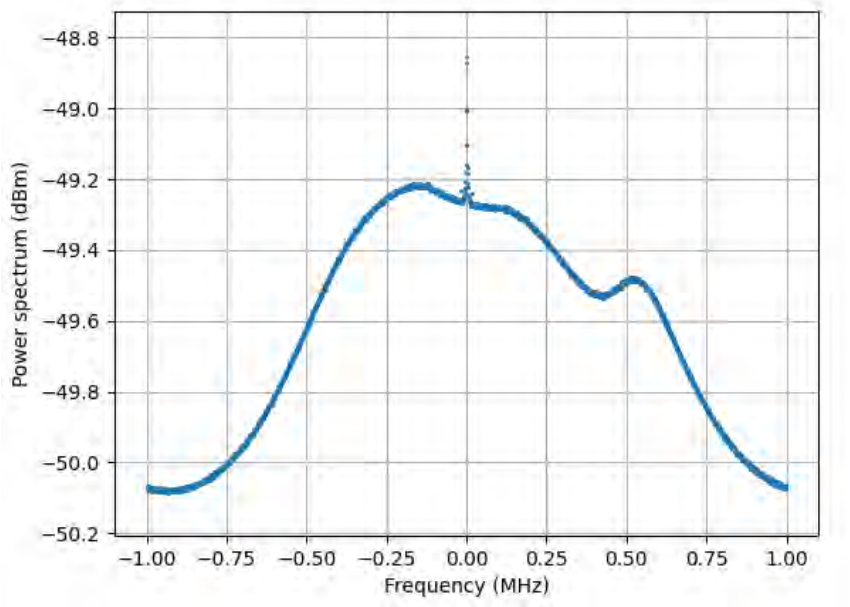

Figure 4.14. Averaged final power spectrum of the first experimental point corresponding to the $\nu_c = 8.831769$ GHz frequency.

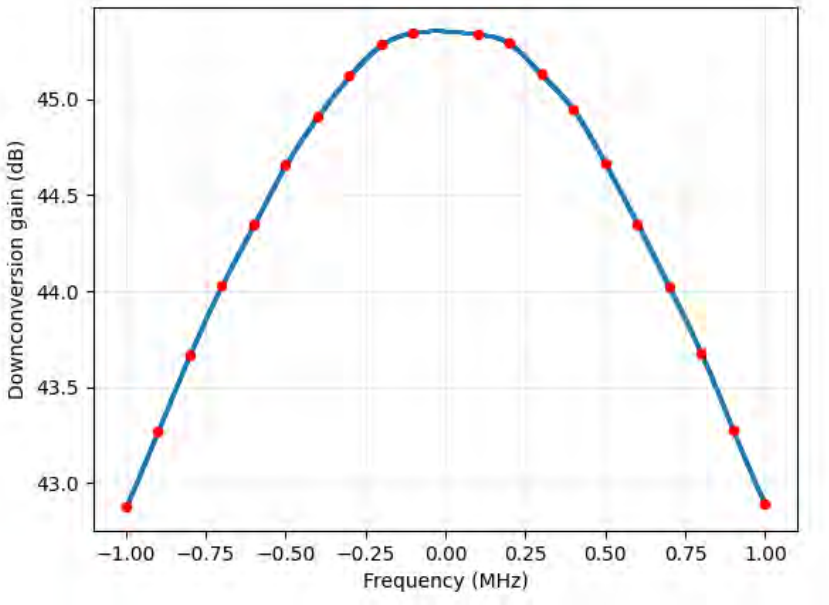

Figure 4.15. Calibration curve of the downconversion electronics from the splitter input to the ADC board. In red the experimental points are presented while in blue their interpolation is shown.

low-noise voltage amplifiers with a factor of $\times 10^3$.

It's now time to subtract from the raw power spectrum all the source of gains we estimated: the downconversion calibration curve and the gain G_{L5} are subtracted to the spectrum of Fig. 4.14 in order to obtain the calibrated power spectra, where now the power level is therefore referred at the cavity readout port.

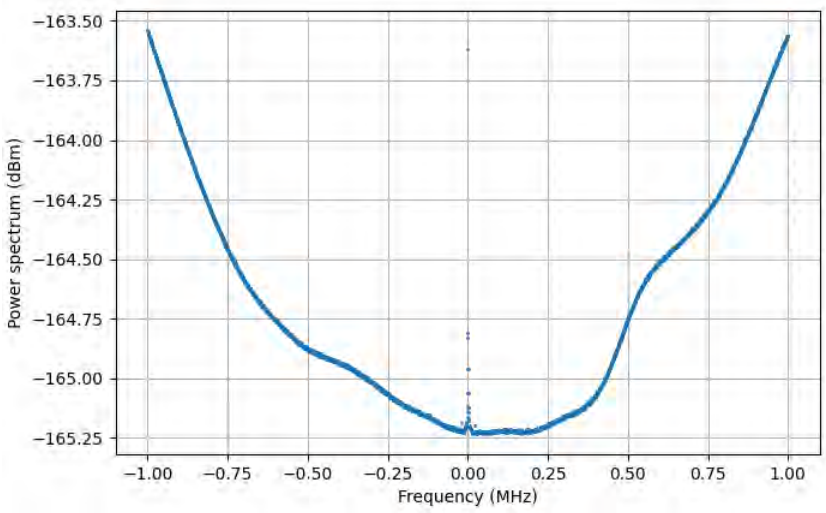

Figure 4.16. Final calibrated power spectrum with both the downconversion calibration curve and the gain G_{L5} subtracted.

In Fig. 4.16 is therefore shown the resulting calibrated power spectrum, with all his peculiar features we discussed earlier such as its slope and the bump structure at the right of the frequency of the resonant cavity that is situated at 0.5 MHz. The slope in the power spectrum is due to aliasing of the thermal noise at the edge of the Nyquist window, in fact since the sampling frequency of the ADC board used is 2 MS/s we are at the limit of application of the Nyquist theorem because our sampling frequency is exactly equal to the double of the maximum frequency (1 MHz) and is not greater.
The bump structure is instead due to the imperfect thermalization and isolation of the rf components connected to the resonant cavity, this can be stated by operating a more specific analysis that concerns all the power spectra of all the 24 sub runs. The procedure we discussed for the first frequency experimental point is therefore done for all the sub runs, leading to 24 final calibrated spectra that are shown in Fig. 4.17. In the figure all the power spectra properly converted from dBm to Watts and one extra spectrum are presented. This extra one is in black, and corresponds to an additional run of measurements with the moving antenna decoupled from the cavity. For this reason the decoupled run doesn't present the bump structure we are going to deal now.
The resonant cavity, being located at 0.5 MHz at each sub run, is situated for most of the power spectra at one flex point; it can be seen in fact that the majority of the sub runs present a bump at the right or left of the frequency of the resonant cavity. The key point here is that across the dataset it can be observed that the power spectra line shapes show features typical of Fano interference, as recently reported in [62] where similar interference phenomena in microwaves measurements were analyzed.

Fano interference is generally observed in wave scattering experiments and it

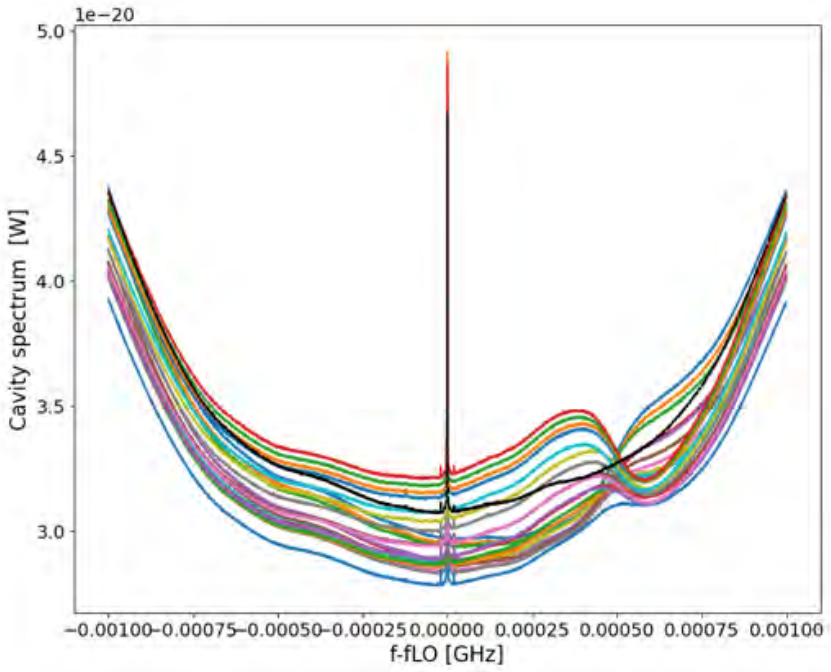

Figure 4.17. All the 24 final calibrated spectra corresponding to all the 24 sub runs. An extra spectrum is present, the black one, corresponding to the additional run with the moving antenna decoupled. Picture provided by Dr. Alessandro D'Elia.

occurs whenever a resonantly scattered signal interferes with background paths. Such paths are inherently present in microwave resonator measurement setups due to port-to-port leakage, impedance mismatches, or other device imperfections.
A visual representation of this model is given in Fig. 4.18 where origin and symptoms of Fano interference in microwave resonator measurements are shown.

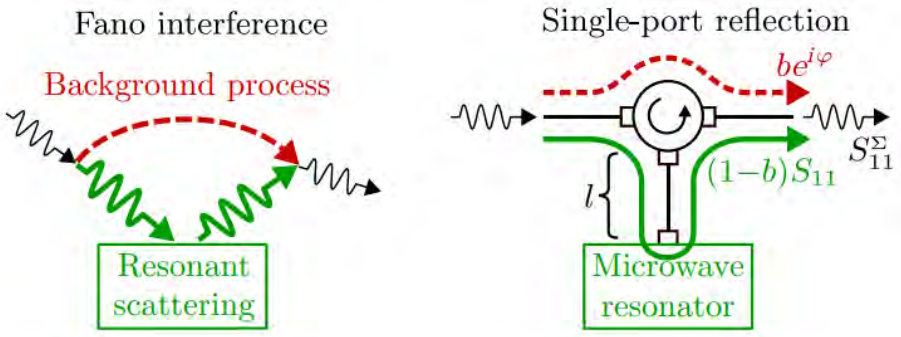

Figure 4.18. [62] Left: a Schematic depiction of Fano interference in wave scattering experiments. Right: Fano interference in single port reflection measurements.

In the left image is depicted a general scheme of a Fano interference in a wave scattering experiments, a background path interferes with the signal scattered by the measured resonant system. In the right image instead is shown a Fano interference in single-port reflection measurements where the finite circulator isolation constitutes a dominant background path.
A visual representation of the resulting effect of a Fano interference on the final

measured signal is instead given in Fig. 4.19.

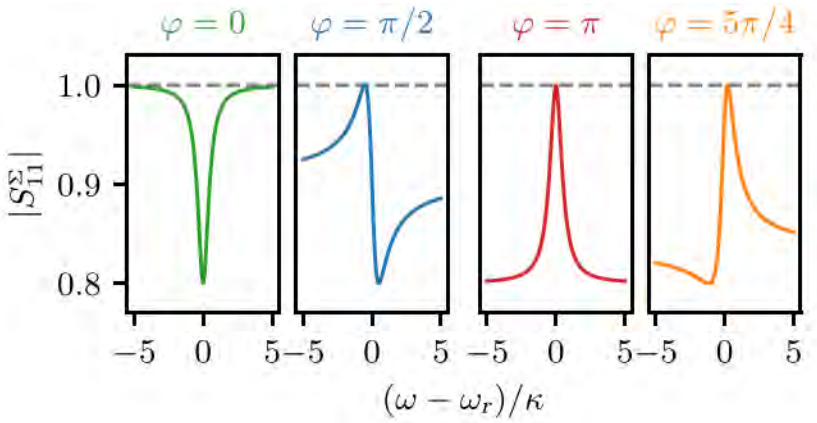

Figure 4.19. [62] Fano lineshapes: resonator responses can be asymmetric or even exhibit peaks depending on ϕ.

The resulting amplitude lineshapes then show dips, peaks, and different degrees of asymmetry depending on the relative background phase ϕ. These apparent loss and gain curves illustrate the systematic distortions of the resonator response due to Fano interference. In this sense therefore it can be explained the fact that starting from a situation in which the bump resides at the right of the cavity resonant frequency as in Fig. 4.16, the bump structure changes relative position with respect to ν_c moving forward and considering one by one all the sub runs spectra. The bump of the first experimental resonant frequency can be noted in blue in Fig. 4.17 together with all the other sub runs, going from an intermediate stage of a bump centered in ν_c up to a final mirrored configuration of a bump at the left of the resonant frequency; all following the scheme presented by the fano resonance in Fig. 4.19.
We then observe the appearance of bump like structures in the power spectra, which exhibit characteristic interference features. These are attributed to a combination of effects. Primarily, the bump originates from an excess of power relative to the thermal background, caused in this case by a thermal source inside the cavity operating at a temperature $T_{\text{cav}} > T_{\text{base}}$, (the "hot rod"). In the absence of additional effects at the output port, such a contribution would result in a symmetric profile (i.e., without Fano like distortions). However, it is likely that the circulator and/or the coaxial cable connecting the circulator to the cavity are not perfectly thermalized at 20 mK. Indeed, part of the noise originating from the 4 K stage propagates backward from the HEMT amplifier and from the attenuators, which themselves act as thermal sources. Furthermore, the cable is intentionally left unanchored to the mixing chamber plate in order to remain flexible as it is lowered by the piezoelectric motor. This mechanical freedom compromises thermal anchoring and, as a result, the cable, circulator, or associated connectors can act as additional sources of thermal noise. Such a thermal source would emit in any direction as it can be seen in Fig. 4.20. The outgoing wave V_+, propagating toward the output line L5, then interferes coherently with the reflected wave V_-, which is reflected by the cavity and redirected toward L5.
To describe the resulting spectral shape, which combines a frequency dependent term with a thermal background, we use an expression analogous to Eq. (1) in [62]:

$$P = k_B T_{\text{circ}} \Delta\nu \left| S_{11} e^{-i(\omega dt + \phi)} + 1 \right|^2 + k_B T_{\text{cav}} \Delta\nu |S_{21}|^2, \tag{4.19}$$

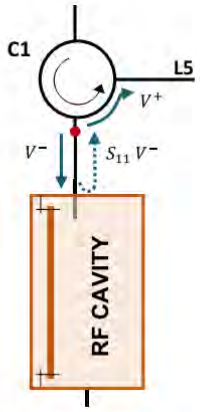

Figure 4.20. [9] Schematic illustration of the coherent sum between a frequency-dependent wave, $S_{11}V_-$, and a frequency-independent component, V_+, originating from the emission of a non thermalized point (highlighted in red).

where S_{11} and S_{21} are the usual scattering parameters, T_{circ} represents the effective temperature of the circulator system, dt is the electrical delay, ϕ is a phase shift, and $\Delta\nu$ is the spectral bin width (500 Hz in our case).

In Fig. 4.21, we compare three representative spectra, acquired at 8.8317690 GHz,

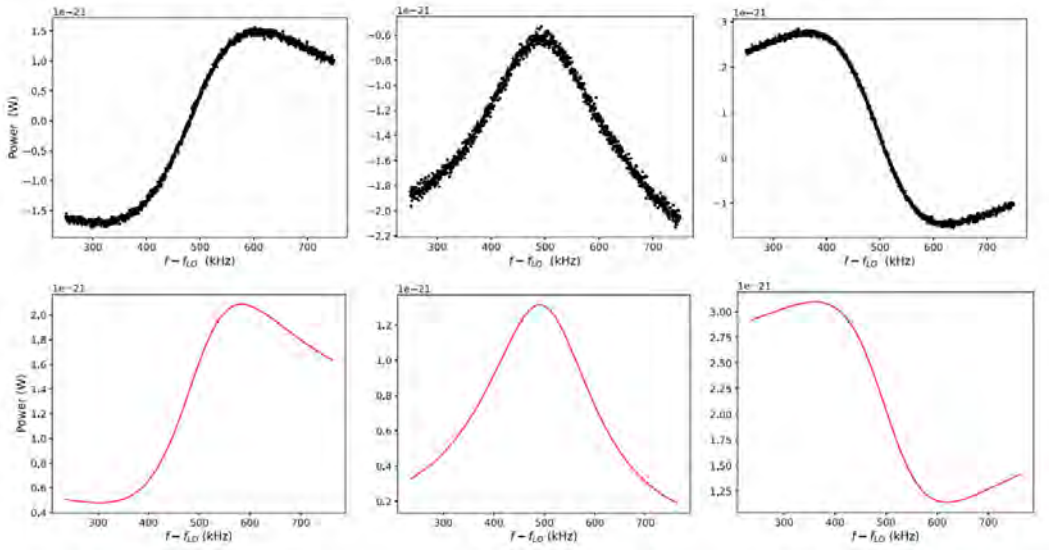

Figure 4.21. [9] Top: Experimental power spectra centered at 8.8317690, 8.8341279, and 8.8377664 GHz, after subtracting the spectrum acquired with the antenna decoupled from the cavity. Bottom: Simulated power spectra at the same frequencies, generated using Eq. (4.19).

8.8341279 GHz, and 8.8377664 GHz, with the corresponding theoretical curves (in red) generated using Eq. (4.19) and the following reasonable parameter values: $T_{\text{circ}} = 0.45\,\text{K}$, $T_{\text{cav}} = 0.1\,\text{K}$, $dt = 10\,\text{ns}$, and, respectively, $\phi = -0.8, -0.1, 0.9$. Although a rigorous fitting procedure is difficult to implement due to the strong correlation among parameters, the comparison nonetheless provides a reasonable estimate of the effective temperatures and system response.

For the subsequent data analysis, for each frequency step, we estimate T_{sys} from the output power of Fig. 4.17 at a reference frequency $\nu_{LO} + 100$ kHz, where 1/f noise is negligible and still far enough from the cavity resonance, obtaining an average value of 4.7 K. As just discussed, we observe that the power spectra line shapes show features typical of Fano interference in addition to what we expected for our system. Thanks to the model described in [62] we interpreted the bump structure as due to a imperfect isolation and thermalization of the circulator, attenuators and the rod inside the cavity, leading to effective temperatures greater than expected from thermalization; in particular, we estimate an average temperature over all the frequency steps of about $T_{cav} \approx 100$ mK and $T_{circ} \approx 450$ mK.
What is important though, is that this effect does not affect the extraction of the power generated by axion conversion we will talk about in Section 4.3, since it adds incoherently.
Before moving on to the last section it's instructive to talk a moment about one parameter we used in the fits of Section 4.1.2, which has to do with fano interference. The parameter q, present in Tab. 4.1 and in the fit equation of the S_{22}^{cav} equation, is in fact a parameter that takes into account the small asymmetries in the reflective coefficient. We can therefore interpret this asymmetries due to the fano interference we discussed in this section, this interference is indeed visible though all the sub runs in different manifestations: with respect to the relative background phase ϕ of the fano resonance we have a different distortion on the measured reflective coefficients S_{22}.
Below in Fig. 4.22 are then shown two examples of the different effect of the fano interference on the S_{22} coefficient through all the sub runs. In particular the left image is about the second frequency step of the experiment ($\nu_c = 8.83203080$ GHz) while the right image is about the last sub run ($\nu_c = 8.83776640$ GHz). The measured S_{22} coefficient then shows the same trend of the power spectra we discussed previously in this section, having the distortion first at the right of the resonance and then at the left, this can be seen in fact from the fits done that in this two particular cases have some errors in describing well the measured coefficients far away from the resonant frequency point. This effect can be considered then due to the fano interference that through all the frequency steps distorts the theoretical S_{22}^{cav} shape, that in this case we described by just adding the q variable in the fits.

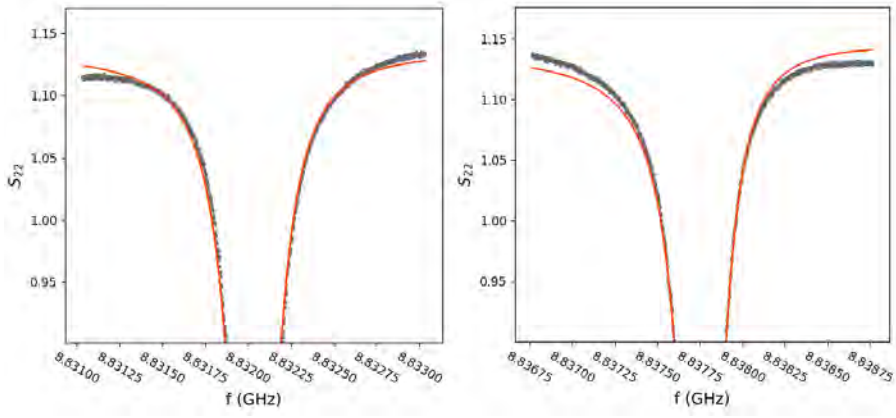

Figure 4.22. Different effect of the fano interference on the S_{22} coefficient. At left the second frequency step of the experiment while on right the last sub run. This distortion through the sub runs follow the distortion on the power spectra.

4.3 Data analysis

After describing all the calibration procedures along with the data taking and processing, we've reached the point where we have the calibrated power spectra for all the frequency points, each corresponding to a different axion mass value. This last section is then dedicated to the final data analysis that consists in the extraction of the power generated by a possible axion conversion. In the end we'll end up with a potential axion signal or, much more likely, with an exclusion limits for $g_{a\gamma\gamma}$ in the mass range we took into account. In the subsequent discussion I will follow the analysis presented in [9] because I haven't put directly my hands on this part of the experiment.
As discussed in Section 3.2.2, in presence of axion conversions a power surplus is expected in the cavity power spectrum as given by Eq. (3.62). The first step is to take all the 24 power spectra showed in Fig. 4.17 and to calculate the residuals by subtracting each spectrum to a polynomial obtained with a Savitzky-Golay (SG) filter [63] from the spectrum itself. A Savitzky–Golay filter is a digital filter that can be applied to a set of digital data points for the purpose of smoothing the data, that is, to increase the precision of the data without distorting the signal tendency. This is achieved by fitting successive sub sets of adjacent data points with a low degree polynomial by the method of linear least squares.
In our specific case we adopt a SG filter of the fourth order with a dynamic interval of 250.5 kHz (501 bins). For each sub run, the filter is applied in a window $[\nu_c - \Gamma, \nu_c + \Gamma]$ of about 530 kHz, where Γ is the cavity line width and is calculated as ν_c/Q_L.
An example of polynomial obtained from a SG filter from one of the datasets is shown in Fig. 4.23. The image is about a section around the resonance of the ninth sub run that corresponds to $\nu_c = 8.833862$ GHz and it shows the data points measured and calibrated together with the digital filter applied, it can be seen how the SG filter smooths the data without distorting its trend. We in fact discussed in the previous section the two main characteristic of the data tendency: the slope in the power spectrum is due to aliasing of the thermal noise at the edge of the Nyquist window, while the bump structure is due to the imperfect thermalization and isolation of the rf components connected to the resonant cavity.

Calculated the residuals for each of the frequency steps, the next operation is to normalize the residuals to the expected noise power σ_{Dicke} for each dataset, where σ_{Dicke} is calculated using the Dicke radiometer equation [51]:

$$\sigma_{Dicke} = k_B T_{sys} \sqrt{\Delta\nu \Delta t}, \tag{4.20}$$

in which k_B is the boltzmann constant, T_{sys} is the system noise temperature we estimated in the previous section, $\Delta\nu$ is the bin width (500 Hz) and Δt is the integration time (3764 s).
The cumulative distribution of the normalized residuals obtained combining all the sub runs, is then shown in Fig. 4.24. The data follow a Gaussian distribution, with a mean value as expected equal to zero with good approximation and a standard deviation compatible with 1.

The last step for the extraction of a possible axion signal is the following: for each of the experimental resonant frequency measured of Tab. 4.2 there corresponds a different value of axion mass m_a in the range $36.5241 - 36.5510$ μeV. For each axion mass then, we apply the Least Squares method to estimate the best value $\hat{g}_{a\gamma\gamma}$ by minimizing

$$\chi^2 = \sum_{\alpha=1}^{N_{scan}} \sum_{i=1}^{N_{bin}} \left[\frac{R_{\alpha,i} - S_{\alpha,i}(m_a, g^2_{a\gamma\gamma})}{\sigma^{(\alpha)}_{Dicke}} \right]^2, \tag{4.21}$$

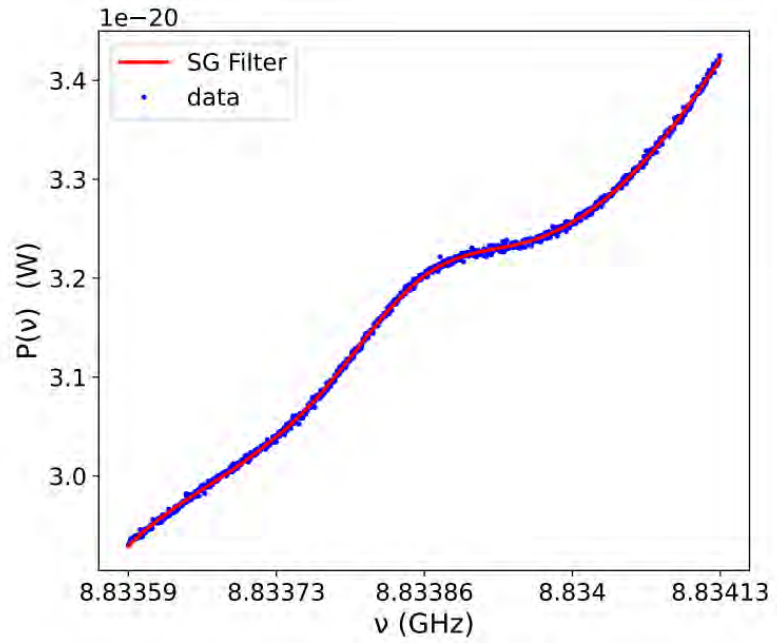

Figure 4.23. [9] Zoom around the resonance of the FFT cavity power spectrum corresponding to $\nu_c = 8.833862$. The measured data are in blue while the SG filter is shown in red.

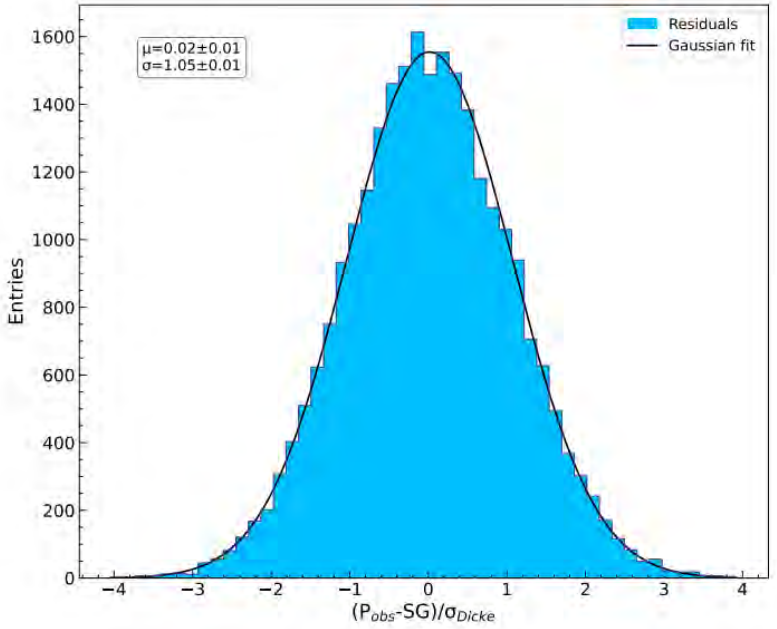

Figure 4.24. [9] Distribution of the cumulative normalized residuals, together with its gaussian fit.

where the α index runs over the number of datasets (N_{scan}) and the index i runs over the frequency bins of each power spectrum. $S_{\alpha,i}$ and $R_{\alpha,i}$ are instead the expected power signal and the residuals for frequency bin i and the dataset α. We have just calculated $R_{\alpha,i}$ for each of the power spectra while $S_{\alpha,i}$ are calculated as the

integral in the frequency domain of Eq. (3.62) multiplied by the spectrum of the full standard halo model distribution [39].
Factorizing now $S_{\alpha,i}$ as $S_{\alpha,i}(m_a, g^2_{a\gamma\gamma}) = g^2_{a\gamma\gamma} T_{\alpha,i}(m_a)$, we can analytically minimize Eq. (4.21) by solving

$$\frac{\partial \chi^2}{\partial g^2_{a\gamma\gamma}} = 0 \tag{4.22}$$

and we can calculate its uncertainty according to the formula:

$$\frac{1}{\sigma^2_{\hat{\xi}}} = \frac{1}{2}\frac{\partial^2 \chi^2}{\partial^2 \xi}, \tag{4.23}$$

where $\xi = g^2_{a\gamma\gamma}$ for graphic purposes. Writing now $\sum\sum \equiv \sum_{\alpha=1}^{N_{scan}} \sum_{i=1}^{N_{bin}}$ for graphic reasons too, we can finally minimize Eq. (4.21) in order to find $\overline{g^2}$ which is the average squared coupling constant that incorporates the contributions of all the frequency bins from all the datasets and is equal to:

$$\overline{g^2} = \sigma^2(\overline{g^2}) \left[\sum\sum \frac{R_{\alpha,i} T_{\alpha,i}(m_a)}{(\sigma^{(\alpha)}_{Dicke})^2} \right], \tag{4.24}$$

where $\sigma^2(\overline{g^2})$ is its variance calculated as:

$$\sigma^2(\overline{g^2}) = \sum\sum \left[\frac{T_{\alpha,i}(m_a)}{\sigma^{(\alpha)}_{Dicke}} \right]^2. \tag{4.25}$$

This procedure is therefore repeated for different values of m_a in our range of interest ($36.5241 - 36.5510$ μeV), knowing that the detection of a power excess larger than 5σ above the noise is required for a candidate discovery. In Fig. 4.24 can be seen that no candidates fulfill this requirement since all the residues lies within the 4σ range of the gaussian distribution. Since no candidates, which could be thought of axion like signal, are found, the exclusion limits for $g_{a\gamma\gamma}$ in this mass range is determined with the following procedure.
To correctly estimate the limits regarding this experimental run to add to the axion parameter space shown in Fig. 2.3, we need to account for the efficiency of the filtering procedure used for the extraction of the axion signal. Following the procedure discussed in [64], a Monte Carlo simulation is run numerically injecting a fake axion signal with a known $g^2_{injected}$ into simulated power-spectra with different ν_c. At this point Eq. (4.24) is used to estimate the $g^2_{injected}$ for each injected signal, obtaining then $g^2_{calculated}$. The efficiency is therefore determined from the relation between $g^2_{calculated}$ and $g^2_{injected}$. The cavity power spectra is instead simulated by adding random Gaussian noise, with $\mu = 0$ and $\sigma = \sigma_{Dicke}$ following a Gaussian PDF, to the Savitzky–Golay filters previously obtained. Applying this procedure, a detection efficiency of 0.845 is then estimated on $g^2_{calculated}$ for the SG filter.
Hence, after correcting for the estimated efficiency, the single sided upper limit on the axion photon coupling is calculated with a 90% confidence level as in [65]. Using a power constrained procedure for the $\overline{g^2}$ that under fluctuates below $-\sigma$ [66], the upper limit $g^{CL}_{a\gamma\gamma}$ is finally obtained in the axion mass window of 27.02 neV centered around 36.53764 μeV as shown in Fig. 4.25. This graph then shows the 90% single sided C.L. upper limit for $g_{a\gamma\gamma}$ as a function of the axion mass in our range of interest. The violet solid curve represents the expected limit in the case of no signal while

the yellow region indicates the QCD axion model band we discussed in Section 2.2.2. The maximum sensitivity obtained with a 90% CL is $g_{a\gamma\gamma}^{CL} < 0.882 \times 10^{-13}$ GeV^{-1}, value that is about 6 times larger with respect to the benchmark QCD axion level of the KSVZ theory [24, 25]. With this run we therefore almost approach the QCD axion model band, being this the final target of an experiment of this type that will allow us to definitely probe a certain region of the axion mass described by a specific theoretical model.
To conclude this work it is also instructive to show how this experimental run stands out from all the others experimental limits displayed in Fig. 2.3. Fig. 4.26, realized through [28], is then a broad view of axion exclusion limits set by haloscopes. The blue vertical line indicates the search presented in this thesis and, as it can be seen, is the only one active experiment present in the axion mass range we treated.

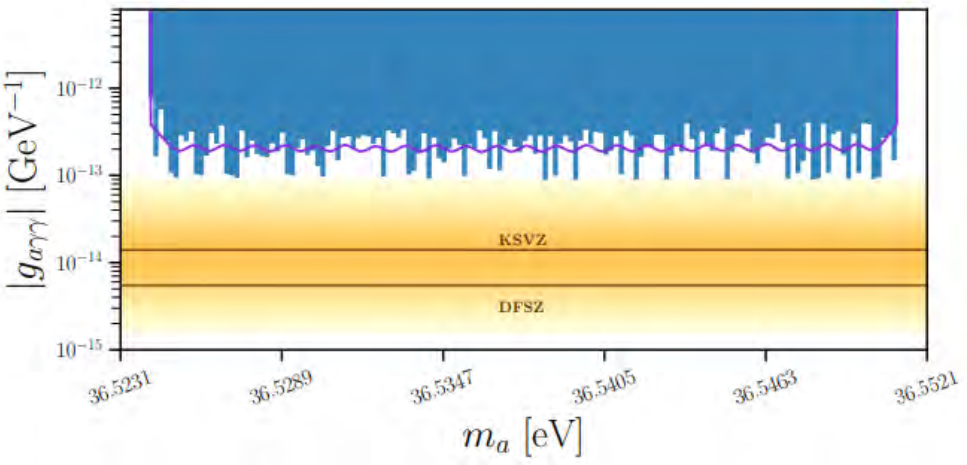

Figure 4.25. [9] 90% single sided C.L. upper limit for $g_{a\gamma\gamma}$ as a function of the axion mass. In violet the expected limit in case of no signal while in yellow is shown the QCD axion model band.

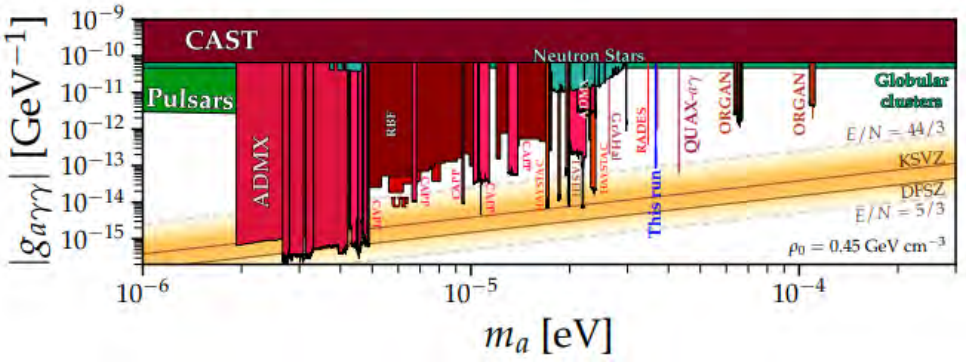

Figure 4.26. [9] Broad view of axion exclusion limits set by haloscopes. In blue the search discussed in this thesis.

Chapter 5

Conclusions

The work presented in this thesis lies within the context of dark matter research, focusing on axions as a compelling solution to both a theoretical and cosmological problem. In particular, this study centered on the QUAX–LNF experiment, a tunable haloscope currently under development at the Laboratori Nazionali di Frascati, aiming to detect dark matter axions through their coupling to photons.
Starting from theoretical motivations, namely the Peccei Quinn mechanism as a dynamical solution to the strong CP problem, axions emerge not only as a theoretically elegant solution, but also as a plausible constituent of cold dark matter. As discussed in Chapter 2, the presence of a CP violating θ term in the QCD Lagrangian as in Eq. (2.23), though experimentally constrained to be extremely small, lacks a natural explanation within the Standard Model. The Peccei Quinn solution promotes this parameter to a dynamical field, giving rise to a pseudo Goldstone boson: the axion. Its mass and coupling constants are inversely proportional to the symmetry breaking scale f_a like in Eq. (2.37) and in Eq. (2.38). Astrophysical and cosmological constraints have helped narrow the viable parameter space for QCD axions, motivating the experimental effort to probe the μeV–meV mass range.
In Chapter 3, I outlined the fundamental radiofrequency principles that underpin haloscope experiments, focusing in particular on resonant cavities. Key theoretical tools such as cavity parametrization (Section 3.1.2) and scattering matrices (Section 3.1.3) were introduced to motivate the experimental design of QUAX. The detection sensitivity depends critically on the cavity quality factor Q, the geometry (via the form factor C), the magnetic field, and the thermal noise environment.
Chapter 4 described my personal contribution to the experiment. I had the opportunity to work directly on the experimental setup and take part in the first run of the QUAX LNF haloscope. I contributed to the calibration of the RF lines, helped implement and validate the fit procedure of the scattering parameters for extracting the gain contribution of the distinct lines inside the cryostat (Section 4.1.2). I also assisted in the data acquisition process (Section 4.2), where the system scanned over a 6 MHz frequency interval, integrating the power spectrum in search of narrow peaks consistent with axion to photon conversion.
Although no signal attributable to axion dark matter was detected, we derived an upper limit on the emitted power, which was then translated into a constraint on the axion photon coupling, leading to an exclusion plot in the $g_{a\gamma\gamma}$-m_a plane as in Fig. 4.25. This experimental setup allowed us to exclude the existence of axion dark matter in a mass range between 36.52413 and 36.5511 μeV with axion photon coupling down to 0.882 $\times 10^{-13}$ GeV^{-1} with a C.L. of 90%. This result also contributes to the global effort to probe the axion parameter space and complements the regions explored by other haloscope experiments such as ADMX or HAYSTAC

as it can be seen in Fig. 4.26.
As a last thing is illuminating to talk about the future step of the QUAX experiment, the apparatus has in fact still much room for improvement. In the next future, the sensitivity can be boosted employing a superconducting resonant cavity, enhancing the intrinsic quality factor. Adding a Josephson Parametric Amplifier as a preamplification stage will break the noise temperature down by one order of magnitude. Moreover, the rod design can be optimized:

- the amount of dielectric exposed to the electromagnetic mode of the cavity can be reduced;
- the lower end of the bar can be placed directly in contact with the endcap of the cavity eliminating PEEK on this side;
- the PEEK can be eventually substituted with sapphire.

To quantify, running such a setup for 1 hour with a quality factor $Q_0 = 3 \times 10^5$ at a frequency of 9 GHz and coupling $k = 2$, would reach an average value for the coupling of $\approx 2 \times 10^{-14}$ GeV^{-1}, provided that the noise temperature is 0.5 K and the magnet is brought to 9 T. This value is a factor less than 1.5 from the benchmark KSVZ model.
Other future improvements may be the change of the acquisition ADC board, the one used had in fact a 2 MHz bandwidth with a sampling frequency of 2 MS/s and as discussed in Section 4.2 this situation led us to the limit of application of the Nyquist theorem.
Logistical enhancements are also possible, we said that for each dataset of the 24 reported in Tab. 4.2 we calculated the power spectrum simultaneously with the data acquisition. Actually, this procedure has been done through a subsequent data manipulation with a Python script right before the analysis of the spectra and after the acquisition through the ADC board. This sequential procedure introduced significant waiting times, waiting for the script to calculate the averaged spectra for each experimental point. This issue can be addressed through two main improvements. First, the entire workflow can be automated so that raw data from the ADC board are immediately pre processed and made available as power spectra. Second, and more immediately realizable, the data processing script can be rewritten in C++, a language recognized for its superior performance in this context. This task was my final contribution during the internship: I rewrote the Python script in C++ and verified its improved performance. When tested on the first sub-run of the experiment, the C++ version proved to be about five times faster.
All these improvements, if implemented, would enhance the QUAX experiment from multiple perspectives, increasing its potential in the experimental search for axions.

Bibliography

[1] Irastorza, I. G. & Redondo, J. New experimental approaches in the search for axion-like particles. Progress in Particle and Nuclear Physics 102, 89–159 (2018).

[2] Peccei, R. D. & Quinn, H. R. CP Conservation in the Presence of Pseudoparticles. Phys. Rev. Lett. 38, 1440–1443 (1977).

[3] Peccei, R. D. & Quinn, H. R. Constraints imposed by CP conservation in the presence of pseudoparticles. Phys. Rev. D 16, 1791–1797 (1977).

[4] Pendlebury, J. M. et al. A Revised Experimental Upper Limit on the Electric Dipole Moment of the Neutron. Phys. Rev. D 92, 092003 (2015).

[5] Weinberg, S. A New Light Boson? Phys. Rev. Lett. 40, 223–226 (1978).

[6] Wilczek, F. Problem of Strong P and T Invariance in the Presence of Instantons. Phys. Rev. Lett. 40, 279–282 (1978).

[7] Sikivie, P. Experimental Tests of the 'Invisible' Axion. Phys. Rev. Lett. 51, 1415–1417 (1983).

[8] Primakoff, H. Photo-Production of Neutral Mesons in Nuclear Electric Fields and the Mean Life of the Neutral Meson. Phys. Rev. 81, 899–899 (1951).

[9] Rettaroli, A. et al. Search for axion dark matter with the QUAX–LNF tunable haloscope. Phys. Rev. D 110, 022008 (2024).

[10] Brubaker, B. M. First results from the HAYSTAC axion search. arXiv:1801.00835 [astro-ph, physics:hep-ex, physics:hep-ph, physics:physics] (2018).

[11] Rettaroli, A. Characterization of superconducting resonant RF cavities for axion search with the QUAX experiment. (INFN, Rome3, 2018).

[12] F. Mandl and G. Shaw. Quantum Field Theory. Wiley, 2010

[13] P. Collins, A. Martin, and E. Squires. Particle Physics and Cosmology. Wiley, 1989

[14] M. Srednicki. Quantum Field Theory. Cambridge University Press, 2007

[15] Weinberg, S. The U(1) problem. Phys. Rev. D 11, 3583–3593 (1975).

[16] Peccei, R. D. QCD, Strong CP and Axions. Preprint at http://arxiv.org/abs/hep-ph/9606475 (1996).

[17] Peccei, R. D. The Strong CP Problem and Axions. in vol. 741 3–17 (2008).

[18] Adler, S. L. Axial-Vector Vertex in Spinor Electrodynamics. Phys. Rev. 177, 2426–2438 (1969).

[19] A.A. Belavin, A.M. Polyakov, A.S. Schwartz, Yu.S. Tyupkin, Pseudoparticle solutions of the Yang-Mills equations, Phys. Lett. B 59, 85 (1975).

[20] 'T Hooft, G. Symmetry Breaking through Bell-Jackiw Anomalies. Phys. Rev. Lett. 37, 8–11 (1976).

[21] M. D. Schwartz, Quantum Field Theory and the Standard Model (Cambridge University Press, 2014).

[22] Pospelov, M. & Ritz, A. Theta Vacua, QCD Sum Rules, and the Neutron Electric Dipole Moment. Nuclear Physics B 573, 177–200 (2000).

[23] Bardeen, W. A., Peccei, R. D. & Yanagida, T. CONSTRAINTS ON VARIANT AXION MODELS. Nucl. Phys. B 279, 401–428 (1987).

[24] Kim, J. E. Weak-Interaction Singlet and Strong CP Invariance. Phys. Rev. Lett. 43, 103–107 (1979).

[25] Shifman, M. A., Vainshtein, A. I. & Zakharov, V. I. Can confinement ensure natural CP invariance of strong interactions? Nuclear Physics B 166, 493–506 (1980).

[26] Zhitnitskii, A. P. Possible suppression of axion-hadron interactions. Sov. J. Nucl. Phys. (Engl. Transl.); (United States) 31:2, (1980).

[27] Dine, M., Fischler, W. & Srednicki, M. A simple solution to the strong CP problem with a harmless axion. Physics Letters B 104, 199–202 (1981).

[28] C. O'Hare, cajohare/axionlimits: Axionlimits, https:// cajohare.github.io/AxionLimits/ (2020).

[29] Particle Data Group et al. Review of Particle Physics. Progress of Theoretical and Experimental Physics 2022, 083C01 (2022).

[30] Raffelt, G. G. Astrophysical Axion Bounds. in vol. 741 51–71 (2008).

[31] Srednicki, M. Axion couplings to matter: (I). CP-conserving parts. Nuclear Physics B 260, 689–700 (1985).

[32] Jaeckel, J. & Ringwald, A. The Low-Energy Frontier of Particle Physics. Annu. Rev. Nucl. Part. Sci. 60, 405–437 (2010).

[33] Planck Collaboration et al. Planck 2018 results: VI. Cosmological parameters. A&A 641, A6 (2020).

[34] Hertzberg, M. P., Tegmark, M. & Wilczek, F. Axion Cosmology and the Energy Scale of Inflation. Phys. Rev. D 78, 083507 (2008).

[35] Any Light Particle Search. https://alps.desy.de/.

[36] Sikivie, P. Detection rates for '"invisible"'-axion searches. Phys. Rev. D 32, 2988–2991 (1985).

[37] Read, J. I. The Local Dark Matter Density. J. Phys. G: Nucl. Part. Phys. 41, 063101 (2014).

[38] Lentz, E. W., Quinn, T. R., Rosenberg, L. J. & Tremmel, M. J. A New Signal Model for Axion Cavity Searches from N-Body Simulations. ApJ 845, 121 (2017).

[39] Turner, M. S. Periodic signatures for the detection of cosmic axions. Phys. Rev. D 42, 3572–3575 (1990).

[40] Asztalos, S. et al. Large-scale microwave cavity search for dark-matter axions. Phys. Rev. D 64, 092003 (2001).

[41] Gatti, C. From KLASH to FLASH A Proposal for a 100-300 MHz Haloscope.

[42] Alesini, D. et al. The future search for low-frequency axions and new physics with the FLASH resonant cavity experiment at Frascati National Laboratories. Physics of the Dark Universe 42, 101370 (2023).

[43] D. M. Pozar. Microwave Engineering. Wiley, 2012

[44] Kenany, S. A. et al. Design and Operational Experience of a Microwave Cavity Axion Detector for the 20-100 micro-eV Range. Nuclear Instruments and Methods in Physics Research Section A: Accelerators, Spectrometers, Detectors and Associated Equipment 854, 11–24 (2017).

[45] Krauss, L., Moody, J., Wilczek, F. & Morris, D. E. Calculations for cosmic axion detection. Phys. Rev. Lett. 55, 1797–1800 (1985).

[46] Barbieri, R. et al. Searching for galactic axions through magnetized media: The QUAX proposal. Physics of the Dark Universe 15, 135–141 (2017).

[47] Crescini, N. et al. Operation of a ferromagnetic axion haloscope at $m_a = 58\,\mu$eV. Eur. Phys. J. C 78, 703 (2018).

[48] Alesini, D. et al. Search for invisible axion dark matter of mass $m_a = 43\,\mu$eV with the QUAX– a γ experiment. Phys. Rev. D 103, 102004 (2021).

[49] Kim, D., Jeong, J., Youn, S., Kim, Y. & Semertzidis, Y. K. Revisiting the detection rate for axion haloscopes. J. Cosmol. Astropart. Phys. 2020, 066–066 (2020).

[50] Nyquist, H. Thermal Agitation of Electric Charge in Conductors. Phys. Rev. 32, 110–113 (1928).

[51] Dicke, R. H. The Measurement of Thermal Radiation at Microwave Frequencies. Rev. Sci. Instrum. 17, 268–275 (1946).

[52] Zmuidzinas, J. Thermal noise and correlations in photon detection. Appl. Opt. 42, 4989 (2003).

[53] COLD Lab – The Cryogenic Laboratory of LNF. https://coldlab.lnf.infn.it/.

[54] attocube systems is the partner of choice for research laboratories and OEM customers all over the world. attocube https://www.attocube.com/en/products/nanopositioners/low-temperature-nanopositioners/anpz101lt-linear-z-nanopositioner.

[55] attocube systems is the partner of choice for research laboratories and OEM customers all over the world. attocube https://www.attocube.com/en/products/nanopositioners/low-temperature-nanopositioners/anr240lt-rotator-360-endless.

[56] Ansys HFSS | 3D High Frequency Simulation Software. https://www.ansys.com/products/electronics/ansys-hfss.

[57] Ventura, G. & Risegari, L. The Art of Cryogenics: Low-Temperature Experimental Techniques. (Elsevier, Amsterdam; Boston, 2008).

[58] Rettaroli, A. Study of devices based on Josephson junctions for galactic axion search. (INFN, Rome3, 2021).

[59] LNF-LNC6_20SC. Low Noise Factory https://lownoisefactory.com/product/lnf-lnc6_20sc/.

[60] Model: LNA-30-08001200-09-10P - Amplifier. Narda-MITEQ https://nardamiteq.com/viewmodel.php?model=LNA-30-08001200-09-10P.

[61] Braggio, C. et al. A haloscope amplification chain based on a traveling wave parametric amplifier. Review of Scientific Instruments 93, 094701 (2022).

[62] Rieger, D. et al. Fano Interference in Microwave Resonator Measurements. Phys. Rev. Applied 20, 014059 (2023).

[63] Savitzky, Abraham. & Golay, M. J. E. Smoothing and Differentiation of Data by Simplified Least Squares Procedures. Anal. Chem. 36, 1627–1639 (1964).

[64] Alesini, D. et al. Search for Galactic axions with a high-Q dielectric cavity. Phys. Rev. D 106, 052007 (2022).

[65] Alesini, D. et al. Galactic axions search with a superconducting resonant cavity. Phys. Rev. D 99, 101101 (2019).

[66] Cowan, G., Cranmer, K., Gross, E. & Vitells, O. Power-Constrained Limits. Preprint at https://doi.org/10.48550/arXiv.1105.3166 (2011).